ABSTRACT

Title of Thesis:	TRAVELING WAVE THERMOACOUSTIC-PIEZOELECTRIC ENERGY HARVESTER: THEORY AND EXPERIMENT
	Andrew Roshwalb, Master of Science, 2011
Master's Thesis directed by:	Professor Amr Baz Department of Mechanical Engineering

This thesis presents a theoretical and experimental investigation of a piezoelectric energy harvester coupled to a traveling wave thermoacoustic engine (TWTAE). By simplifying the engine using a lumped-parameter model, the performance parameters such as pressure oscillation frequency and amplitude, regenerator hot end temperature, and piezoelectric output voltage are predicted. Also, an axisymmetric finite element model of the piezoelectric energy harvester is developed, resulting in a two-part reduced-order model of the electromechanical impedance of the harvester. The predictions of the finite element model are compared with those of ANSYS finite element analysis and validated experimentally. The two-part model is utilized in a numerical analysis of the TWTAE using DeltaEC (Design Environment for Low-Amplitude ThermoAcoustic Energy Conversion). Results from pressure transducers and the piezoelectric disc attached to a physical realization of the TWTAE are compared with theoretical predictions of the lumped-parameter models and DeltaEC analysis. The developed theoretical techniques and experimental validation provide invaluable tools for effective design of the thermoacoustic-piezoelectric harvester.

TRAVELING WAVE THERMOACOUSTIC-PIEZOELECTRIC ENERGY HARVESTER: THEORY AND EXPERIMENT

by

Andrew Zvi Roshwalb

Thesis submitted to the Faculty of the Graduate School of the
University of Maryland, College Park in partial fulfillment
of the requirements for the degree of
Master of Science
2011

Advisory Committee:
Professor Amr Baz (chair)
Professor Balakumar Balachandran
Professor Nikhil Chopra

Acknowledgments

Firstly, I must thank Dr. Baz for guiding me through the process and giving life lessons along the way. For example, he always recommended I get a good night's sleep. I want to thank Dr. Gu for constructing the traveling wave thermoacoustic engine on which this thesis is based. I want to thank Dr. Wael Akl for helping me with the ANSYS coding. I want to thank Dr. Swift from Los Alamos for responding to my emails regarding DeltaEC. I want to thank the students for whom I was a TA for being cooperative and pleasant to work with.

I want to thank my friends Nick, Roman, Adam, Kurt, Daniel, Carolyn, Jenny, Abi, Andrew and Jenna for taking an interest in my progress. Mostafa, for helping me with classes and experimentation, and for encouraging me throughout my graduate career. Jason, for explaining the lab equipment. Mohamed, for making the labs an enjoyable place to work. My roommate Jeremy, for making sure I was alright during a late night. I must thank my parents for telling me I'm doing a good job without evidence to support this claim. I must also thank my fiancé Jackelyn for always being there. Always. It is impossible to remember all, and I apologize to those I've inadvertently left out.

Table of Contents

List of Tables

List of Figures

List of Symbols, Subscripts and Abbreviations

Symbols

a	area and mass of lumped-parameter components
A	area
$[A]$	matrix convention
$[B]$	matrix convention
c	speed of sound or radial piezo elastic modulus tensor coefficient
c^E	elastic modulus
C	flow conductance or analogous capacitance
$[C]$	matrix convention; matrix of modulus coefficients
C_H	refers to thermal capacity
d_{31}	piezo strain constant
D	electric displacement
$[D]$	matrix convention
E	elastic modulus or electric field
$\dot{E}$	acoustic power
$[E]$	matrix convention pertaining to electric field
$\{E_{total}\}$	convention; reformatted vector relating the global deflection vector to electric displacement
F	force
$[F(i\omega)]$	matrix convention; matrix coupling w_1 and V with p_t and I
g	volumetric flow gain
$\overset{*}{H}$	enthalpy flow rate
I	volumetric flow or current flow
k_{31}	electromagnetic coupling factor
$[K]$	stiffness matrix
KE	kinetic energy
l	length
L	inertance or length
m	mass
$\dot{m}$	mass flow rate
M	molar mass of gas or mass of gas "piston" or inertance due to mass or moment
$[M]$	mass matrix
N	number of nodes in FEM corresponding to $N-1$ elements
$[N_s]$	matrix convention in terms of radial coordinate s
p	pressure
P	pressure (in Laplace domain) or power supplied to regenerator
PE	potential energy
Q	charge
$\dot{Q}$	heat transfer rate

Symbols Continued

$\{Q\}$	vector of forces
r	radius
R	universal gas constant or flow or electrical resistance
$[R]$	matrix convention for Guyan reduction process
s	Laplace complex variable or local radial coordinate
S	strain
t	time or thickness
T	temperature or stress
u	displacement in radial direction
U	volumetric velocity
v	velocity
V	volume or voltage
$\overset{*}{V}$	volume flow rate
w	convention; inverse of the capacitance in electric analogue or displacement normal to plane
z	specific flow resistance
Z	convention or equivalent impedance of piezo
$[Z_p]$	2×2 matrix coupling mechanical and electrical impedance of combined aluminum-piezo disk
$\{Z_{total}\}$	convention; reformatted vector relating the global deflection vector to volume flow rate
$[ZE]$	matrix convention
α	thermal diffusivity of gas or shape function coefficients
γ	specific heat ratio
δp_t	$p_t - p_0$; difference between pulse pressure and equilibrium
$\{\delta\}$	deflection vector
ε	permittivity or strain
η	thermal efficiency or viscocity
κ	thermal conductivity
ν	Poisson's ratio
ρ	density
σ	stress
τ	time required for thermal equilibrium or temperature ratio ${}^{T_H}/_{T_C}$
ϕ	turning ratio
Φ	phase difference between velocity and pressure
χ	curvature
ω	angular frequency (in ${}^{rad}/_{s}$)
$[\omega MK]$	convention; equal to $[-\omega^2[M] + [K]]$
ω_n	resonant frequency

Subscripts

0	pertaining to equilibrium
$3N$	refers to the first $3N$ terms of expression
a	pertaining to the ambient surroundings
c	pertaining to feedback loop segment c or cold end
d	pertaining to feedback loop segment d
e	equivalent; a conventional subscript combining several others or pertaining to an individual element
ep	pertaining to an individual piezo element
i	entering regenerator or pertaining to inertance i
p	pertaining to piezo
r	pertaining to the regenerator
s	in-plane direction
t	pertaining to pulse tube segment t or hot end; thermal
z	pertaining to the z direction
C	cold end or critical value
H	hot end of regenerator
R	pertaining to resonator segment R
θ	hoop direction

Abbreviations

ANSYS	Analysis System
DeltaEC	Design Environment for Low-Amplitude ThermoAcoustic Energy Conversion
FEM	finite element model
FFT	fast Fourier transform
LabVIEW	Laboratory Virtual Instrument Engineering Workbench
MATLAB	Matrix Laboratory
PZT	Piezoelectric material (Lead-Zirconate-Titanate)
TWTAE	Traveling Wave ThermoAcoustic Engine
UMD	University of Maryland
VariAC	Variable Alternating Current

Chapter 1

Introduction

1.1 Overview

Traveling wave thermoacoustic engines (TWTAEs) are a type of heat engine operating on the Stirling cycle. Unlike traditional Stirling engines, the TWTAE does not have pistons, nor does it have moving parts. As a result, thermoacoustic Stirling engines have less viscous losses than Stirling engines with pistons, or other Stirling engine models with liquid pistons. The ultimate goal of these Stirling engines is to create an efficient and effective way to create electrical energy from waste heat.

As a heat engine which converts heat energy into acoustic energy, study of the TWTAE lies within the field of study known as thermoacoustics. This field also covers study of devices such as standing wave thermoacoustic engines and thermoacoustic refrigerators. One of the canonized texts on thermoacoustics was G.W. Swift's classical textbook [1].

Extensive efforts have been exerted to develop and analyze various configurations of thermo-acoustic engines [1]. The motivation behind these efforts is the fact that these engines are in effect clean, compact, environmentally friendly, and low cost devices. The Bell Telephone Laboratories (BTL) can be credited to the development of a "standing wave" class of such thermoacoustic engines whereby steady heat energy was transformed into self-sustained oscillating pressure waves which are then converted into electricity using reversed acoustical speakers [2], [3]. In spite of the simplicity and reliability of the BTL concepts, their conversion efficiency were relatively low (<10%) and the generated pressure oscillations were relatively weak. In order to overcome these limitations, Ceperley [4], [5] , introduced a radically different concept for achieving higher efficiencies whereby the produced acoustic waves were forced to undergo phasing similar to inherently reversible and thus highly efficient Stirling engine [6].The resulting class of thermoacoustic engines is called the traveling wave engines which will be the focus of this thesis.

Generally, the conversion of the acoustic energy into electricity is achieved by coupling the TWTAE with electromagnetic transducers of the moving-magnet type. This type of transducers are typically heavy and inefficient due to Joule heating resulting from the electrical resistance of the coil, eddy currents generated in the laminations around which the coil is wound, as well as to magnetic hysteresis in the lamination. Due to these serious limitations, the present thesis has attempted to consider piezoelectric transducers as a viable alternative for direct conversion of the acoustic energy into electricity because of their numerous attractive attributes. Distinct among these attributes, are their high conversion efficiency, light weight, and high reliability as they have no moving parts. Furthermore, piezoelectric transducers as they can operate efficiently at high frequencies, lead to the design of thermoacoustic engines with more compact acoustic resonators. Because of these distinct advantages, this thesis will focus on studying the characteristics of the efficient traveling wave thermoacoustic engines coupled with piezoelectric transducers in order to effectively harvest the thermal energy and convert it into electric energy.

1.2 Scope of the Thesis

The thesis is organized in nine chapters. In Chapter 2, a brief literature review is presented including some of the attempts to model the TWTAE such as the classical work of Yazaki [7], Backhaus and Swift [8], [9], and recently by A.T.A.M deWaele [10].

In his publication, deWaele presented a method for converting the TWTAE from a complicated continuous thermoacoustic system to a simplified discrete model where components of the TWTAE are replaced by lumped-parameter elements. This thesis reproduces the analysis performed by deWaele in Chapter 3 and in Appendix A. Further analysis is performed on a prototype of the TWTAE, which has been built at the Smart Systems Laboratory at the University of Maryland. By using the lumped-parameter approach, deWaele generated a fourth-order differential expression describing the behavior of the pressure within the engine. Also, deWaele presented a theory in which the transient behavior of the TWTAE, the regenerator hot-end temperature, and oscillating pressure amplitude are predicted.

The lumped-parameter model as theorized by A.T.A.M. deWaele is then furthered in Chapter 4 and Appendix B whereby an electrical analog of the traveling wave energy harvester is developed. By using the circuit analogy, the same fourth-order differential expression can be created, but with the added benefit of being easily integrated with other electrical elements. Chapter 4 presents also an analysis of the TWTAE combined with a piezoelectric disk attached to the end of the TWTAE resonator. By using the circuit analogy, the piezo disk's mechanical and electrical behavior is integrated into the circuit analogy for the TWTAE.

Chapter 5 presents an axisymmetric finite element model (FEM) of the piezoelectric disk coupled with an aluminum resonator cap. The method for the axisymmetric finite element model for the system is derived from sources published by K.C. Rocky *et al.* [11], and Ashida and Tauchert [12]. The developed FEM, is used to predict the resonant frequencies of the combined aluminum-piezo disk system is assessed, then compared with experimental results obtained by a laser vibrometer and white noise frequency response. Also, a two-port impedance matrix that describes the electro-mechanical coupling of the combined system is derived. This matrix is then used in the DeltaEC analysis developed in Chapter 6.

Chapter 6 presents a numerical analysis using DeltaEC (Design Environment for Low-Amplitude ThermoAcoustic Energy Conversion) [13]. By using DeltaEC, comparisons of the predictions of the pressure amplitude, operating frequency, and regenerator hot-end temperature are made against both the lumped-parameter analysis and the experimental results.

The results of the experimental setup described in Chapter 7 are discussed in Chapter 8. Chapter 8 also compares the pressure amplitudes, temperatures and frequencies determined theoretically from the lumped-parameter models, and from the numerical analysis from DeltaEC. MATLAB codes, ANSYS text files and extended derivations are included in the Appendices at the end of the thesis.

In this thesis, these theoretical transient plots are developed and compared with the experimental results measured by the pressure transducers and thermocouples attached to the prototype engine. These results are displayed in Chapter

8.

Chapter 9 summarizes the conclusions arrived at and sets forth the recommendations for future work and possible extensions of this thesis

Chapter 2

Literature Review

2.1 Overview

Research intoTWTAEs began when Ceperly [4] published a paper exploring the possibilities of a traveling acoustic wave passing through a regenerator. The source of the acoustic wave was a loudspeaker; therefore, the experiment was of a purely academic interest. Ceperly did however, present the idea of a thermoacoustic engine with a positive feedback loop where the regenerator would amplify its own spontaneous thermoacoustic oscillations. Ceperly, for a number of reasons, did not manage to record a power gain greater than one, but he managed to demonstrate the potential of traveling wave engines.

The TWTAE with a looped tube was constructed in 1998 by T. Yazaki *et al.* [7]. The paper published successfully demonstrated traveling wave engines superiority over standing wave engines. While the engine depicted in the paper did not have precisely the phase variation necessary to fully carry out the Stirling cycle, traveling wave oscillations demonstrated improved efficiency over their standing wave counterparts.

The TWTAE was greatly improved with Backhaus and Swift's design in 1999 [8],[9]. The design incorporated improvements such as the thermal buffer tube which removed heat and allowed only acoustic energy to pass into the feedback loop. The feedback loop itself was improved; its shape was altered to create the necessary phase variation needed to better carry out the Stirling cycle. Furthermore, its theoretical efficiency is reported at 0.3 which is very high for thermoacoustic engines.

Backhaus *et al.* in 2004 constructed an engine with the same components identified in the paper published with Swift in 1999 [14]. This engine connected with a linear alternator to generate electricity. Backhaus reported experimental efficiencies as high as 0.18.

In 2009, A.T.A.M. de Waele published a paper demonstrating a new method of modeling thermoacoustic engines [10]. Previously, most modeling was done using the circuit analogy of thermoacoustic components. This paper, however, decomposed the engine into lumped element components. With this method, a fourth-order differential equation was derived, and from this, operating properties were assessed.

2.2 Thermoacoustic Concepts and Prototypes

Several TWTAEs have been constructed and reported in literature. This section will report on the literature chronologically, focusing on physical constructions and prototypes. A particular emphasis will be placed on any predictive modeling performed by the publications, with experimentation and results following.

2.2.1 A pistonless Stirling engine-The traveling wave heat engine

In 1978 Peter H. Ceperly [4] published a paper entitled "A pistonless Stirling engine-The traveling wave heat engine." This paper attempted to determine the acoustic effects of an acoustic wave traveling through a regenerator where a temperature gradient was present. This paper discusses the viability of a Stirling engine operating using this concept, and discusses the differences between traveling wave thermoacoustics and the established standing wave engines. The paper reports an approximation for the theoretic behavior of a regenerator in a traveling wave, rather than the performance of a constructed traveling wave engine.

Concept

Unlike later concepts where a feedback loop in the engine provides the input acoustic energy for the regenerator, this study created the acoustic wave using a loudspeaker, operating at 190 Hz. This can be seen below in Figure 2.1.

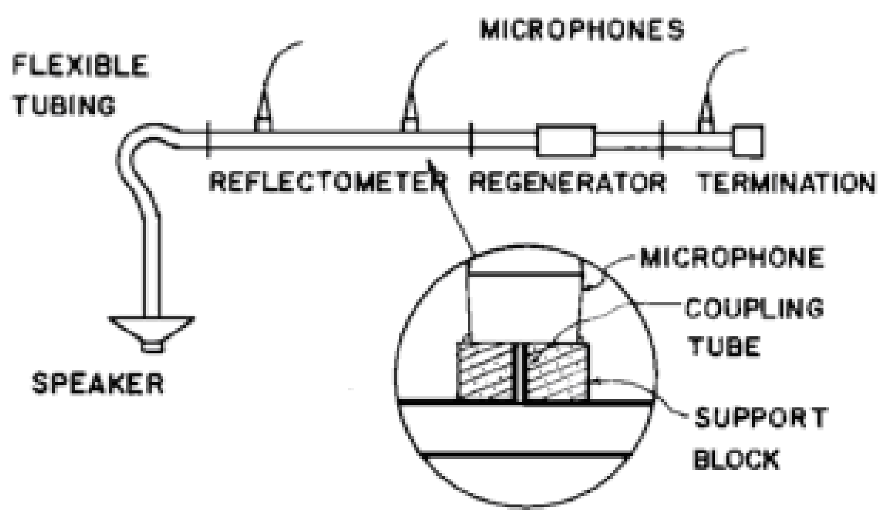

Figure 2.1: Setup of Ceperly's traveling wave heat engine study [4].

Also indicated in Figure 2.1 is the flexible tube, the section of tubing referred to in the paper as the reflectometer, and the regenerator. The approximate locations of the microphones used to record the gain of the regenerator are also shown. The flexible tubing is used to transmit sound from the loudspeaker, but not vibrations in the walls. The reflectometer is used to calibrate the gain measurements. The regenerator, which is designed to be shorter than the wavelength of the traveling wave, is made of steel wool and a heating element for creating the temperature gradient.

As mentioned before, Ceperly's setup was created for academic purposes, to study the gain of traveling acoustic waves through a regenerator. Ceperly proposed constructing a TWTAE, which includes a feedback loop to supply acoustic energy to the regenerator. This can be seen below in Figure 2.2.

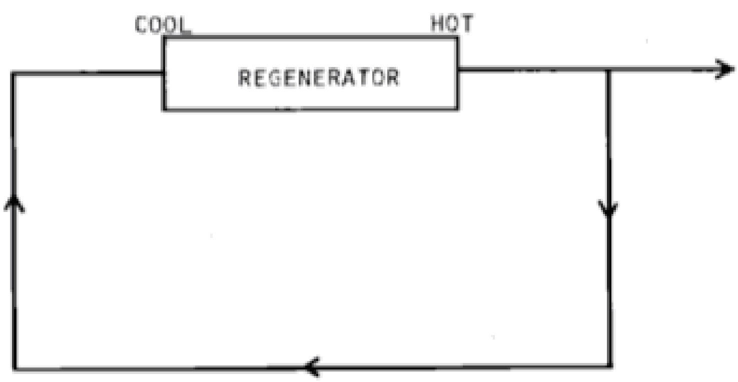

Figure 2.2: Ceperly's suggestion of a traveling wave engine with a positive feedback loop [4]

The design in Figure 2.2 was realized and analyzed by many future publications.

Modeling

The predictive model Ceperly employs in this paper is based on volumetric flow and power gains of the gas due to the temperature differential in the regenerator. The paper treats volumetric flow gain g as the ratio between volume flow entering the regenerator and that leaving the regenerator. By using the notation I_i as the volumetric flow entering the regenerator, and I_o as the volumetric flow leaving the regenerator:

$$g = \frac{I_o}{I_i} \tag{2.1}$$

Because the dimensions of the setup by Ceperly are all smaller than the wavelength of oscillations and because of conservation of mass, the mass flow rate entering the regenerator is assumed to be equal to the mass flow rate leaving the regenerator. By using the relationship for mass flow rate to volumetric flow rate [15]

$$\dot{m} = \rho I \tag{2.2}$$

where in Eq. (2.2), $\dot{m}$ is the mass flow rate and ρ is the density of the gas. Applying conservation of mass through the regenerator:

$$\dot{m}_i = \dot{m}_o \tag{2.3}$$

and applying Eq. (2.2) to Eq. (2.3):

$$\rho_i I_i = \rho_o I_o \tag{2.4}$$

Rearranging gives:

$$g = \frac{I_o}{I_i} = \frac{\rho_i}{\rho_o} \tag{2.5}$$

Ideal gas law states [15]:

$$\rho = \frac{Mp}{RT} \tag{2.6}$$

In Eq. (2.6) M is the molar mass of the gas, p is the pressure, R is the universal gas constant, and T is the temperature in Kelvins. Applying Eq. (2.6) to Eq. (2.5) yields:

$$g = \frac{p_i T_o}{p_o T_i} \tag{2.7}$$

Ceperly then uses an electrical analogy to simplify the expression for volumetric gain. This analogy entails treating volumetric flow as current, and pressure as voltage. This is discussed in greater detail in Chapter 4. The components of the engine then have equivalent resistance and often compliance or inductance. Ceperly treats the tubing as a resistance to flow R_t and the regenerator as both a resistor R_p and an amplifier. The lumped parameter electrical analogy for the model published can be seen in Fig. 2.3.

In the figure, the loudspeaker, the source of acoustic energy in the experiment, is represented by a sinusoidal voltage source. By using Ohm's law, it can be seen that if p_i is the pressure before the regenerator, and p_o is the pressure afterwards:

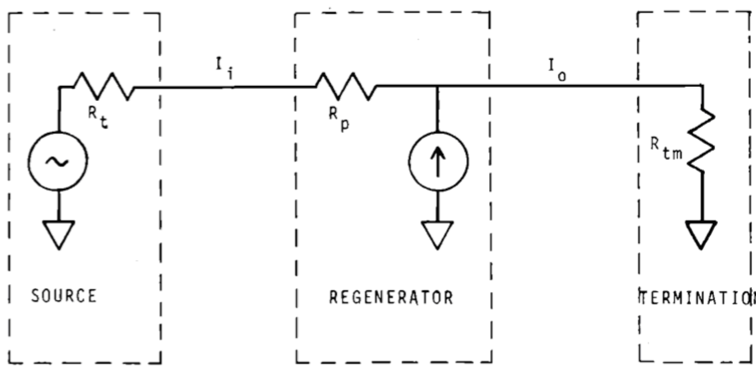

Figure 2.3: Lumped parameter model of Ceperly's thermoacoustic heat engine [4]

$$p_i = R_t I_i \tag{2.8}$$

and:

$$p_i - p_o = R_p I_i \tag{2.9}$$

Rearranging and substituting Eq. (2.8):

$$p_o = I_t(R_t - R_p) \tag{2.10}$$

Inserting into Eq. (2.7):

$$\begin{aligned} g &= \frac{R_t I_i T_o}{I_i \left(R_t - R_p\right) T_i} \\ &= \frac{T_o}{T_i}\left(1 - \frac{R_p}{R_t}\right)^{-1} \end{aligned} \tag{2.11}$$

Ceperly makes the assumption that that the flow resistance due to the regenerator (Rp) is much smaller than the resistance du to the tubing ($R_p \ll R_t$). This leads to Eq. (2.11) to be approximated as

$$\begin{aligned} g &= \frac{T_o}{T_i}\left(1 - \frac{R_p}{R_t}\right)^{-1} \\ &\approx \frac{T_o}{T_i}(1-0)^{-1} \\ &= \frac{T_o}{T_i} \end{aligned} \tag{2.12}$$

which leads to the relation

$$g = \frac{p_i T_o}{p_o T_i} \approx \frac{T_o}{T_i} \tag{2.13}$$

which implies the following approximation

$$\frac{p_i}{p_o} \approx 1 \tag{2.14}$$

Because of this, the power gain G, defined as the ratio of output to input power can be approximated as:

$$G = \frac{p_o I_o}{p_i I_i} \tag{2.15}$$

Therefore, incorporating Eq. (2.15) into Eq. (2.1) yields the following approximation:

$$G \approx g \approx \frac{T_o}{T_i} \tag{2.16}$$

Results

By using eq. (2.16), estimations for the power gain of the regenerator are easy to predict using the temperatures of the hot and ambient heat exchangers on either side of the regenerator. By using three microphones, one to measure the acoustic power moving towards the regenerator, acoustic power reflected from the regenerator, and the power transmitted through the regenerator, the power gain was measured. Theoretic gain was measured as:

$$G_{measured} = \frac{P_{out}}{P_{in} - P_{reflected}} \tag{2.17}$$

Listed in Table 2.1 is the chart of results obtained by Ceperly from his experimentation.

Temperatures			$G_{measured}$		
Input (°C)	Output (°C)	Difference (°C)	Theoretically expected gain	Measured Gain	Measured gain normalized by first entry
90	90	0	1.00	0.81	1.00
150	90	-60	0.86	0.70	0.86
90	150	+60	1.16	0.90	1.11

Table 2.1: Results of gain measurements from Ceperly traveling thermoacoustic wave study [4]

The measurements depicted in Table 2.1 are for 3 separate situations. The first row of the figure represents the situation where the input and output are heated to the same temperature, and there is no temperature differential. The 2nd row represents the situation where the gain is expected to be less than one, in other words, the temperature gradient dampens the acoustic energy entering the regenerator. The 3rd row represents the situation where positive gain is expected. As can be seen from the figure, the regenerator behaves as expected. When the regenerator is oriented as a damper, the acoustic power is damped relative to the first row where no gradient is present. When the regenerator is oriented such that acoustic power is expected to be amplified, this is indeed the case, relative to the first row where no gradient is present.

Because the measured gain does not match the theoretic gain due to unaccounted losses, the model represented is not a very accurate prediction for the behavior of a traveling wave thermoacoustic engine. Possible ways to improve power gain would be to use a higher temperature gradient, and to match the source frequency to the resonant frequency of the apparatus. A way to improve the fidelity of the model would be to more accurately predict the losses due to the regenerator.

2.2.2 Traveling Wave Thermoacoustic Engine in a Looped Tube

In 1998, T. Yazaki *et al.* [7] published a paper entitled "Traveling Wave Thermoacoustic Engine in a Looped Tube." This paper reported the construction of a looped tube with a differentially heated regenerator, similar to the designed by Ceperly in an earlier paper, seen in Fig. 2.2. This tube acts as a pistonless Stirling engine; a traveling wave engine. Unlike Ceperly's experiment, where a loudspeaker was used, the acoustic energy is provided by spontaneous oscillations in the regenerator. The looped tube allows positive feedback of the acoustic energy. The energy returns to the cold end of the regenerator and amplifies the acoustic wave. A schematic for Yazaki's looped Stirling engine is seen in Fig. 2.4.

Prototype

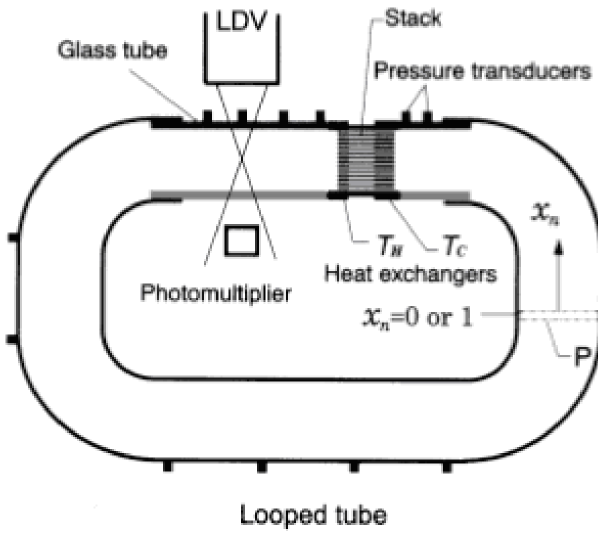

Figure 2.4: Yazaki's looped tube with differentially heated regenerator [7]

The tube shown in Fig. 2.4 is constructed mainly of 20.1 mm inner radius tubing, with a section of 18.5 mm inner radius glass tubing. The glass is included in order to use a laser Doppler velocimetry to measure the velocity of the working gas. Heat exchangers are attached to the wall of the tube at T_H and T_C at either end of the regenerator. Pressure sensors were placed along the wall at different points with the goal of identifying the wavelength and direction of wave propagation.

Results

The set up was built in order to observe two characteristic variables of thermoacoustic engines: onset spontaneous oscillation temperature ratio T_H/T_C, and the phase difference between velocity and pressure Φ at various locations around the tube.

It is assumed that spontaneous oscillations are initiated when the difference across the regenerator is great enough, or in other words, when the ratio of ${}^{T_H}/_{T_C}$ is large enough. The paper then attempted to experimentally plot the relationship between the parameter $\omega\tau$ and the ratio ${}^{T_H}/_{T_C}$. The variable ω represents the angular frequency of the gas oscillation and was determined experimentally for each measurement. The variable τ is defined as the time required for thermal equilibrium in the cross section of the flow channel. It is also defined as:

$$\tau = \frac{r^2}{2\alpha} \tag{2.18}$$

In Eq. (2.18), α is the thermal diffusivity of gas, defined as:

$$\alpha = \frac{\kappa}{c_p \rho_m} \tag{2.19}$$

In this equation, κ is the thermal conductivity, c_p is the thermal capacity, and ρ_m is the mean density of the gas. For measurements, the temperature $\frac{(TH+TC)}{2}$ was used to determine these values. In order to vary $\omega\tau$, the pressure was increased, thereby increasing ρ_m, reducing α, and finally increasing τ. Seen below in Fig. 2.5 is the log-log plot of the measured ratio ${}^{T_H}/_{T_C}$ which initiates oscillations for each $\omega\tau$.

From the plot, for each value of $\omega\tau$, the ratio ${}^{T_H}/_{T_C}$ above which spontaneous oscillation occurs is seen. This plot can be used to determine whether spontaneous

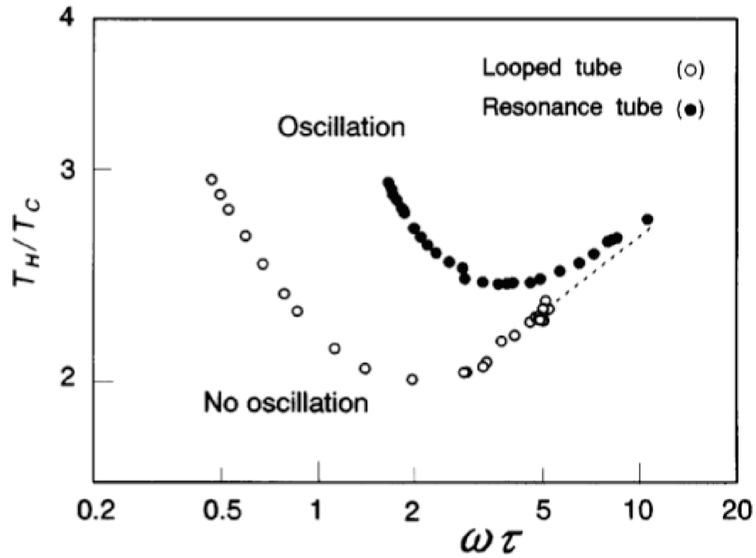

Figure 2.5: Yazaki's log-log plot of onset temperature ratio with respect to operating frequency [7].

oscillations due to engine operating conditions are expected to occur. Also, the value for $\omega\tau$ that minimizes the ratio T_H/T_C needed is experimentally can be approximated. Finally, it was noted that the ratio T_H/T_C needed to generate spontaneous oscillations is reduced for a traveling wave engine as opposed to a standing wave engine. The comparison was made by repeating measurements yet putting a stiff barrier in the engine thereby changing the looped engine to a standing wave engine.

By using the twenty-four pressure transducers located at various points around the loop (transducer locations can be seen in Fig. 2.4), both the phase variation between the volumetric velocity and pressure are measured, as well as work flow at multiple points in the loop. Fig. 2.6 represents these plots versus location in the loop for both the standing wave engine and traveling wave engine.

In both plots the location of the regenerator is depicted. It has been well

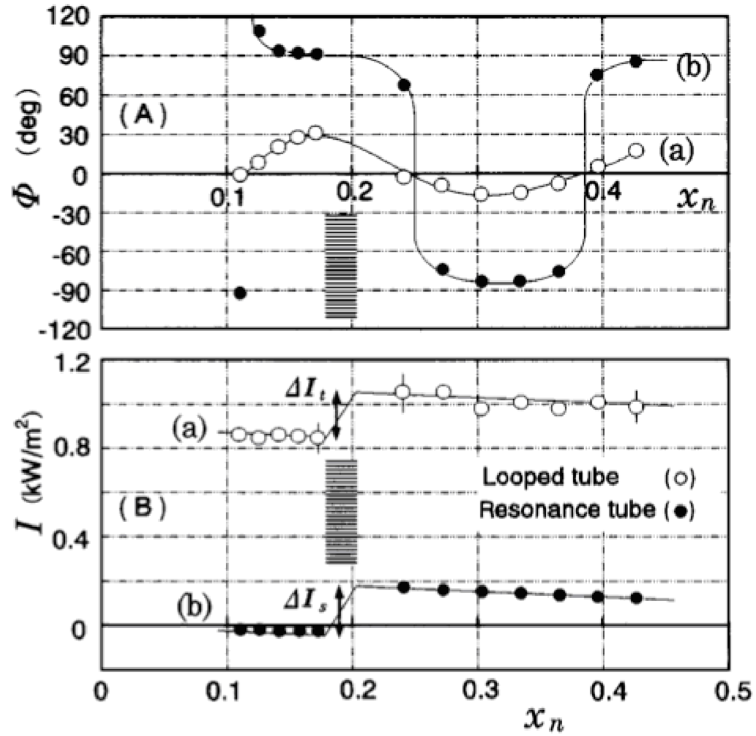

Figure 2.6: Yazaki's plot of phase and work flow versus position on looped tube [7].

documented that traveling wave engines can be more efficient and powerful than standing wave engines and the lower of the two plots clearly confirms this assumption. The increase in work flow denoted by ΔI is similar for both the standing wave and traveling wave engine, but the work flow is higher for traveling wave engine varieties. The top plot demonstrates the flaws in Yakazi's design for a traveling wave engine. As can be seen, for the traveling wave engine, and specifically about the regenerator, the phase variation (Φ) is not 0. This is problematic because it is required that phase variation (Φ) be as close to zero as possible about the regenerator for the efficient Stirling cycle to be leveraged. This problem has been solved in later papers by introducing non-uniform tube sections in an attempt to tune the phase variation for their engine.

2.2.3 A thermoacoustic Stirling heat engine and A thermoacoustic-Stirling Engine: Detailed study

In 1999, S. Backhaus and G.W. Swift published papers entitled “A thermoacoustic Stirling heat engine” [8] and also “A thermoacoustic-Stirling heat engine: Detailed study” [9] where they construct a TWTAE which involves many improvements over Yazaki’s design. These include a resonator section of the engine, inertance in the feedback loop, and a buffer tube with a 2^{nd} heat exchanger. The two published papers report on the same engine. The schematic for the heat engine can be seen in Fig. 2.7.

Prototype

The inertance and compliance in the feedback loop influences the phase of the acoustic wave fed back through to the regenerator so that the working gas more closely undergoes the Stirling cycle. This design also includes a 2^{nd} cold exchanger and a buffer tube, preventing heat from the hot end of the regenerator from escaping into the feedback loop and resonator. The regenerator is made up of 120 mesh stainless steel screens. The overall hydraulic radius of the regenerator is ~ 42 μm, which is smaller than the thermal penetration depth of helium pressurized to 30 bar, estimated at 300 μm. While operating, the engine produces acoustic oscillations at 80 Hz.

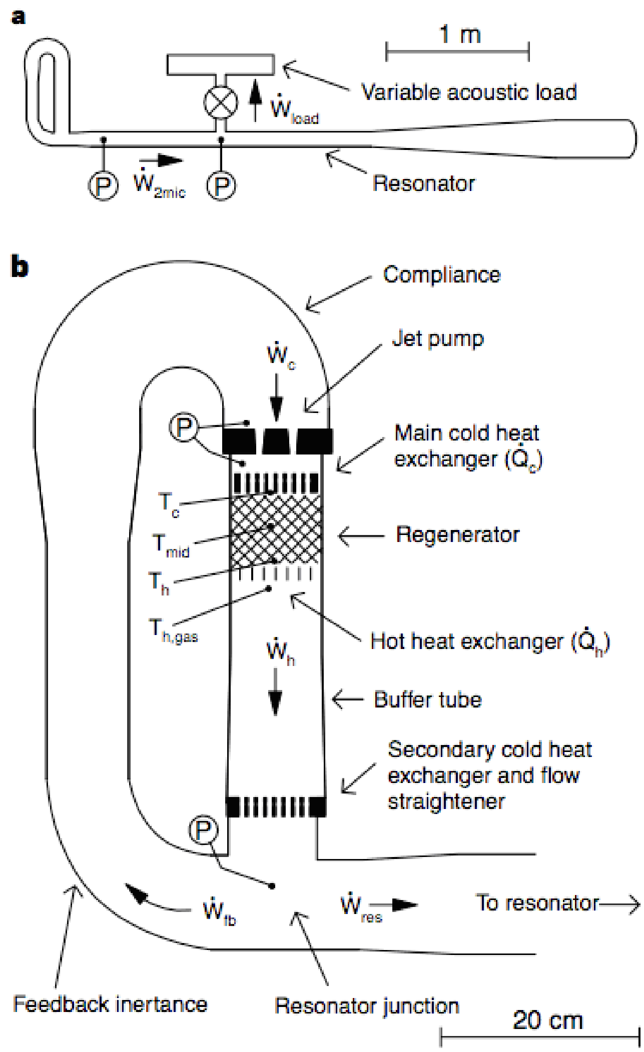

Figure 2.7: Backhaus and Swift's thermoacoustic traveling wave heat engine. a) Scale drawing of engine. b) Close up of looped torus shaped section of engine [8]

Modeling

Backhaus and Swift's design was inventive in that they attempted to use the feedback loop geometry to adjust the phase difference between the volume velocity and acoustic pressure at the regenerator. The way in which this was done included a narrower section in the feedback loop creating an inertance and an expanded section to create a compliance. Afterwards, using circuit analysis to manipulate the frequency response of the system to improve its performance. Fig. 2.8 depicts the circuit analogy of the engine displayed in Fig. 2.7.

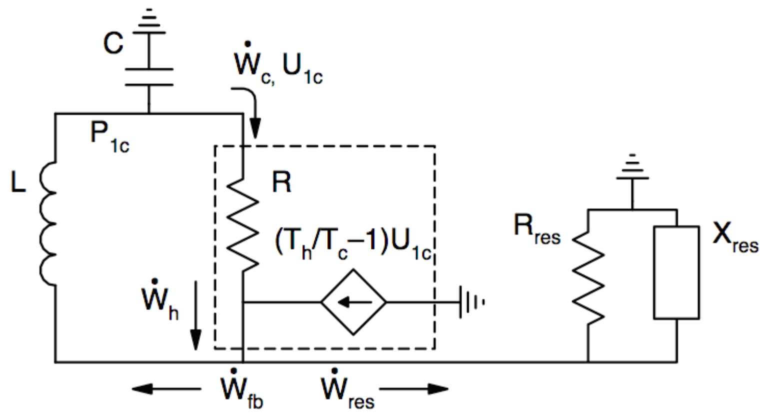

Figure 2.8: Circuit analogy for Backhaus and Swift's traveling wave thermoacoustic engine [8]

In the circuit analogy, as discussed by Ceperly, the current in the circuit is equated to volumetric velocity, and the voltage is equated to pressure. By using the expression for volumetric velocity gain in the regenerator determined by Ceperly [4], where the regenerator provides a volumetric velocity input of

$$U_{regen} = U_{1c}\left(\frac{T_h}{T_c} - 1\right) \tag{2.20}$$

Backhaus and Swift then attempt to solve for U_{1c}, the volumetric velocity entering the cold end of the regenerator. The expression derived is reported as

$$U_{1c} = \frac{\omega^2 LC}{R}\frac{p_{1c}}{1 + i\omega L/R} \tag{2.21}$$

In Eq. (2.22), p_{1c} refers to the pressure in the engine immediately before the cold end of the regenerator. The term L is the inertance of the feedback loop, and the terms C is the compliance of the feedback loop. The term R is defined as the flow resistance due to the regenerator. The equation derived is independent of temperatures T_h and T_c, and is dependant only on geometry of the engine. It is noted in the paper that if ωL is small in comparison with R, then by looking at the denominator on the right hand side, it can be seen that U_{1c} becomes in phase with p_{1c}, which is the phasing requirement for the Stirling cycle. The paper reports this as a suggested method for adjusting the phasing of the engine. Furthermore, the relationship between the volumetric flow into the feedback loop and the volumetric flow into the regenerator is given:

$$\frac{U_{1c}}{U_f b} = \frac{\omega L}{R} \tag{2.22}$$

This implies that as L increases relative to R, the volumetric flow through the regenerator, U_{1c}, increases as well.

Results

The papers by Backhaus and Swift [8], [9] report on the efficiency and output power of their design and attempt to demonstrate the viability of traveling wave thermoacoustic engines. By using strategically placed microphones, Backhaus and Swift attempted to measure the power delivered to the resonator- the location where the energy will be harvested- versus the temperature of the hot heat exchanger. This graph is represented in Fig. 2.9.

Fig. 2.9 is a plot of the thermal efficiency, η, measured as the power delivered

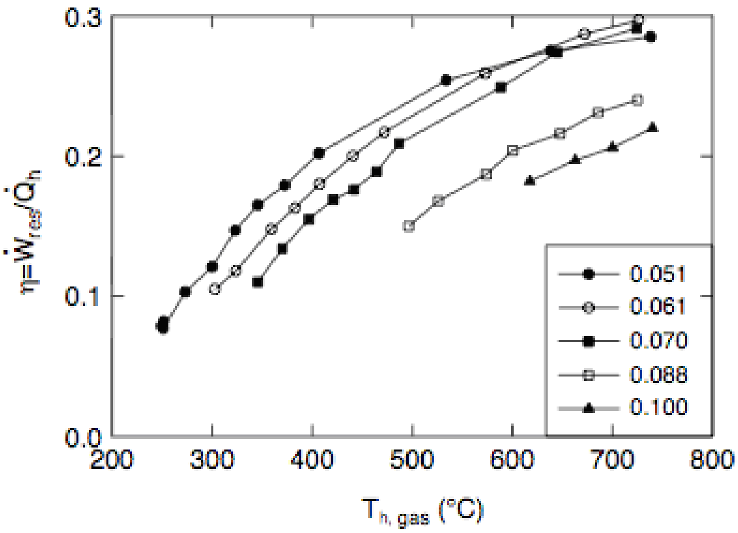

Figure 2.9: Backhaus and Swift plot of engine efficiency vs. hot heat exchanger temperature [8]

to the resonator, $\dot{W}_{res}$, divided by power needed to heat the hot heat exchanger, $\dot{Q}_h$, to the temperature shown on the x-axis. The figure also plotted the efficiency across different size openings for the jet pump located before the cold heat exchanger of the regenerator. Based on the plots, it appears that a smaller opening can improve efficiency of the engine despite an increase in flow resistance; an interesting connection.

Backhaus and Swift [9], through a variety of techniques such as measuring and computer analysis attempted to determine the amount of power that is lost through different components of the engine. Their tabulations can be seen in Table 2.2. As expected, the greatest power loss is due to the regenerator both through viscous losses due to a tightly packed regenerator, and to thermal losses due to heat removed by the cold heat exchangers. Power is also lost due to the high temperature used; a steep temperature gradient between the hot heat exchanger and the ambient room is created.

			$p_{ref}/p_m = 0.061$ $T_{h,gas} = 725°C$		$p_{ref}/p_m = 0.10$ $T_{h,gas} = 725°C$	
Element	Process	Method	$\dot{X}_{lost}\,(W)$	Fraction	$\dot{X}_{lost}\,(W)$	Fraction
Regenerator	Viscous/Thermal loss	DeltaE	238	0.14	393	0.13
	Heat leak	Measured	163	0.09	172	0.06
Feedback inertance	minor loss	DeltaE	62	0.04	296	0.10
	Viscous/Thermal loss	DeltaE	36	0.092	145	0.05
Thermal buffer tube	Residual streaming	Measured	82	0.05	25	0.01
	Radiation	Measured	69	0.04	78	0.03
	Metallic conduction	Measured	52	0.03	55	0.02
	Boundary-layer transport	DeltaE	7	<0.01	18	¡0.01
	Flow straightener	DeltaE	2	<0.01	12	<0.01
Insulation	Heat leak	Measured	82	0.05	87	0.03
Main cold heat exchanger	Temperature difference	Measured	57	0.03	181	0.06
	Viscous loss	DeltaE	4	<0.01	11	<0.01
Sec. cold heat exchanger	Minor/Viscous loss	DeltaE	34	0.02	144	0.05
Jet pump	Minor/Viscous loss	DeltaE	30	0.02	130	0.04
Resonator and load	Delivered power	Measured	710	0.41	890	0.30
Input energy	$(1 - T_{hhx}/T_{water})\,\dot{Q}_h$	Measured	1724	1.00	2968	1.00
Unaccounted $\dot{W}_{lost}$			44	0.03	200	0.07

Table 2.2: Backhaus and Swift's calculated losses in traveling wave engine due to individual components [9]

Backhaus and Swift accomplish many things with the two paper published in 1999. They devised a method using the geometry of the feedback loop to improve and tune the power output and efficiency of a traveling wave thermoacoustic engine. The paper reports values for efficiency and power. Specifically they report for their engine design that at its most efficient, 710 W were delivered with an efficiency of 0.3, while at its most powerful, 890 W were delivered with an efficiency of 0.22. There is a good effort at determining specific losses due to individual components of the engine.

While a method of tuning the phasing and output power of the engine using the geometry of the feedback loop is proposed, direct analytical expressions for the inertance and compliance of the feedback loop based on engine geometry are not determined in these publications. These are required to better analyze the engine.

2.2.4 Acoustic field in a thermoacoustic Stirling engine having a looped tube and resonator

Yuki Ueda, Tetsushi Biwa, Uichiro Mizutani and Tachi Yazaki [16] published another paper in 2002 entitled “Acoustic field in a thermoacoustic Stirling engine having a looped tube and resonator.” The paper reports construction of a traveling wave thermoacoustic engine for the purpose of measuring pressure, velocity, and the phase difference between the two different points within the engine. The schematic for this engine can be seen in Fig. 2.10.

Prototype

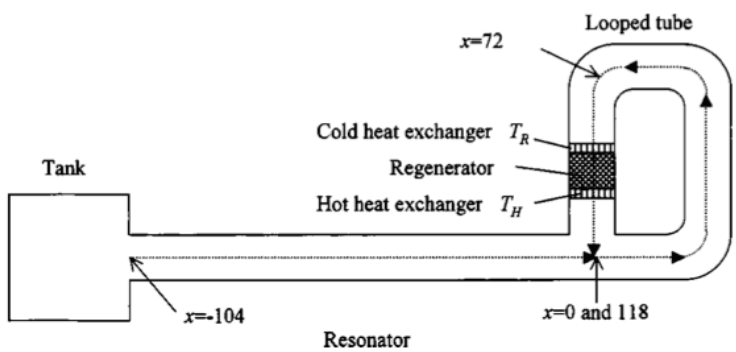

Figure 2.10: Traveling wave thermoacoustic engine built by Yuki Ueda *et al.* [16]

Ueda’s engine is much closer to the engine built by Yazaki in 1998 than the engine built by Swift and Backhaus in 1999. It is a relatively simple construction with a Pyrex loop and resonator of uniform 40 mm diameter cross section. Unlike Swift and Backhaus’ construction, there is no inertance or compliance in the feedback loop, and no buffer tube to return the gas temperature to ambient in the looped tube and resonator.

Results

Pressure and velocity measurements taken by Ueda *et al.* were performed along the center axis depicted in Fig. 2.10. The plots associated with these measurements seen below in Fig. 2.11 begin at $x = -104$, which based on Fig. 2.10 is the very end of the resonator where it meets the reservoir tank. Then the value of x increases along the resonator to the torus section of the engine and travels counter-clockwise around the loop. In Fig. 2.11, the regenerator location is indicated. Pressure measurements were taken using pressure sensors at the ends of thin tubes attached to various locations around the engine. The cross -sectional mean velocity was measured using a laser Doppler velocimeter. The pressure (p) and velocity (U) were recorded simultaneously, and phase variation (Φ) with respect to location is also recorded. By using these measured values, work flow (I) was calculated and plotted using the following relationship:

$$I = \frac{1}{2} Apu \cos(\Phi) \tag{2.23}$$

In Eq. (2.23), A refers to the cross sectional area, p refers to pressure, u represents mean velocity, and represents phase variations.

Because the cross section of the torus section is uniform, the phase was not tuned as closely as possible to match the ideal Stirling phase variation ($\Phi = 0$). As a result, the second plot depicts a phase variation of approximately -20° about the regenerator. Also of note, the work flow rate in the resonator is nearly zero for the length of the resonator. While Swift and Backhaus managed to direct a large

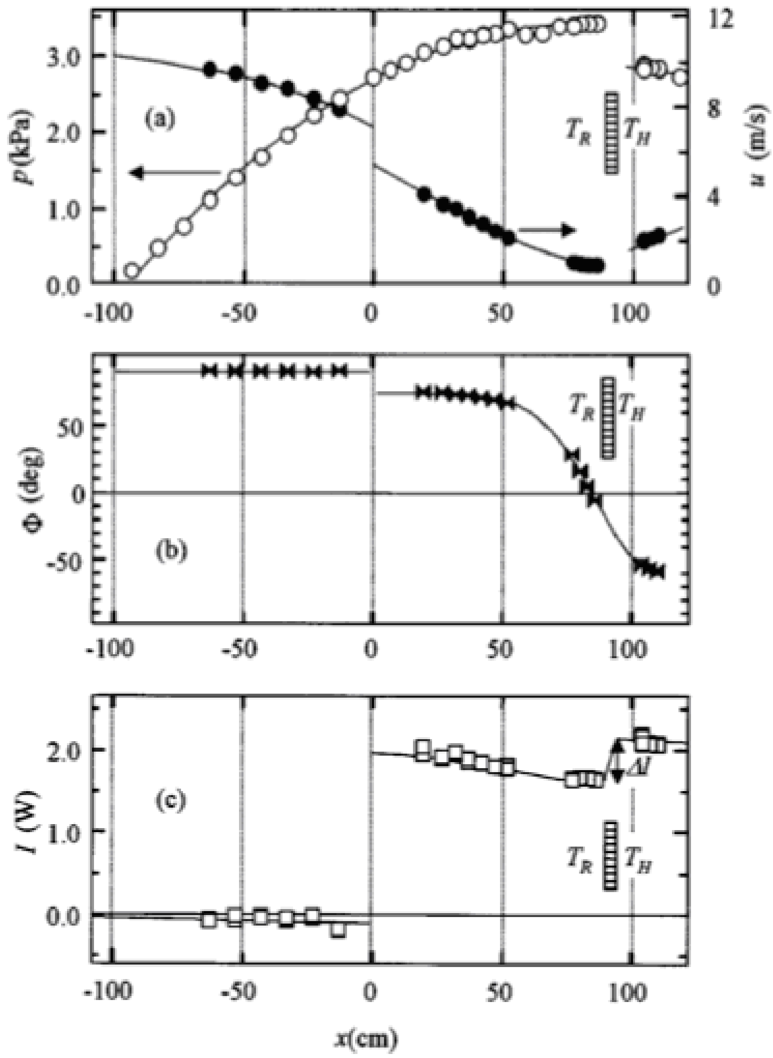

Figure 2.11: Ueda's plot of pressure amplitude, phase difference, and work flow vs. position [16].

amount of acoustic energy into the resonator, very little is reported in this paper. Ueda *et al.* make the claim that the negative phase change about the regenerator plays an important role in creating a large ΔI across the regenerator, but this claim is largely unsupported.

2.2.5 ‘Work flow measurements in a thermoacoustic engine

In 2001 Yuki Ueda, Tetsushi Biwa, Uichiro Mizutani and Tachi Yazaki [17] published a paper that outlined the method for experimentation used in their 2002 study. The paper, entitled “Work flow measurements in a thermoacoustic engine” reports on pressure and velocity measurements for a TWTAE similar to the one published in the 2002 paper but with slight differences. The diagram for their engine can be seen below in Fig. 2.12.

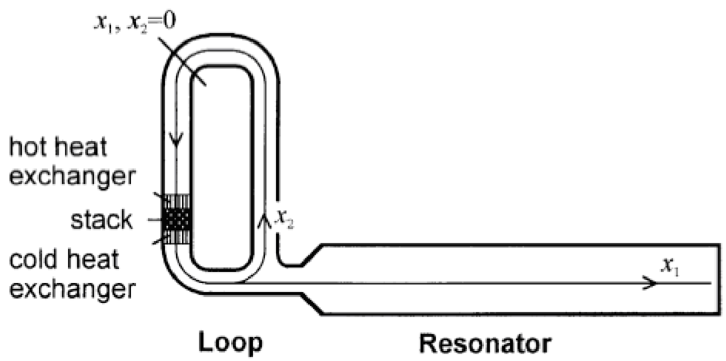

Figure 2.12: T. Biwa, Y. Ueda, T. Yazaki, U. Mizutani's traveling wave thermoacoustic engine [17]

The looped tube is made of uniform 37 mm inner diameter Pyrex with three copper elbows and one copper t-shaped joints. The resonator has a 78 mm inner diameter. The 35 mm regenerator is made up of a ceramic stack with 1.03×1.03 mm square channels. Some important differences between this design and the one reported in 2002 are the size and shape of the resonator, and the location of the regenerator with respect to the resonator and feedback loop.

Results

By using pressure transducers, the pressure amplitude is recorded along both x_1 and x_2. The two variables begin in the same location indicated above in Fig. 2.12. The variable x_1 then travels along the resonator to its termination, while x_2 returns to the origin via the feedback loop. The plot of pressure versus position can be seen in Fig. 2.13.

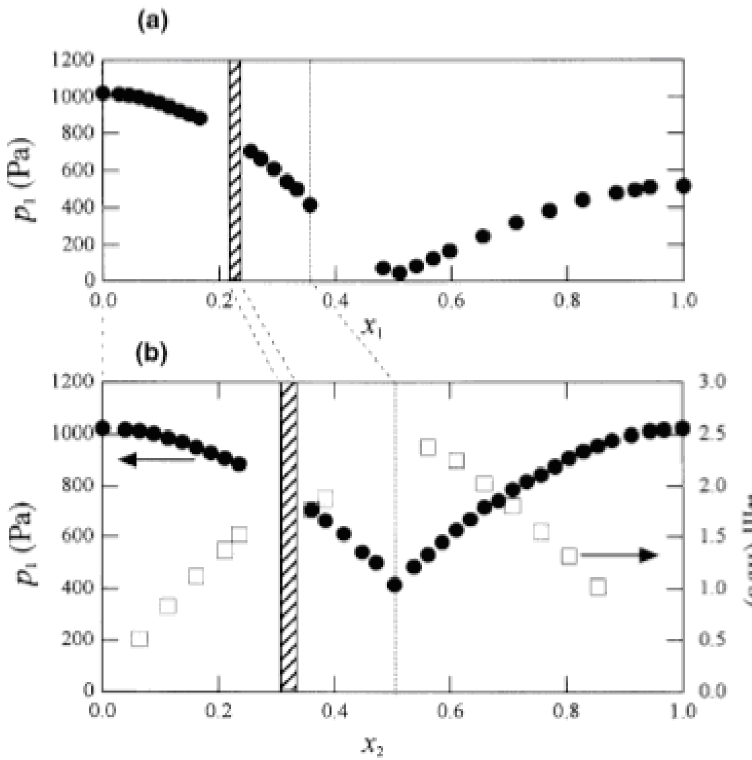

Figure 2.13: Biwa's plot of pressure amplitude vs. position [17]

As seen in the image, x_1 and x_2 are identical until the two axes diverge at the dashed line. As can be seen, x_1, which travels along the resonator, possesses standing wave modes as evidenced by the pressure node. The pressure along x_2 gradually returns to the initial pressure amplitude of the origin.

2.2.5.1 Investigation on traveling wave thermoacoustic heat engine with high pressure amplitude

D. Sun, L. Qiu, W. Zhang, W. Yan and G. Chen [18] published a paper, in 2004, entitled "Investigation on traveling wave thermoacoustic heat engine with high pressure amplitude." The paper reports construction of a traveling wave thermoacoustic engine that possesses similar components to that designed by Backhaus and Swift seen in Figure 9. The purpose of their engine was to attempt to find a relationship between filling pressure, heating power, and the pressure amplitude at various points in the engine. The schematic for the engine constructed by Sun *et al.* can be seen in Fig. 2.14.

Concept

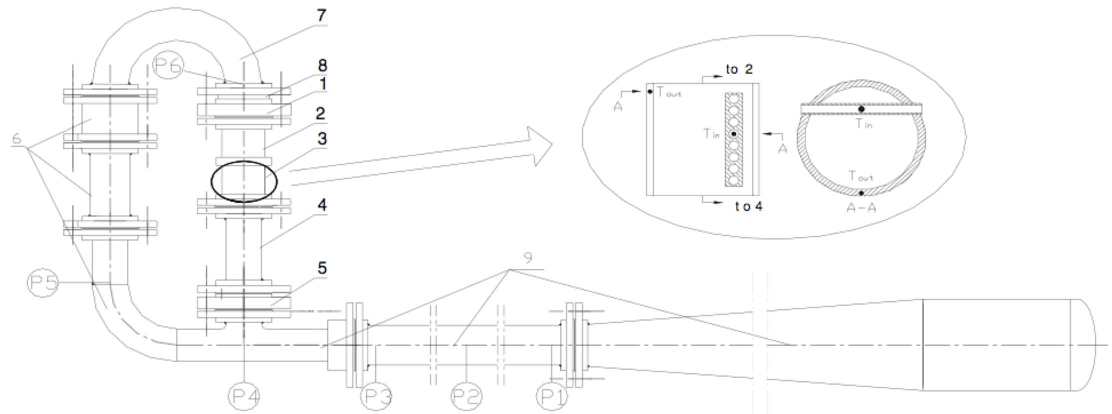

Figure 2.14: Traveling wave thermoacoustic engine built by D. Sun, L. Qiu, W. Zhang, G. Chen [18]

Fig. 2.14 shows the traveling wave thermoacoustic engines cooling heat exchanger (1), the thermal buffer tube (4), the secondary cooling exchanger at the bottom of the buffer tube (5), the feedback tubes (6), the compliance (7), jet pump (8), and straightener tubes (9). The feedback and compliance tubes are not shaped in a beneficial manner Backhaus and Swifts engine to achieve the correct Stirling zero phase difference between the velocity and the pressure. Backhaus and Swift install both a narrower section (inertance) and a wider section (compliance) in the feedback loop to accomplish this. The regenerator (2) and heater (3) is shown in more detail below in Fig. 2.15. The points where pressure amplitudes were measured are labeled P1-P6.

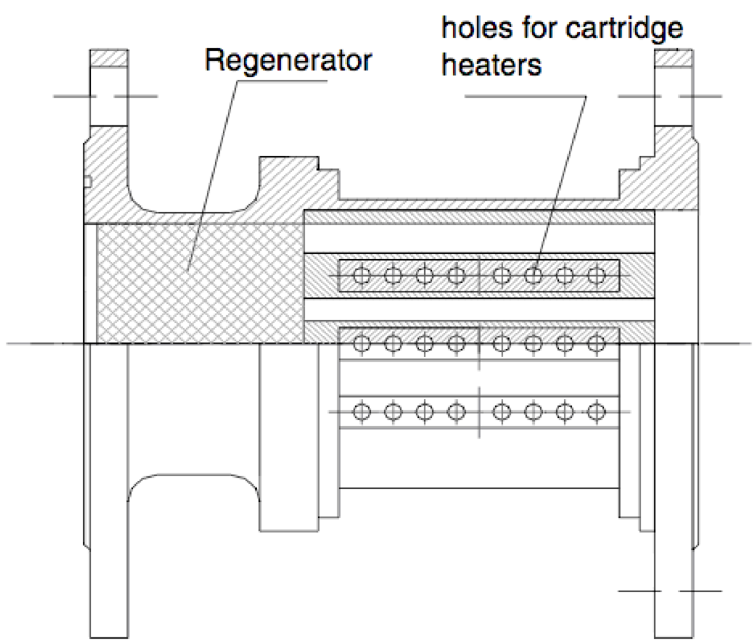

Figure 2.15: Side view of regenerator and heater in traveling wave thermoacoustic engine built by D. Sun *et al.* [18]

Fig. 2.15 shows the schematic of the relative locations of the 70 mm long regenerator and the 100 mm long heater to one another. The heater has 24 holes where heating cartridges are placed. The regenerator was made by cutting rectangular channels into a stainless steel cylinder.

Results

As depicted in Fig. 2.14, pressure was recorded at five locations about the engine. By using these pressure readings, a transient plot of pressure versus time was generated. This can be seen below in Fig. 2.16.

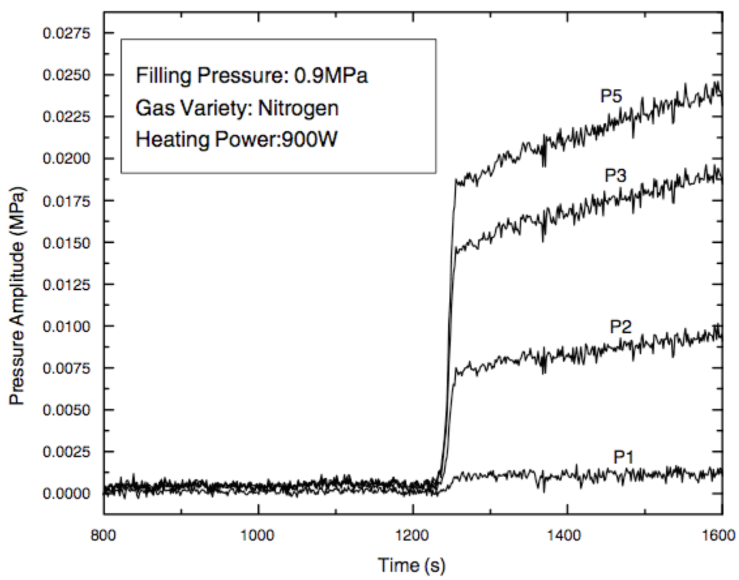

Figure 2.16: D. Sun *et al.*'s transient pressure amplitude vs. time plot [18]

In Fig. 2.16, the transient pressure chart of a traveling wave engine warming up from ambient temperature, a demonstration of spontaneous oscillations present in regenerators is shown. After heating the regenerator at 900 W using the 24 heater cartridges, the threshold temperature was met and oscillations spontaneously occur at approximately 1200s. As the temperatures continued to increase, so did the pressure amplitudes for the five pressure sensor locations.

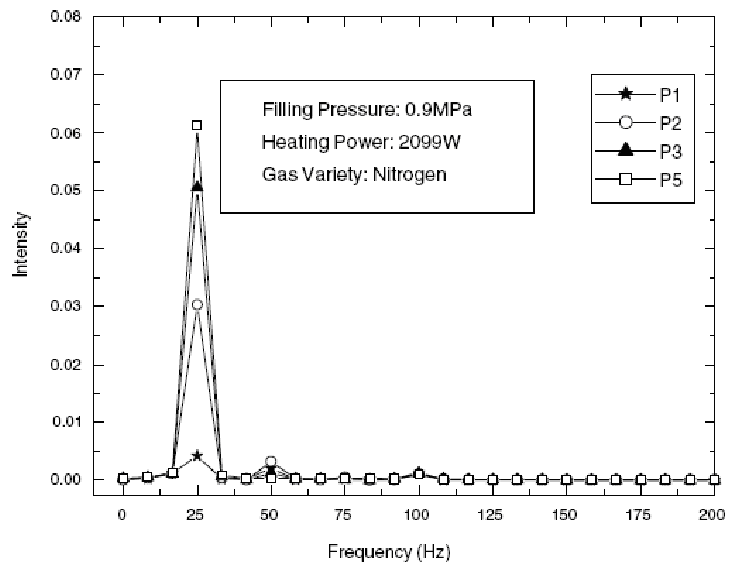

Figure 2.17: Spectral analysis of D. Sun's traveling wave thermoacoustic engine [18]

Fig. 2.17 presents the spectral plots of the TWTAE. In the plot, the first three resonant modes of the system as a whole are clear. Attempts at analytically modeling the TWTAE are absent from this publication.

2.3 Summary

This chapter has presented a brief summary of the basics of traveling wave thermoacoustic engines and their typical design features as well as their performance characteristics.

Chapter 3

Lumped-Parameter Model of the TWTAE

The modeling method that will be most closely inspected is the lumped-paramter approach derived by A.T.A.M. de Waele [10] in a paper published in 2009. The paper begins with the thermoacoustic engine described by Backhaus and Swift [8],[9] in 1999. The labeled schematic can be seen in Fig. 3.1

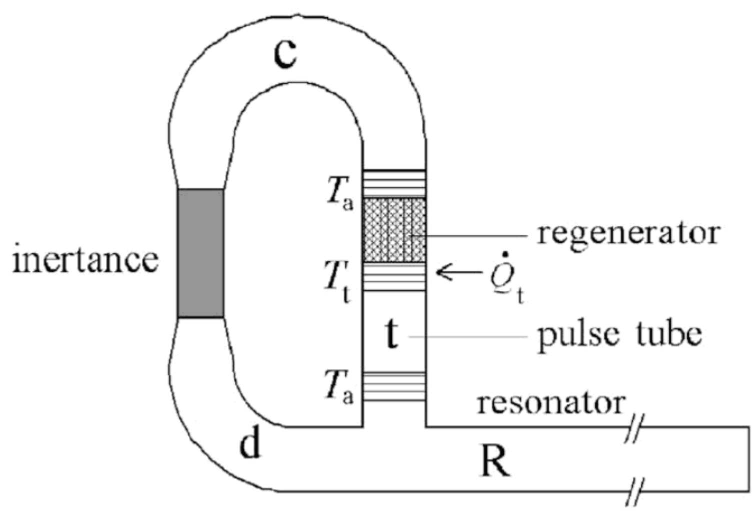

Figure 3.1: Diagram of model traveling wave thermoacoustic engine analyzed by A.T.A.M. de Waele [10].

The sections labeled in the figure are the compliance tube (c), the connecting tube (d), the pulse tube (t), and the resonance tube (R). The inertance and regenerator are also shown. Because the dimensions of the engine are smaller than the wavelength if the oscillations, it is assumed that the system can decomposed into discrete compartments. The connecting tube, the compliance, and the pulse tube, labeled (c), (d), and (t) respectively, are transformed into discrete volumes connected by isobaric tubes. The inertance is transformed into a piston whose mass (M_i) is that of the gas within its volume. The resonance tube is transformed into a piston, whose mass (M_R) is that of the gas within the resonance tubes volume. The diagram of the transformed system is shown in Fig. 3.2.

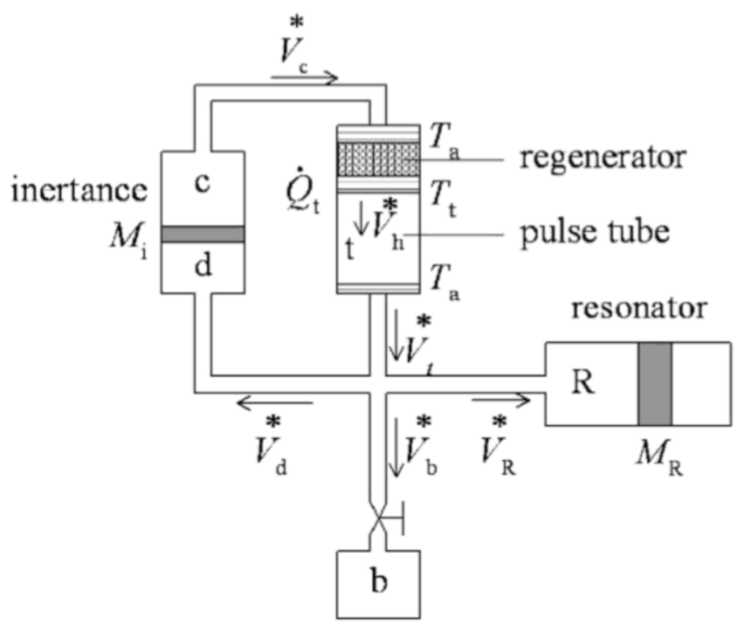

Figure 3.2: Discretized model of traveling wave thermoacoustic engine analyzed by de Waele [10].

In the figure, the regenerator and the three heat exchangers (T_t representing the hot exchanger, and T_a representing the ambient heat exchangers) hold over from Fig. 3.1. The component labeled (b) represents a buffer volume and accounts for losses in the system. The volume (b) is connected by a valve with flow conductance C. As a convention, volumes the pressures in volumes (c), (d), (t) are defined as p_c, p_d, and p_t respectively. The terms $\overset{*}{V}_c$, $\overset{*}{V}_d$, $\overset{*}{V}_t$, and $\overset{*}{V}_b$, all denoted with an asterisk, represent volume flow rates depicted at various points in Fig. 3.2. By assumption, because volumes (d), (t), and (R) are connected by frictionless, isobaric tubes. In Appendix A, the derivation of the single fourth-order differential expression which defines the pressure δp_t is shown. This expression, repeated below is:

$$0 = \frac{d^4 \delta p_t}{dt^4} + a_3 \frac{d^3 \delta p_t}{dt^3} + a_2 \frac{d^2 \delta p_t}{dt^2} + a_1 \frac{d \delta p_t}{dt} + a_0 \delta p_t \tag{3.1}$$

Where:

$$\begin{aligned} a_3 &= w_e C_0 + \tau_t w_e C_r + w_c C_r \\ a_2 &= w_e a_R + w_c C_r w_e C_0 + (w_e + w_c) a_i \\ a_1 &= w_c C_r w_e a_R + w_c a_i w_e C_0 \\ a_0 &= w_c a_i w_e a_R \end{aligned} \tag{3.2}$$

The only variable in this expression is τ_c, the critical temperature ratio. Replacing $\frac{d\delta p_t}{dt}$ with $P_t s$, and rearranging Eq. (3.1):

$$P_t \left(\frac{-a_3 s^3}{s^4 + a_2 s^2 + a_1 s + a_0} \right) = 1 \tag{3.3}$$

3.1 Typical Performance Characteristics

Fig. 3.3 displays the root locus plot for Eq. (3.3). By using a_3 as the gain for the root locus plot, the point on the root locus plot where the graph crosses the $j\omega$ will give the point where the system becomes unstable, that is to say, where oscillations begin.

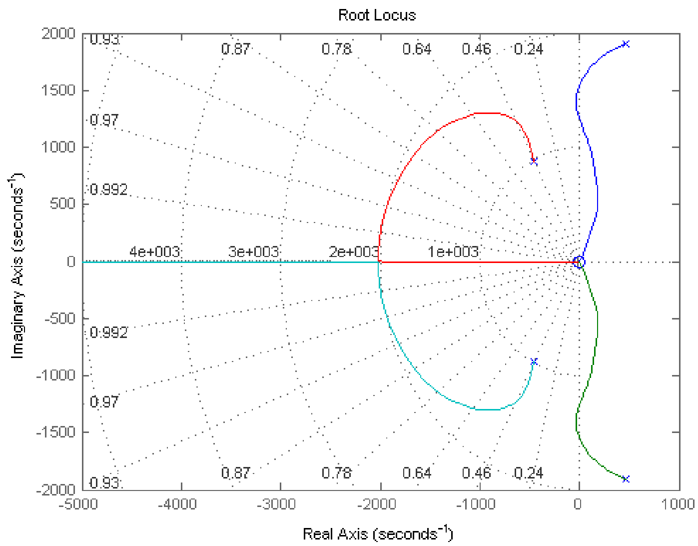

Figure 3.3: Root locus plot of the 4$^{\text{th}}$ order differential expression derived by deWaele [10] and confirmed in Appendix A.

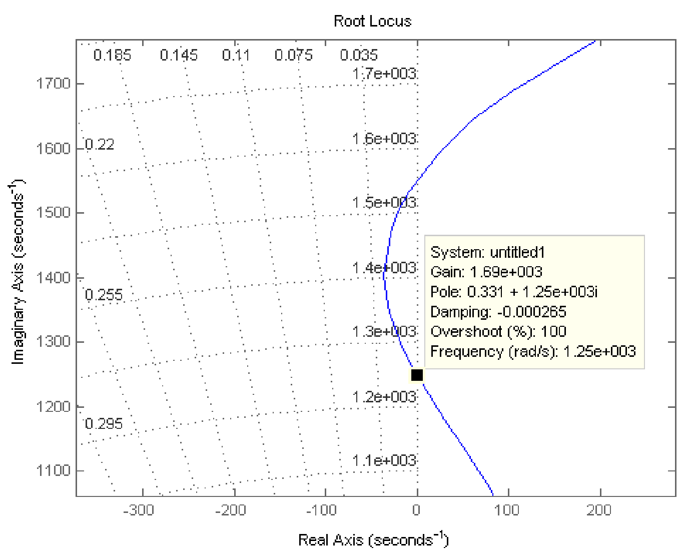

Figure 3.4: Close up of root locus plot of Eq. (3.3), showing gain of 1.69×10^3

Fig. 3.4 displays a close up of the the root locus plot and a marker displaying the gain for where the system becomes unstable. By using Eq. (3.1), the critical temperature ratio can be determined. From the critical temperature ratio, given the ambient temperature the regenerator hot-end temperature can be determined. DeWaele then attempted to determine the transient temperature and pressure responses vs. time as the system transitions from a static system to an oscillatory one. From conservation of energy the expression for temperature in there regenerator can be described by:

$$C_H \frac{dT_t}{dt} = \dot{Q}_t - \dot{Q}_c - \overset{*}{H}_t \tag{3.4}$$

In Eq. (3.4), the term C_H refers to the heat capacity of the regenerator, T_t refers to the hot end of the regenerator, $\dot{Q}_t$ and $\dot{Q}_c$ refer respectively to heat entering and leaving the system. Finally, the term $\overset{*}{H}$ is the enthalpy flow rate in the system defined as:

$$\overset{*}{H}_t = \overset{*}{V}_h \delta p_t \tag{3.5}$$

And also:

$$\dot{Q}_c = \kappa_a \frac{A_r}{L_r}(T_t - T_a) \tag{3.6}$$

The expression for $\overset{*}{V}_h$ can be shown from Appendix A:

$$\frac{d\overset{*}{V}_h}{dt} + \frac{\overset{*}{V}_h a_i T_a}{T_t C_r} = \left(\frac{1}{w_t} + \frac{1}{w_d} + \frac{1}{w_R}\right)\frac{d^2\delta p_t}{dt^2} + C_0\frac{d\delta p_t}{dt} + a_R \delta p_t \tag{3.7}$$

It can be seen from Eq. (3.1), Eq. (3.4) and Eq. (3.7), that for 3 unknowns:

δp_t, $\overset{*}{V}_h$, and T_t, there are 3 distinct differential equations. By using a MATLAB's ODE45 (Dormand-Prince) solution method, a numerical solution for T_t and p_1 (the amplitude of δp_t) can be generated. Fig. 3.5 depicts the transient response of the thermoacoustic engine where the regenerator has a presumed heat capacitance $C_H = 0.21$ as a heat in put of $\dot{Q}_t = 500W$ is applied as published by deWaele. Fig. 3.6 is the verification performed in this paper using Eq. (3.1), Eq. (3.4) and Eq. (3.7). The MATLAB code and Simulink block diagram shown in Appendix C.2.

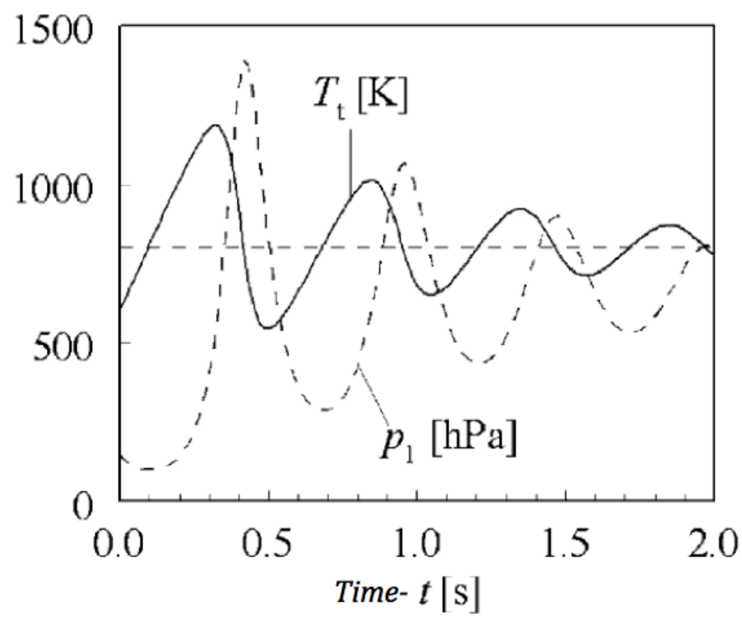

Figure 3.5: Figure 7 from deWaele's paper displaying the theoretical transient response of the traveling wave thermos acoustic engine [10].

Similar to Fig. 3.5 and Fig. 3.6, Fig. 3.7 depicts the transient response of the thermoacoustic engine where the regenerator has a presumed heat capacitance $C_H = 21$ as a heat in put of $\dot{Q}_t = 2000W$ is applied as published by deWaele. Fig. 3.8 is the verification performed in this paper using Eq. (3.1), Eq. (3.4) and Eq. (3.7). In his publication, deWaele refers to Fig. 3.7 as a "more realistic" transient

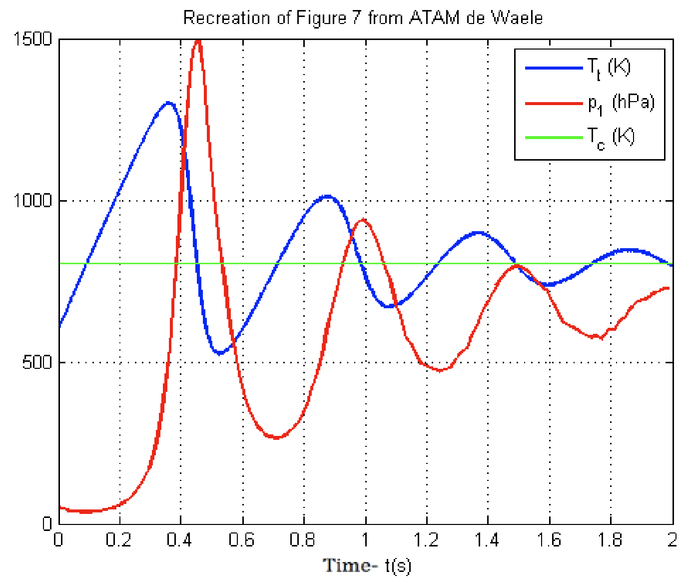

Figure 3.6: Recreated verification of Figure 7 from deWaele's paper

response.

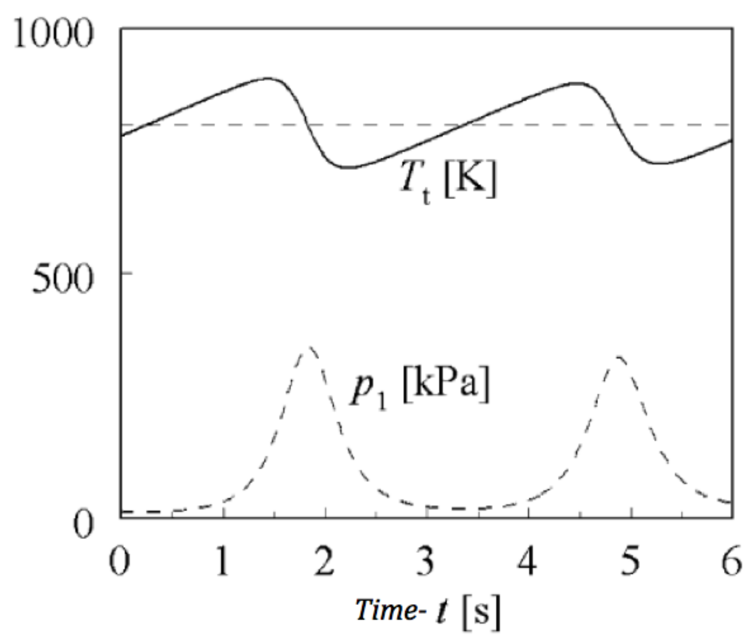

Figure 3.7: Figure 8 from deWaele's paper displaying the "more realistic" theoretical transient response of the traveling wave thermos acoustic engine [10].

Meanwhile, similar transient plots are generated for a prototype of the TWTAE,

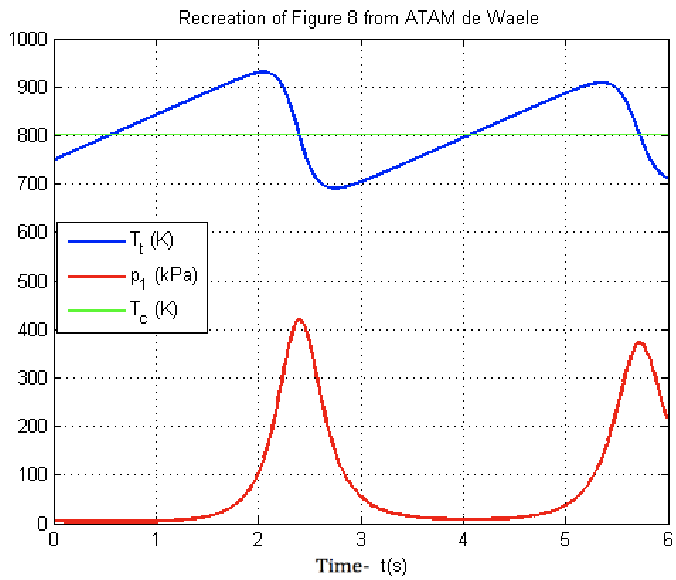

Figure 3.8: Verification of Figure 8 from deWaele's paper.

which is described in Chapter 7. Plots of numerical solutions for T_t and p_1, (the amplitude of δp_t) are shown in Fig. 3.9 and Fig. 3.10.

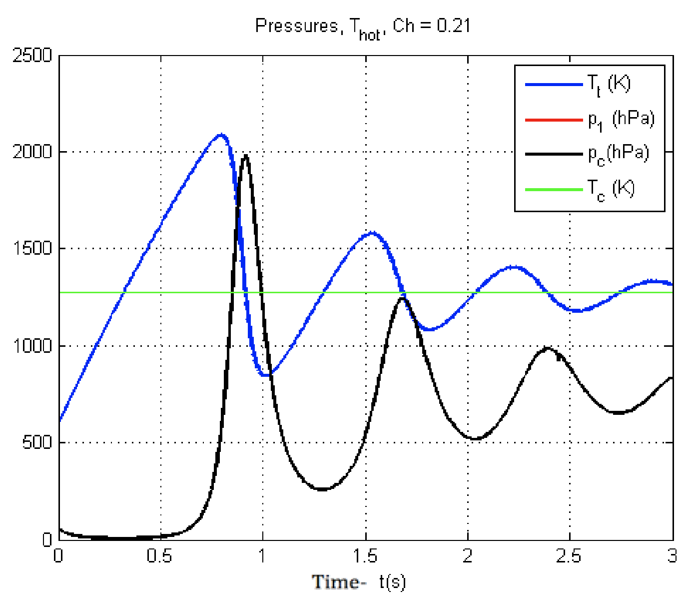

Figure 3.9: Plot of T_t and p_1 vs. time fora prototype of the traveling wave thermoacoustic engine as described in chapter 7. $C_H = 0.21$ and $\dot{Q}_t = 500W$.

In Fig. 3.9, an important characteristic is the oscillation of both the temperature and pressure for this system. The explanation for this oscillation is that, as the temperature increases in the hot-end of the regenerator, when the critical temperature is reached, the system becomes unstable and pressure oscillations begin. Then as enthalpy carries heat out of the system due to volume flow, the system loses temperature and the oscillations reduce, which in turn causes the temperature to rise again. Ultimately the system will settle into a steady state where the temperature is settling around a constant temperature and the pressure oscillatory amplitude also settles. According to deWaele, a "more accurate" model of the system can be approximated with $C_H = 21$. For a higher thermal capacitance, the system reacts more slowly to temperature change. This is shown in Fig. 3.10.

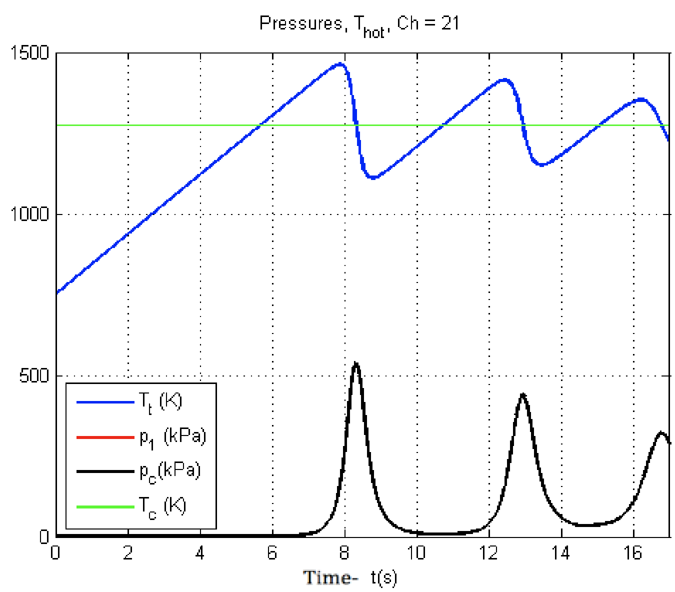

Figure 3.10: Plot of T_t and p_1 vs. time for a prototype of the traveling wave thermoacoustic engine as described in chapter 7. $C_H = 21$ and $\dot{Q}_t = 2000W$.

The important aspects of these two plots in Fig. 3.9 and Fig. 3.10 is the rising and falling action of the plots. According to this theory, there exists a "threshold" power input which would cause the oscillations to start, then die off due to enthalpy as heat leaves the system, and then start again as the temperature rises due to the power input. Chapter 8 shows the temperature and pressure plots that are derived from the experimental setup described in Chapter 7 which attempt to confirm this theory. The volume flow rate for both situations, $C_H = 0.21$ and $C_H = 21$ are shown in Fig. 3.11 and Fig. 3.12 respectively. These are compared with Chapter 6, which shows results from from DeltaEC simulations.

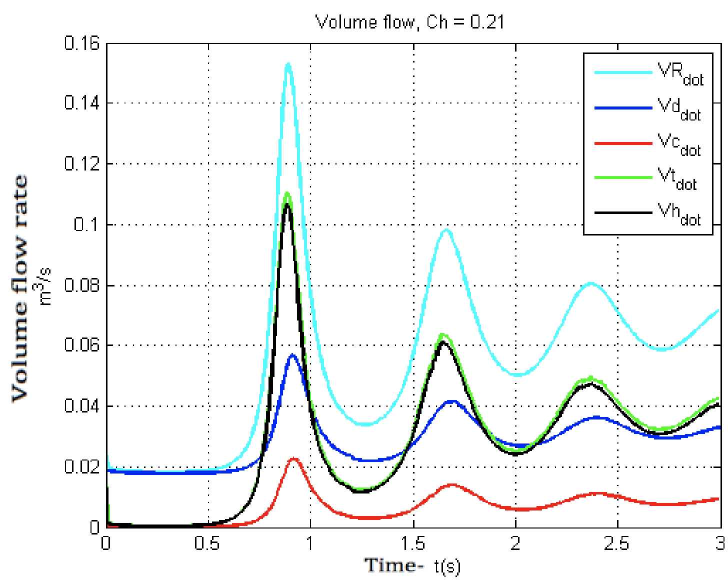

Figure 3.11: Plot of volume flow rate vs. time for a prototype of the traveling wave thermoacoustic engine as described in Chapter 7. $C_H = 0.21$ and $\dot{Q}_t = 500W$.

According to the DeltaEC analysis from Chapter 6, it can be seen that the volume flow through the regenerator was calculated to have a linear relationship with input power. From Fig. 6.3 it was approximated that the flow rate has values between 3.65×10^{-3} and 4×10^{-3} $^{m^3}/_{s}$ corresponding to input powers between 300W

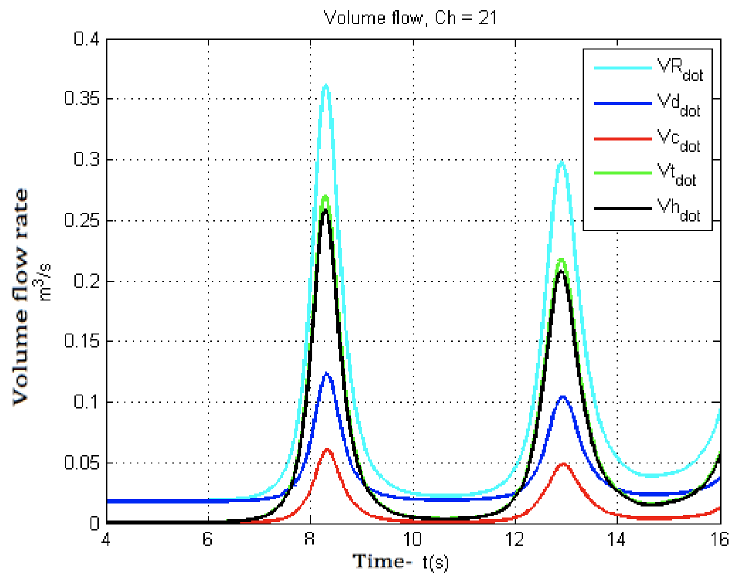

Figure 3.12: Plot of volume flow rate vs. time for a prototype of the traveling wave thermoacoustic engine as described in Chapter 7. $C_H = 21$ and $\dot{Q}_t = 2000W$.

and 360W. From Fig. 3.11, the lumped capacity model approximates that the volume flow rate settles somewhere between 0.01 and 0.07 m^3/s, depending on where the measurement is taking place, with the volume flow rate of the pulse tube settling at about 0.04 m^3/s, or about 10 times the volume flow rate estimated from DeltaEC.

By using an input heat power of 354.7W, the same as the maximum input power used in the experiments in Chapter 8, a thermal capacitance of $C_H = 0.021$ yields an oscillating pressure amplitude plotted in Fig. 3.13 , and a volume flow rate in Fig. 3.14. As can be seen from these figures, the steady state pressure amplitude is predicted to be 628.9 hPa, which is equivalent to 9.12 psi. The volume flow rate predicted to be between 0.008 m^3/s and 0.057 m^3/s depending on which point in the TWTAE is being measured. Changing C_H in the model does not have an impact steady-state pressure amplitude predictions, but does have an impact on the time it takes for the system to reach steady-state.

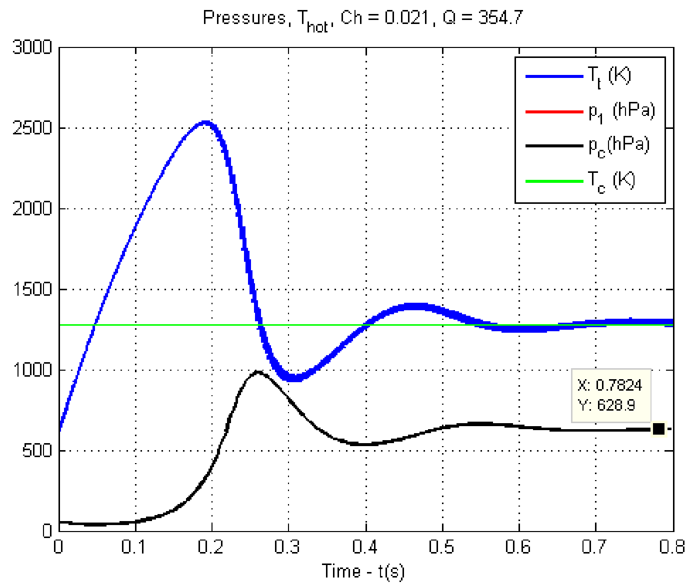

Figure 3.13: Plot of pressure amplitude vs. time for a prototype of the traveling wave thermoacoustic engine as described in Chapter 7. $C_H = 0.021$ and $\dot{Q}_t = 354.7W$.

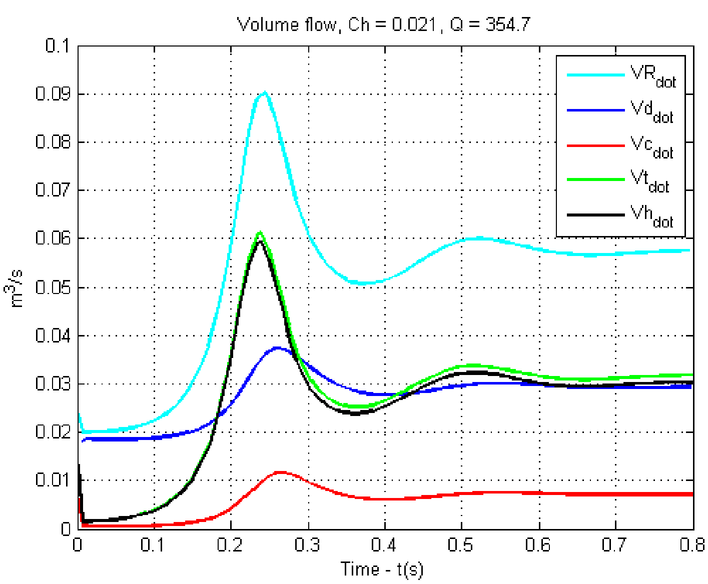

Figure 3.14: Plot of volume flow rate vs. time for a prototype of the traveling wave thermoacoustic engine as described in Chapter 7. $C_H = 0.021$ and $\dot{Q}_t = 354.7W$.

3.2 Summary

This chapter has presented the basics of a lumped-parameter model of a traveling wave thermoacoustic engine. The model is based on deWaele's analysis. The predictions of the threshold of onset of self-sustained oscillations and transient performance characteristics are presented. Application of the model to the analysis of the TWTAE is also presented.

Chapter 4

Electric Analog of the TWTAE

4.1 Electric Analog of the TWTAE with Piezoelectric Disc Attached to Resonator End Cap

Analogies exist between acoustic modeling and electric circuit modeling [19]. This is done because acoustic equations regarding pressure and volume flow bear the same format as electric equations regarding voltage and current flow. Tab. 4.1 represents the acoustic terms and the analogous electric equivalents. Expressions for determining analogous capacitance and inductance are given later in the chapter in Eq. (4.1) and Eq. (4.4).

Acoustic networks	AC electric networks
pressure p_1	voltage V_1
volume flow rate U_1	current I_1
compliance C	capacitance C
inertance L	inductance L
flow resistance R	resistance R
acoustic power $\dot{E}_2$	electric power $\dot{W}_2$

Table 4.1: Analogous acoustic and electric components for system modeling [19].

The traveling wave engine diagram described by A.T.A.M. de Waele is shown in Fig. 3.1 with the pulse tube, compliance, connecting tube, and resonator labeled respectively as sections t, c, d, and R. A.T.A.M. de Waele then uses a lumped-parameter model to discretize the system as shown in Fig. 3.2. In this model, the pulse tube, compliance, and connecting tube are transformed into lumped-parameter volumes. The inertance is transformed into a piston, while the resonator is modeled as both an inertance and a piston. Each section can be modeled as an inertance, compliance, and a resistance, but for simplification purposes, the resistance is neglected. Also the compliance portions of the inertance is neglected as is the inertial aspect of the compliance section and connector section. The resonator is modeled as both a compliance and inertance.

The system can also be modeled as an electrical analog seen in Fig. 4.1. Included in this model is a piezo diaphragm sealing the resonator tube.

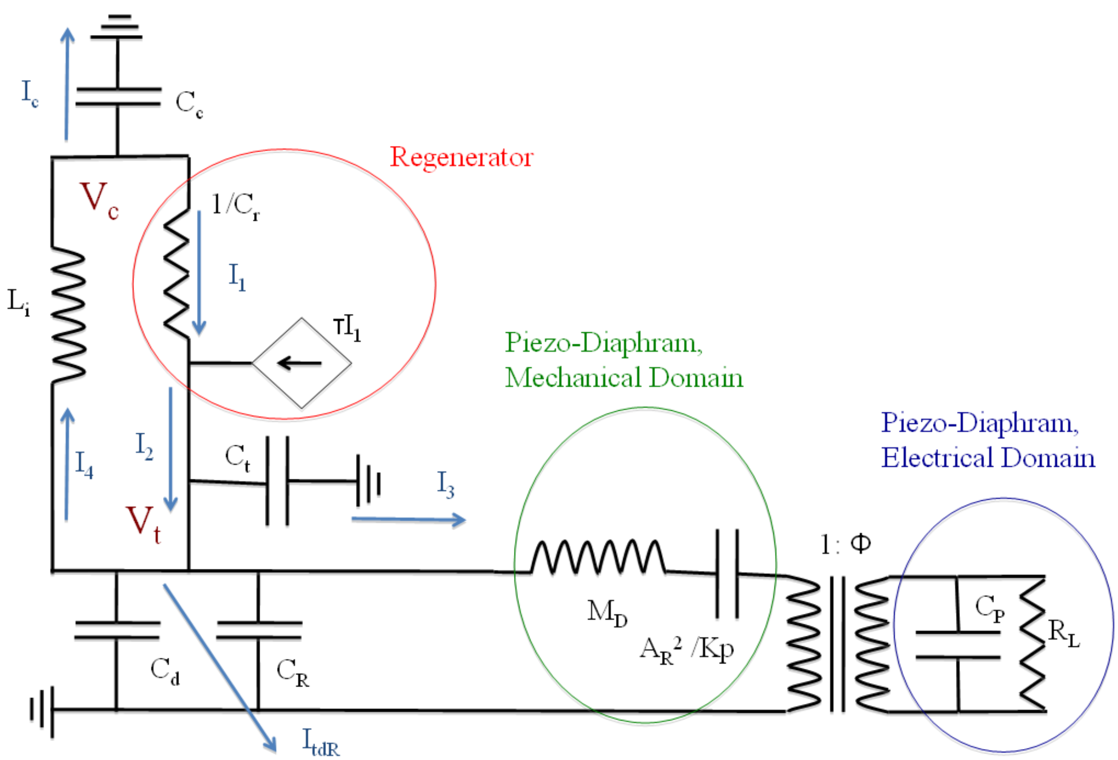

Figure 4.1: Electric analog lumped-parameter model of traveling wave thermoacoustic engine.

In Fig. 4.1, the term C represents equivalent capacitance of an acoustic chamber. For sections $i = t, R, d, c$, the equivalent capacitance is defined as:

$$C_i = \frac{V_i}{\rho_0 c_0^2} \tag{4.1}$$

In Eq. (4.1), V is the volume of the section, ρ is the density of the air in the section, and c is the speed of sound. And because:

$$c^2 = \frac{\gamma p}{\rho} \tag{4.2}$$

Eq. (4.1) can be rewritten as:

$$C_i = \frac{V_i}{\gamma p} \tag{4.3}$$

where in Eq. (4.2) and Eq. (4.3), γ is the specific heat ratio and p is the pressure.

As for the term labelled L_i in Fig. 4.1, the equivalent impedance in an acoustic tube is given as:

$$L_i = \frac{\rho_0 l_i}{A_i} \tag{4.4}$$

where in Eq. (4.4), l_i is the length of the section modeled as an inductor and A_i is the cross sectional area of the section. Also the flow conductance, labelled C_r in Fig. 4.1 is defined as:

$$C_r = \frac{1}{\eta_a Z_r} \tag{4.5}$$

The equivalent resistance of the regenerator section is defined as ${}^{1}/_{C_r}$. In Eq. (4.5), η_a is the viscocity of air at room temperature. Also, Z_r is defined as:

$$Z_r = \frac{z_r l_r}{A_r} \tag{4.6}$$

In Eq. (4.6), z_r is the specific flow resistance or the regenerator, l_r is the length of the regenerator and A_r is the cross sectional area of the regenerator. The capacitance of the piezo-diaphragm at the end of the resonator C_p is calculated as:

$$C_p = \frac{\varepsilon A_R}{t_p}\left(1 - k^2\right) \tag{4.7}$$

where k is given as:

$$k = \frac{dc^E}{\varepsilon} \tag{4.8}$$

where ε is the permittivity, t is the thickness of the piezo-diaphragm, c^E is the elastic modulus, d is the piezo strain constant, and A_R is the area of the diaphragm. Also from Fig. 4.1:

$$K_p = \frac{c^E A_R}{t_p} \tag{4.9}$$

Also the equivalent inductance due to the mass of the piezo-diaphragm, M_D is given as:

$$M_D = \frac{m_p}{A_R^2} \tag{4.10}$$

In this expression, m_p is defined as the mass of the piezo-diaphragm. The resonant frequency of the system is given as:

$$
\begin{aligned}
\omega_n^2 &= \frac{c^E A_R}{t_p m_p} \\
&= \frac{K_p}{m_p} \\
&= \frac{K_p}{A_R^2 M_D}
\end{aligned} \tag{4.11}
$$

The turning ratio, ϕ, is given as:

$$
\phi = -\frac{dK_p}{A_R} \tag{4.12}
$$

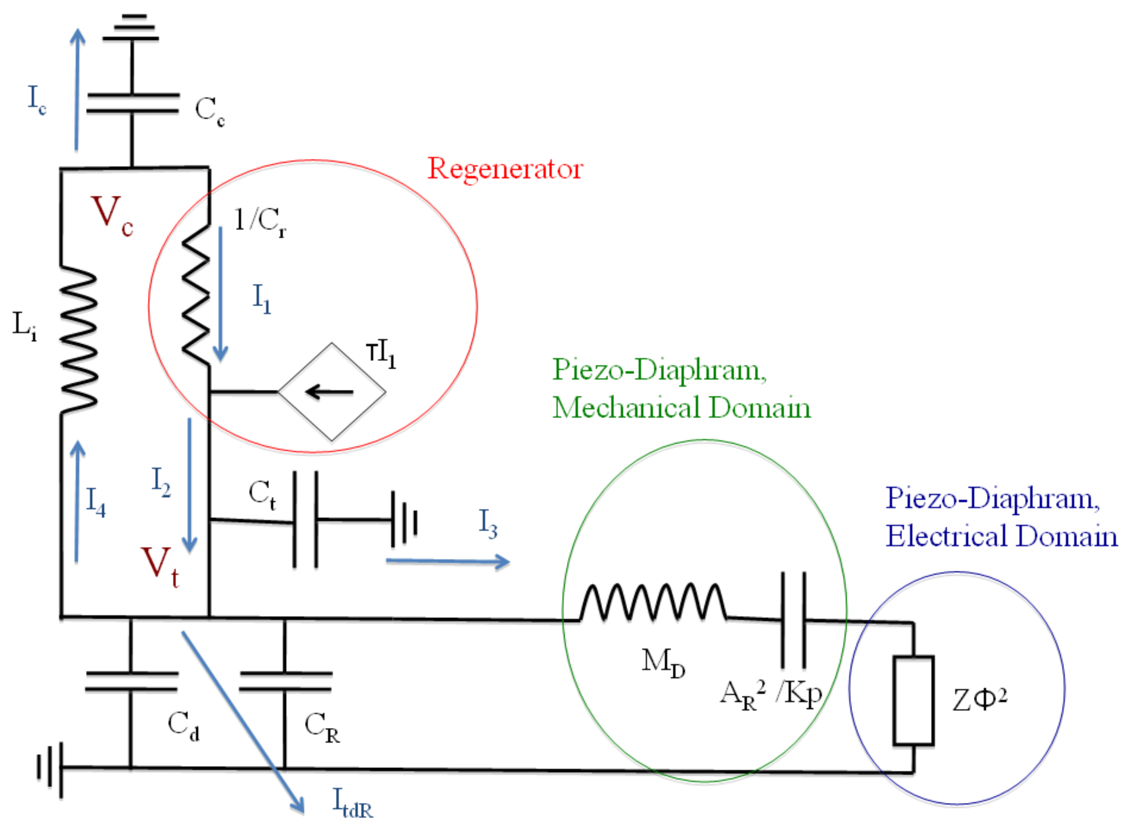

Figure 4.2: Electric analog lumped-parameter model of traveling wave thermoacoustic engine, simplified piezo model.

Further simplification of the circuit analog diagram can be performed, as seen in Fig. 4.2. In this figure, Z is the equivalent impedance of the load resistor R_L in parallel with the piezo capacitance C_p. This, in the Laplace domain is given as:

$$Z = -\frac{R_L}{1 + R_L C_p s} \tag{4.13}$$

The circuit analysis of Fig. 4.2 is performed in Appendix B. This appendix leads to the following expression for V_t:

$$0 = V_t \left(s^5 + a_4 s^4 + a_3 s^3 + a_2 s^2 + a_1 s + a_0 \right) \tag{4.14}$$

where the coefficients a_0 through a_4, as given in Eq. (B.20), are:

$$\begin{aligned}
a_4 &= \frac{1}{R_L C_p}(1 + \tau C_r w_e R_L C_p + w_c C_R R_L C_p) \\
a_3 &= \frac{1}{R_L C_p}\begin{pmatrix} \tau C_r w_e + R_L C_p(a_i w_e + a_i w_c + a_R w_e) \\ +w_c C_r + \omega_n^2 R_L (C_p + d^2 K_p) \end{pmatrix} \\
a_2 &= \frac{1}{R_L C_p}\begin{pmatrix} \omega_n^2 + (a_i w_e + a_R w_e + w_c a_i) + \tau C_r w_e \omega_n^2 R_L (C_p + d^2 K_p) \\ +C_r w_c \omega_n^2 R_L (C_p + d^2 K_p) + a_R w_c w_e C_r R_L C_p \end{pmatrix} \\
a_1 &= \frac{1}{R_L C_p}\begin{pmatrix} C_r w_c \omega_n^2 + a_i (w_e + w_c) \omega_n^2 R_L (C_p + d^2 K_p) + a_R w_e w_c C_r \\ +a_R a_i w_e w_c R_L C_p + \tau w_e C_r \omega_n^2 \end{pmatrix} \\
a_0 &= \frac{1}{R_L C_p}\left(a_i (w_e + w_c) \omega_n^2 + a_R a_i w_c w_e \right)
\end{aligned} \tag{4.15}$$

4.2 Electric Analog of the TWTAE without Piezoelectric Disc

The system can also be modeled for when the piezo-diaphragm is not present and is replaced with a rigid end, or in other words, when $R_L = C_p = Z = Kp = 0$.

The diagram for such a situation is seen in Fig. 4.3.

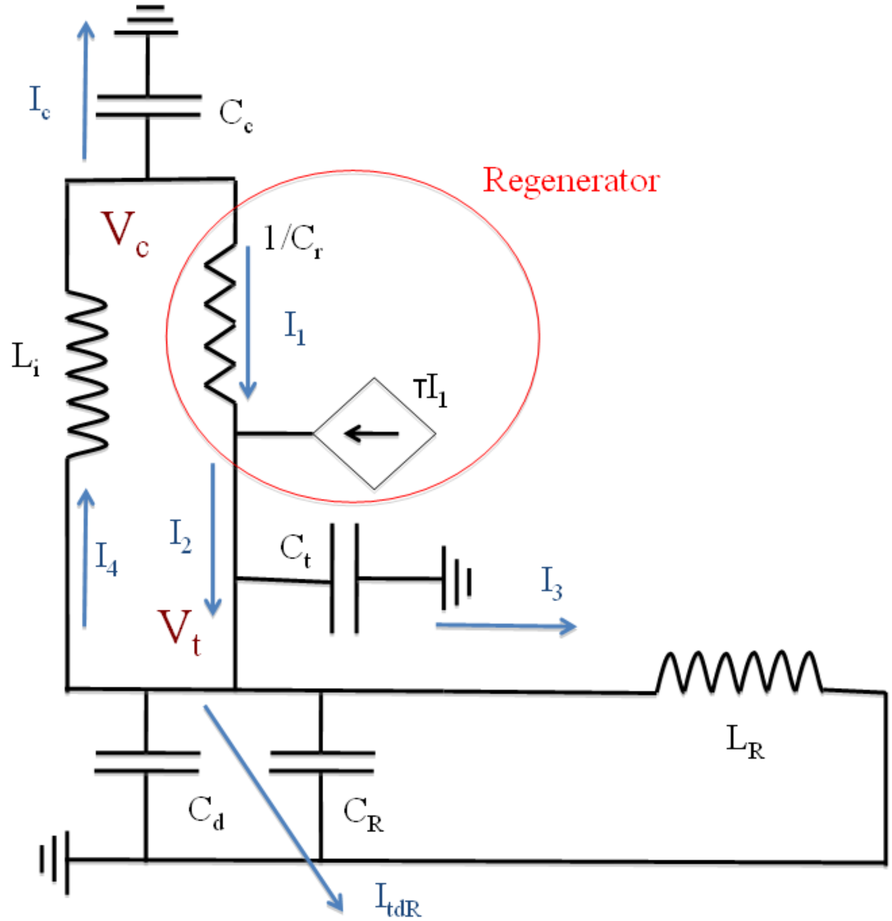

Figure 4.3: Electric analog lumped-parameter model of traveling wave thermoacoustic engine without piezo diaphragm end cap.

Continuing the derivation, as outlined in detail in Appendix B, for the situation described in Fig. 4.3, it can be seen that the expression for V_t becomes:

$$0 = V_t \left(s^4 + a_3 s^3 + a_2 s^2 + a_1 s + a_0\right) \tag{4.16}$$

where the coefficients a_0 through a_3 in Eq. (B.23) are:

$$
\begin{aligned}
a_3 &= \tau C_r w_e + w_c C_r \\
a_2 &= a_i w_e + a_i w_c + a_R w_e \\
a_1 &= a_R w_c w_e C_r \\
a_0 &= a_R a_i w_c w_e
\end{aligned}
\tag{4.17}
$$

Therefore:

$$
0 = V_t \begin{pmatrix} s^4 \\ + \left(\tau C_r w_e + w_c C_r\right) s^3 \\ + \left(a_i w_e + a_i w_c + a_R w_e\right) s^2 \\ + \left(a_R w_c w_e C_r\right) s \\ a_R a_i w_c w_e \end{pmatrix}
\tag{4.18}
$$

Eq. (4.18) is precisely the same as that derived by deWaele [10]. The primary difference between the expressions is that for the model where a piezo disc is present, the end cap is considered a dynamic system capable of deformation, while for the model without the piezo disc, the end cap is considered static. The term L_R represents the inductance due to the air piston in the piezo-free case, while M_D is the inductance due to a dynamic end cap mass in the case where the piezo is present. Both terms do not exist simultaneously in either model.

4.3 Summary

This chapter has presented an electrical analog of the TWTAE which is coupled with a piezoelectric disc to harvest the acoustic energy. The developed analog can be used to, in general, predict the performance of the TWTAE but in particular, determine the threshold of onset of self-sustained oscillations.

Chapter 5
Axisymmetric Finite Element Model of a Composite Piezoelectric Disc

5.1 Finite Element Formulation

This chapter attempts to perform a finite element analysis of a composite piezoelectric disc consisting of an aluminum disc of diameter of $2.16in$, and a thickness of $0.015in$ with a Lead-Zirconate-Titanate piezo-disc $1.25in$ in diameter and $0.0075in$ thick bonded to it. The schematic for this can be seen in Fig. 5.1.

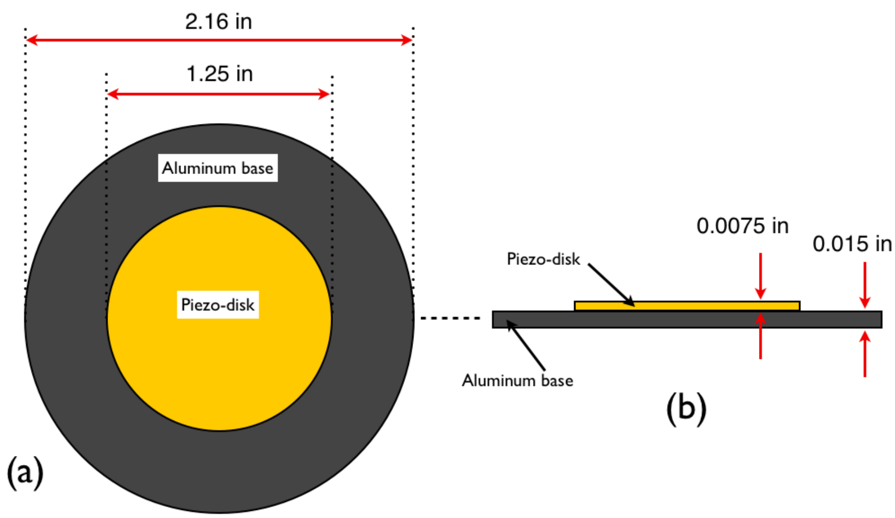

Figure 5.1: Schematic drawing of a composite piezo disc: (a) top view (b) profile view.

The composite piezo system will be analyzed using concentric, axially symmetric elements of uniform thickness. The process will be following the method outlined by K.C. Rocky *et al.* [11]. A generic axially symmetric element can be seen in Fig. 5.2

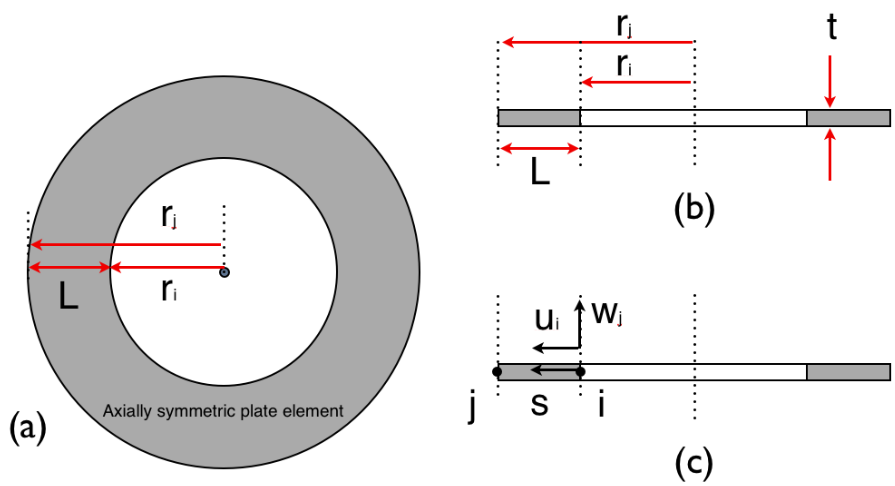

Figure 5.2: Circular plate element: (a) top view of element of width L showing two radii of lengths r_i and r_j (b) profile cross section of element of width L showing radii of lengths r_i and r_j and disc thickness t (c) profile cross section of element showing location of node i and node j for the element and radial displacement u_1 and in plane displacement w_1.

In Fig. 5.2, the coordinate s, is the only degree of for a axially symmetric system. The shape functions for the in-plane displacement u and the normal displacement w is given as follows:

$$\begin{aligned} u &= \alpha_1 + \alpha_2 s \\ w &= \alpha_3 + \alpha_4 s + \alpha_5 s^2 + \alpha_6 s^3 \\ \frac{dw}{ds} &= \alpha_4 + 2\alpha_5 s + 3\alpha_6 s^2 \end{aligned} \tag{5.1}$$

The α's for each equation are coefficients for the shape functions, unique to each element. At node 1 of each element, $s = 0$, and the expressions become:

$$u_i = \alpha_1$$

$$
\begin{aligned}
w_i &= \alpha_3 \\
\left(\frac{dw}{ds}\right)_i &= \alpha_4
\end{aligned}
\tag{5.2}
$$

At node 2 for each element, $s = L$, therefore the expressions become:

$$
\begin{aligned}
u_j &= \alpha_1 + \alpha_2 L \\
w_j &= \alpha_3 + \alpha_4 L + \alpha_5 L^2 + \alpha_6 L^3 \\
\left(\frac{dw}{ds}\right)_j &= \alpha_4 + 2\alpha_5 L + 3\alpha_6 L^2
\end{aligned}
\tag{5.3}
$$

Therefore, Eq. (5.2) and Eq. (5.3) in matrix form can be expressed as:

$$
\begin{Bmatrix} u_i \\ w_i \\ \left(\frac{dw}{ds}\right)_i \\ u_j \\ w_j \\ \left(\frac{dw}{ds}\right)_j \end{Bmatrix}
=
\begin{bmatrix}
1 & 0 & 0 & 0 & 0 & 0 \\
0 & 0 & 1 & 0 & 0 & 0 \\
0 & 0 & 0 & 1 & 0 & 0 \\
1 & L & 0 & 0 & 0 & 0 \\
0 & 0 & 1 & L & L^2 & L^3 \\
0 & 0 & 0 & 1 & 2L & 3L^2
\end{bmatrix}
\begin{Bmatrix} \alpha_1 \\ \alpha_2 \\ \alpha_3 \\ \alpha_4 \\ \alpha_5 \\ \alpha_6 \end{Bmatrix}
\tag{5.4}
$$

Rearranging Eq. (5.40 to solve for the column vectors of shape function coefficients:

$$
\begin{Bmatrix} \alpha_1 \\ \alpha_2 \\ \alpha_3 \\ \alpha_4 \\ \alpha_5 \\ \alpha_6 \end{Bmatrix} = \begin{bmatrix} 1 & 0 & 0 & 0 & 0 & 0 \\ 0 & 0 & 1 & 0 & 0 & 0 \\ 0 & 0 & 0 & 1 & 0 & 0 \\ 1 & L & 0 & 0 & 0 & 0 \\ 0 & 0 & 1 & L & L^2 & L^3 \\ 0 & 0 & 0 & 1 & 2L & 3L^2 \end{bmatrix}^{-1} \begin{Bmatrix} u_i \\ w_i \\ \left(\frac{dw}{ds}\right)_i \\ u_j \\ w_j \\ \left(\frac{dw}{ds}\right)_j \end{Bmatrix} \tag{5.5}
$$

The inverse of the 6×6 matrix above in Eq. (5.5) is:

$$
\begin{bmatrix} 1 & 0 & 0 & 0 & 0 & 0 \\ 0 & 0 & 1 & 0 & 0 & 0 \\ 0 & 0 & 0 & 1 & 0 & 0 \\ 1 & L & 0 & 0 & 0 & 0 \\ 0 & 0 & 1 & L & L^2 & L^3 \\ 0 & 0 & 0 & 1 & 2L & 3L^2 \end{bmatrix}^{-1} = \begin{bmatrix} 1 & 0 & 0 & 0 & 0 & 0 \\ -\frac{1}{L} & 0 & 0 & \frac{1}{L} & 0 & 0 \\ 0 & 1 & 0 & 0 & 0 & 0 \\ 0 & 0 & 1 & 0 & 0 & 0 \\ 0 & -\frac{3}{L^2} & -\frac{2}{L} & 0 & \frac{3}{L^2} & -\frac{1}{L} \\ 0 & \frac{2}{L^3} & \frac{1}{L^2} & 0 & -\frac{2}{L^3} & \frac{1}{L^2} \end{bmatrix} \tag{5.6}
$$

Defining the displacements u and w at any point in the element, using the shape functions from Eq. (5.1):

$$\begin{Bmatrix} u \\ w \end{Bmatrix} = \begin{bmatrix} 1 & s & 0 & 0 & 0 & 0 \\ 0 & 0 & 1 & s & s^2 & s^3 \end{bmatrix} \begin{Bmatrix} \alpha_1 \\ \alpha_2 \\ \alpha_3 \\ \alpha_4 \\ \alpha_5 \\ \alpha_6 \end{Bmatrix} \tag{5.7}$$

Therefore, replacing the column vector of α coefficients in Eq. (5.7) with the expression from Eq. (5.5) in conjunction with Eq. (5.6):

$$\begin{Bmatrix} u \\ w \end{Bmatrix} = \begin{bmatrix} 1 & s & 0 & 0 & 0 & 0 \\ 0 & 0 & 1 & s & s^2 & s^3 \end{bmatrix} \begin{bmatrix} 1 & 0 & 0 & 0 & 0 & 0 \\ -\frac{1}{L} & 0 & 0 & \frac{1}{L} & 0 & 0 \\ 0 & 1 & 0 & 0 & 0 & 0 \\ 0 & 0 & 1 & 0 & 0 & 0 \\ 0 & -\frac{3}{L^2} & -\frac{2}{L} & 0 & \frac{3}{L^2} & -\frac{1}{L} \\ 0 & \frac{2}{L^3} & \frac{1}{L^2} & 0 & -\frac{2}{L^3} & \frac{1}{L^2} \end{bmatrix} \begin{Bmatrix} u_i \\ w_i \\ \left(\frac{dw}{ds}\right)_i \\ u_j \\ w_j \\ \left(\frac{dw}{ds}\right)_j \end{Bmatrix} \tag{5.8}$$

Let:

$$[N_s] = \begin{bmatrix} 1 & s & 0 & 0 & 0 & 0 \\ 0 & 0 & 1 & s & s^2 & s^3 \end{bmatrix} \begin{bmatrix} 1 & 0 & 0 & 0 & 0 & 0 \\ -\frac{1}{L} & 0 & 0 & \frac{1}{L} & 0 & 0 \\ 0 & 1 & 0 & 0 & 0 & 0 \\ 0 & 0 & 1 & 0 & 0 & 0 \\ 0 & -\frac{3}{L^2} & -\frac{2}{L} & 0 & \frac{3}{L^2} & -\frac{1}{L} \\ 0 & \frac{2}{L^3} & \frac{1}{L^2} & 0 & -\frac{2}{L^3} & \frac{1}{L^2} \end{bmatrix} \tag{5.9}$$

Also, let the elemental nodal deflection vector for each element be defined as:

$$\{\delta_e\} = \left\{ \begin{array}{cccccc} u_i & w_i & \left(\frac{dw}{ds}\right)_i & u_j & w_j & \left(\frac{dw}{ds}\right)_j \end{array} \right\}^T \tag{5.10}$$

Therefore, Eq. (5.8) becomes:

$$\left\{ \begin{array}{c} u \\ w \end{array} \right\} = [N_s]\{\delta_e\} \tag{5.11}$$

5.2 Mass Matrix Formulation

The kinetic energy, KE_e for each element in the disc system can be determined from the equation:

$$KE_e = \frac{1}{2} \int_V \rho \left\{ \begin{array}{cc} \dot{u} & \dot{w} \end{array} \right\} \left\{ \begin{array}{c} \dot{u} \\ \dot{w} \end{array} \right\} dV \tag{5.12}$$

where in Eq. (5.12), ρ is the density of the material of the element, and:

$$\left\{ \begin{array}{cc} \dot{u} & \dot{w} \end{array} \right\} = \{\dot{\delta}_e\}^T [N_s]^T \tag{5.13}$$

and:

$$\left\{ \begin{array}{c} \dot{u} \\ \\ \dot{w} \end{array} \right\} = [N_s]\{\dot{\delta}_e\} \tag{5.14}$$

Therefore, Eq. (5.12) becomes:

$$KE_e = \frac{1}{2} \int\limits_V \rho \{\dot{\delta}_e\}^T [N_s]^T [N_s] \{\dot{\delta}_e\} dV \tag{5.15}$$

Since $\{\dot{\delta}_e\}$ and $\{\dot{\delta}_e\}^T$ are not dependent on s, both terms can be moved outside of the integral:

$$KE_e = \frac{1}{2} \{\dot{\delta}_e\}^T \int\limits_V \rho [N_s]^T [N_s] dV \{\dot{\delta}_e\} \tag{5.16}$$

Because the element is a disc shaped as seen in Fig. 5.2, the integral expression in Eq. (5.16) becomes:

$$KE_e = \frac{1}{2}\{\dot{\delta}_e\}^T \int_{r_i}^{r_j} \rho[N_s]^T[N_s]2\pi rtdr\{\dot{\delta}_e\} \tag{5.17}$$

The radius from the center axis, r, for the element in terms of s can be defined using the following:

$$r = r_i + s \tag{5.18}$$

Meaning:

$$dr = ds \tag{5.19}$$

By using Eq. (5.18) and Eq. (5.19), Eq. (5.17) becomes:

$$KE_e = \frac{1}{2}\{\dot{\delta}_e\}^T \left[\int_0^L \rho[N_s]^T[N_s]2\pi(r_i + s)tds\right]\{\dot{\delta}_e\} \tag{5.20}$$

The expression for kinetic energy for each element can be written as:

$$KE_e = \frac{1}{2}\{\dot{\delta}_e\}^T [M_e] \{\dot{\delta}_e\} \tag{5.21}$$

where in Eq. (5.21), $[M_e]$ refers to the element mass matrix. Therefore, from Eq. (5.21):

$$[M_e] = \int_0^L \rho [N_s]^T [N_s] 2\pi (r_i + s) t ds \tag{5.22}$$

Since the inner radius, r_i, is going to be different for each element in the system, the mass matrix for each element must be calculated individually.

5.3 Stiffness Matrix Formulation

Beginning with the expression for potential energy in each element, PE_e:

$$PE_e = \frac{1}{2} \int_V ST dV \tag{5.23}$$

In Eq. (5.23), S refers to the middle surface strain in the element, and T is the middle surface stress. K.C. Rocky *et al.* [11] identifies $\{S(r,s)\}$ for a disc element ($\phi = 90°$) as follows:

$$\{S(r,s)\} = \begin{Bmatrix} \varepsilon_s \\ \varepsilon_\theta \\ \chi_s \\ \chi_\theta \end{Bmatrix} = \begin{bmatrix} \frac{d}{ds} & 0 \\ \frac{1}{r} & 0 \\ 0 & -\frac{d^2}{ds^2} \\ 0 & -\frac{1}{r}\frac{d}{ds} \end{bmatrix} \begin{Bmatrix} u \\ w \end{Bmatrix} \tag{5.24}$$

In Eq. (5.24), ε_s, is the in plane strain, ε_θ is the hoop strain, χ_s is the in plane curvature, and χ_θ is the hoop curvature. Incorporating Eq. (5.11) and Eq. (5.18):

$$\{S(r,s)\} = \left\{ \begin{array}{c} \varepsilon_s \\ \\ \varepsilon_\theta \\ \\ \chi_s \\ \\ \chi_\theta \end{array} \right\} = \begin{bmatrix} \frac{d}{ds} & 0 \\ \\ \frac{1}{r_i+s} & 0 \\ \\ 0 & -\frac{d^2}{ds^2} \\ \\ 0 & -\frac{1}{r_i+s}\frac{d}{ds} \end{bmatrix} [N_s]\{\delta_e\} \tag{5.25}$$

For convention, define:

$$[B] = \begin{bmatrix} \frac{d}{ds} & 0 \\ \\ \frac{1}{r_i+s} & 0 \\ \\ 0 & -\frac{d^2}{ds^2} \\ \\ 0 & -\frac{1}{r_i+s}\frac{d}{ds} \end{bmatrix} [N_s] \tag{5.26}$$

Therefore, Eq. (5.25) becomes:

$$\{S(r,s)\} = \left\{ \begin{array}{c} \varepsilon_s \\ \\ \varepsilon_\theta \\ \\ \chi_s \\ \\ \chi_\theta \end{array} \right\} = [B]\{\delta_e\} \tag{5.27}$$

Similarly for T, K.C. Rocky *et al.* [11] identifies $\{T(r,s)\}$ for a disc element ($\phi = 90^\circ$) as follows:

$$\{T(r,s)\} = \left\{ \begin{array}{c} \sigma_s \\ \\ \sigma_\theta \\ \\ M_s \\ \\ M_\theta \end{array} \right\} = \frac{E}{(1-\nu^2)} \left[\begin{array}{cccc} 1 & \nu & 0 & 0 \\ \\ \nu & 1 & 0 & 0 \\ \\ 0 & 0 & \frac{t^2}{12} & \frac{\nu}{t^2} \\ \\ 0 & 0 & \frac{\nu t^2}{12} & \frac{t^2}{12} \end{array} \right] \left\{ \begin{array}{c} \varepsilon_s \\ \\ \varepsilon_\theta \\ \\ \chi_s \\ \\ \chi_\theta \end{array} \right\} \tag{5.28}$$

In Eq. (5.28), σ_s and σ_θ refers to in plane and hoop stress respectively, while M_s and M_θ refer to in plane and hoop moments. Define the following convention:

$$[D] = \frac{E}{(1-\nu^2)} \left[\begin{array}{cccc} 1 & \nu & 0 & 0 \\ \\ \nu & 1 & 0 & 0 \\ \\ 0 & 0 & \frac{t^2}{12} & \frac{\nu}{t^2} \\ \\ 0 & 0 & \frac{\nu t^2}{12} & \frac{t^2}{12} \end{array} \right] \tag{5.29}$$

Therefore with Eq. (5.27) and Eq. (5.29), Eq. (5.28) becomes:

$$\begin{aligned} \{T(r,s)\} &= [D][B]\{\delta_e\} \\ &= [D]\{S(r,s)\} \end{aligned} \tag{5.30}$$

By using the following expression:

$$ST = \{S(r,s)\}^T \{T(r,s)\} \tag{5.31}$$

Therefore Eq. (5.23) becomes:

$$PE_e = \frac{1}{2} \int_V \{S(r,s)\}^T \{T(r,s)\} dV \tag{5.32}$$

Therefore, using Eq. (5.27) and Eq. (5.30), Eq. (5.32) becomes:

$$PE_e = \frac{1}{2} \int_V \{\delta_e\}^T [B]^T [D][B] \{\delta_e\} dV \tag{5.33}$$

Since $\{\delta_e\}$ and $\{\delta_e\}^T$ are not dependent on s, both terms can be moved outside of the integral:

$$PE_e = \frac{1}{2} \{\delta_e\}^T \int_V [B]^T [D][B] dV \{\delta_e\} \tag{5.34}$$

Because the element is a disc shaped as seen in Fig. 5.2, the integral expression in Eq. (5.34) becomes:

$$PE_e = \frac{1}{2} \{\delta_e\}^T \int_{r_i}^{r_j} [B]^T [D][B] 2\pi r t dr \{\delta_e\} \tag{5.35}$$

By using Eq. (5.18) and Eq. (5.19), Eq. (5.34) becomes:

$$PE_e = \frac{1}{2} \{\delta_e\}^T \left[\int_0^L [B]^T [D][B] 2\pi (r_i + s) t ds \right] \{\delta_e\} \tag{5.36}$$

The expression for potential energy for an element can be written as:

$$PE_e = \frac{1}{2} \{\delta_e\}^T [K_e] \{\delta_e\} \tag{5.37}$$

where, in Eq. (5.35), $[K_e]$ is the element stiffness matrix. Therefore, from Eq. (5.34):

$$[K_e] = \int_0^L [B]^T [D][B] 2\pi (r_i + s) t ds \tag{5.38}$$

5.4 Formulation of Global Mass and Stiffness Matrices of Base Layer

In the previous two sections, the mass and stiffness matrices have been defined for each axisymmetric disc element. For each element, there exists a 6×1 elemental nodal deflection vector $\{\delta_e\} = \left\{ \begin{array}{cccccc} u_i & w_i & \left(\frac{dw}{ds}\right)_i & u_j & w_j & \left(\frac{dw}{ds}\right)_j \end{array} \right\}^T$. For the entire system, encompassing all nodes, define the nodal deflection vector as:

$$\{\delta\} = \left\{ \begin{array}{ccccccccccc} u_1 & w_1 & \left(\frac{dw}{ds}\right)_1 & u_2 & w_2 & \left(\frac{dw}{ds}\right)_2 & \cdots & u_N & w_N & \left(\frac{dw}{ds}\right)_N \end{array} \right\}^T \tag{5.39}$$

This nodal deflection vector corresponds to a disc with $N-1$ elements and N nodes. The vector therefore is of $3N \times 1$ dimension. The corresponding global mass and stiffness matrices are therefore of $3N \times 3N$ dimension. Formulation of each of these global matrices will now be discussed. Each of the 6×6 elemental matrices can be broken down into 3×3 quadrants. For example, the following elemental mass matrix can be broken down into four 3×3 matrices:

$$[M_i] = \left[\begin{array}{c|c} [M_{i,i}]_i & [M_{i,j}]_i \\ \hline [M_{j,i}]_i & [M_{j,j}]_i \end{array} \right] \tag{5.40}$$

Similarly for a stiffness matrix:

$$[K_i] = \left[\begin{array}{c|c} [K_{i,i}]_i & [K_{i,j}]_i \\ \hline [K_{j,i}]_i & [K_{j,j}]_i \end{array}\right] \tag{5.41}$$

For the global mass and stiffness matrices, at shared nodes between elements, element matrix quadrants are added together. This is illustrated for the global $3N \times 3N$ mass and stiffness matrices below in Eq. (5.42) and Eq. (5.43).

$$[M_b] = \left[\begin{array}{c|c|c|c|c|c} [M_{1,1}]_1 & [M_{1,2}] & 0_{3\times3} & \dots & \dots & 0_{3\times3} \\ \hline [M_{2,1}]_1 & [M_{2,2}]_1 + [M_{2,2}]_2 & [M_{2,3}]_2 & \ddots & \dots & \vdots \\ \hline 0_{3\times3} & [M_{3,2}]_2 & [M_{3,3}]_2 + \dots & \ddots & \ddots & \vdots \\ \hline \vdots & \ddots & \ddots & \ddots & \ddots & 0_{3\times3} \\ \hline \vdots & \dots & \ddots & \ddots & \dots + [M_{N-1,N-1}]_{N-1} & [M_{N-1,N}]_{N-1} \\ \hline 0_{3\times3} & \dots & \dots & 0_{3\times3} & [M_{N,N-1}]_{N-1} & [M_{N,N}]_{N-1} \end{array}\right] \tag{5.42}$$

Similarly for a stiffness matrix:

$$
[K_b] = \begin{bmatrix}
[K_{1,1}]_1 & [K_{1,2}] & 0_{3\times3} & \dots & \dots & 0_{3\times3} \\
[K_{2,1}]_1 & [K_{2,2}]_1 + [K_{2,2}]_2 & [K_{2,3}]_2 & \ddots & \dots & \vdots \\
0_{3\times3} & [K_{3,2}]_2 & [K_{3,3}]_2 + \dots & \ddots & \ddots & \vdots \\
\vdots & \ddots & \ddots & \ddots & \ddots & 0_{3\times3} \\
\vdots & \dots & \ddots & \ddots & \dots + [K_{N-1,N-1}]_{N-1} & [K_{N-1,N}]_{N-1} \\
0_{3\times3} & \dots & \dots & 0_{3\times3} & [K_{N,N-1}]_{N-1} & [K_{N,N}]_{N-1}
\end{bmatrix} \tag{5.43}
$$

This concept can be similarly applied to multilayered elements. For nodes that share both aluminum and piezo components, the global matrix matrix components adds stiffness and mass matrices for both the piezo and aluminum layers.

5.5 Stiffness Matrix for Piezo Elements

While the mass matrices for piezo elements can be calculated in the same manner as the base layer, the piezo stiffness matrices have an additional electric component that needs to be accounted for. Because of this, the piezo voltage, V, is included in the element displacement vector $\{\delta_e\}$.

$$
\{\delta_e\} = \left\{ \begin{matrix} u_i & w_i & \left(\frac{w}{ds}\right)_i & u_j & w_j & \left(\frac{w}{ds}\right)_j & V \end{matrix} \right\}^T \tag{5.44}
$$

Many of the previous equations require adjustments as a result of this change. Eq. (5.8) and Eq. (5.9) becomes:

$$
\begin{Bmatrix} u \\ w \\ V \end{Bmatrix} = \begin{bmatrix} 1 & s & 0 & 0 & 0 & 0 & 0 \\ 0 & 0 & 1 & s & s^2 & s^3 & 0 \\ 0 & 0 & 0 & 0 & 0 & 0 & 1 \end{bmatrix} \begin{bmatrix} 1 & 0 & 0 & 0 & 0 & 0 & 0 \\ -\frac{1}{L} & 0 & 0 & \frac{1}{L} & 0 & 0 & 0 \\ 0 & 1 & 0 & 0 & 0 & 0 & 0 \\ 0 & 0 & 1 & 0 & 0 & 0 & 0 \\ 0 & -\frac{3}{L^2} & -\frac{2}{L} & 0 & \frac{3}{L^2} & -\frac{1}{L} & 0 \\ 0 & \frac{2}{L^3} & \frac{1}{L^2} & 0 & -\frac{2}{L^3} & \frac{1}{L^2} & 0 \\ 0 & 0 & 0 & 0 & 0 & 0 & 1 \end{bmatrix} \{\delta_e\}
$$

$$
= [N_s]\{\delta_e\} \tag{5.45}
$$

From Eq. (5.24) and Eq. (5.25):

$$
\{S(r,s)\} = \begin{Bmatrix} \varepsilon_s \\ \varepsilon_\theta \end{Bmatrix} = \begin{bmatrix} \frac{d}{ds} & \frac{t_b}{2}\frac{d^2}{ds^2} & 0 \\ \frac{1}{r} & 0 & 0 \end{bmatrix} \begin{Bmatrix} u \\ w \\ V \end{Bmatrix}
$$

$$
= [B_2]\{\delta_e\} \tag{5.46}
$$

From Ashida and Tauchert [12], the constitutive equations for an axisymmetric piezo disc can be expressed as follows:

$$
\begin{aligned}
\sigma_s &= c_{11}\varepsilon_s + c_{12}\varepsilon_\theta + c_{13}\varepsilon_z - e_1 E_z - \beta_1 T \\
\sigma_\theta &= c_{12}\varepsilon_s + c_{11}\varepsilon_\theta + c_{13}\varepsilon_z - e_1 E_z - \beta_1 T \\
D_z &= e_1\varepsilon_s + e_1\varepsilon_\theta + e_3\varepsilon_z + \eta_3 E_z
\end{aligned} \tag{5.47}
$$

where in Eq. (5.47):

$$
\begin{aligned}
c_{11} &= \frac{c^E}{1-\upsilon_p^2} \\
c_{12} &= \frac{\upsilon_p c^E}{1-\upsilon_p^2} \\
e_1 &= c^E d_{31} \\
\eta_3 &= \varepsilon_{33}^T (1-k_{31}^2)
\end{aligned} \tag{5.48}
$$

Assuming the strain in the z direction is neglected, the constitutive equations can be expressed as:

$$
\begin{aligned}
\begin{Bmatrix} \sigma_s \\ \sigma_\theta \end{Bmatrix} &= \begin{bmatrix} c_{11} & c_{12} \\ c_{12} & c_{11} \end{bmatrix} \begin{Bmatrix} \varepsilon_s \\ \varepsilon_\theta \end{Bmatrix} - \begin{Bmatrix} e_1 \\ e_1 \end{Bmatrix} E_z \\
D_z &= \begin{Bmatrix} e_1 & e_1 \end{Bmatrix} \begin{Bmatrix} \varepsilon_s \\ \varepsilon_\theta \end{Bmatrix} + \eta_3 E_z
\end{aligned} \tag{5.49}
$$

Replacing E_z with the following expression and incorporating Eq. (5.46):

$$
\begin{aligned}
E_z &= \frac{V}{t} \\
&= \begin{Bmatrix} 0 & 0 & \frac{1}{t} \end{Bmatrix} \begin{Bmatrix} u \\ w \\ V \end{Bmatrix} \\
&= \begin{Bmatrix} 0 & 0 & \frac{1}{t} \end{Bmatrix} [N_s]\{\delta_e\}
\end{aligned} \tag{5.50}
$$

Therefore, Eq. (5.49) becomes:

$$
\begin{aligned}
\begin{Bmatrix} \sigma_s \\ \\ \sigma_\theta \end{Bmatrix} &= \begin{bmatrix} c_{11} & c_{12} \\ \\ c_{12} & c_{11} \end{bmatrix} [B_2]\{\delta_e\} - \begin{Bmatrix} e_1 \\ \\ e_1 \end{Bmatrix} \begin{Bmatrix} 0 & 0 & \frac{1}{t} \end{Bmatrix} [N_s]\{\delta_e\} \\
D_z &= \begin{Bmatrix} e_1 & e_1 \end{Bmatrix} [B_2]\{\delta_e\} + \eta_3 \begin{Bmatrix} 0 & 0 & \frac{1}{t} \end{Bmatrix} [N_s]\{\delta_e\} \qquad (5.51)
\end{aligned}
$$

Now define:

$$
\begin{aligned}
\{S_p\} &= \begin{Bmatrix} \varepsilon_s \\ \\ \varepsilon_\theta \end{Bmatrix} - \begin{bmatrix} c_{11} & c_{12} \\ \\ c_{12} & c_{11} \end{bmatrix}^{-1} \begin{Bmatrix} e_1 \\ \\ e_1 \end{Bmatrix} E_z \\
&= [B_2]\{\delta_e\} - \begin{bmatrix} c_{11} & c_{12} \\ \\ c_{12} & c_{11} \end{bmatrix}^{-1} \begin{Bmatrix} e_1 \\ \\ e_1 \end{Bmatrix} \begin{Bmatrix} 0 & 0 & \frac{1}{t} \end{Bmatrix} [N_s]\{\delta_e\} \\
&= \left[[B_2] - \begin{bmatrix} c_{11} & c_{12} \\ \\ c_{12} & c_{11} \end{bmatrix}^{-1} \begin{Bmatrix} e_1 \\ \\ e_1 \end{Bmatrix} \begin{Bmatrix} 0 & 0 & \frac{1}{t} \end{Bmatrix} [N_s] \right] \{\delta_e\} \\
&= [A]\{\delta_e\} \qquad (5.52)
\end{aligned}
$$

and:

$$
\{T_p\} = \begin{bmatrix} c_{11} & c_{12} \\ \\ c_{12} & c_{11} \end{bmatrix} [A] \{\delta_e\} \qquad (5.53)
$$

and:

$$
\begin{aligned}
E_p &= E_z = \begin{Bmatrix} 0 & 0 & \frac{1}{t} \end{Bmatrix} [N_s]\{\delta_e\} \\
&= [E]\{\delta_e\}
\end{aligned}
$$

$$\begin{aligned} D_p &= \eta_3 E_z = \eta_3 \left\{ \begin{array}{ccc} 0 & 0 & \frac{1}{t} \end{array} \right\} [N_s]\{\delta_e\} \\ &= \eta_3 [E]\{\delta_e\} \end{aligned} \tag{5.54}$$

Also, define:

$$[C] = \begin{bmatrix} c_{11} & c_{12} \\ c_{12} & c_{11} \end{bmatrix} \tag{5.55}$$

The potential energy of the system is given as:

$$PE = \frac{1}{2} \int\limits_V T_p S_p dV - \frac{1}{2} \int\limits_V D_p E_p dV \tag{5.56}$$

Incorporating Eq. (5.52), Eq. (5.53), Eq. (5.54) into Eq. (5.56):

$$PE = \frac{1}{2} \int\limits_V \{\delta_e\}^T [A]^T [C][A]\{\delta_e\} dV - \frac{1}{2} \int\limits_V \{\delta_e\}^T [E]^T \eta_3 [E]\{\delta_e\} dV \tag{5.57}$$

Rearranging Eq. (5.56) so that $\{\delta_e\}$ is outside the integral, and adjusting the integral for an axially symmetric disc element:

$$PE = \frac{1}{2}\{\delta_e\}^T \int\limits_{r_i}^{r_j} [A]^T [C][A] 2\pi r t dr \{\delta_e\} - \frac{1}{2}\{\delta_e\}^T \int\limits_{r_i}^{r_j} [E]^T \eta_3 [E] 2\pi r t dr \{\delta_e\} \tag{5.58}$$

By using Eq. (5.18) and Eq. (5.19) in Eq. (5.58):

$$\begin{aligned} PE &= \frac{1}{2}\{\delta_e\}^T \int_0^L [A]^T[C][A]2\pi(r_i+s)tds\{\delta_e\} - \frac{1}{2}\{\delta_e\}^T \int_0^L [E]^T\eta_3[E]2\pi(r_i+s)tds\{\delta_e\} \\ &= \frac{1}{2}\{\delta_e\}^T \left[\int_0^L \Big([A]^T[C][A]2\pi(r_i+s)t - [E]^T\eta_3[E]2\pi(r_i+s)t\Big)\, ds\right]\{\delta_e\} \end{aligned} \tag{5.59}$$

And from Eq. (5.37) it can be shown that the piezo element stiffness matrix can be expressed as:

$$[K_{ep}] = \int_0^L \Big([A]^T[C][A] - [E]^T\eta_3[E]\Big)\, 2\pi(r_i+s)tds \tag{5.60}$$

5.6 Global Piezo Mass and Stiffness Matrix Formulation

Formulation of the global stiffness matrix for the piezo diaphragm is similar to the process of matrix formulation in section 5.4, except that for the piezo stiffness elements described in section 5.5 the element nodal deflection vector has an added degree of freedom V at the end of the deflection vector. As before, matrix components at shared nodes are added together, but now all elements share the voltage node. Let the global deflection vector be a $(3N+1)\times(3N+1)$ vector encompassing all nodes be defined as follows:

$$\{\delta\} = \left\{ u_1 \quad w_1 \quad \left(\tfrac{dw}{ds}\right)_1 \quad u_2 \quad w_2 \quad \left(\tfrac{dw}{ds}\right)_2 \quad \cdots \quad u_N \quad w_N \quad \left(\tfrac{dw}{ds}\right)_N \quad V \right\}^T \tag{5.61}$$

This nodal deflection vector corresponds to a disc with $N-1$ elements and N nodes. The voltage (V) component is a node shared by all piezo elements and is added onto the end of the global deflection vector described in Eq. (5.39). Retroactively, this adds an additional row and column of zeros to the mass and stiffness global matrices of the base layer, $[M_b]$ and $[K_b]$, and the global mass matrix of the piezo layer, $[M_p]$. For the purpose of global matrix formulation, and similarly to Eq. (5.41), the 7×7 piezo stiffness element $[K_{ep}]$ is divided into subcomponents:

$$[K_{ep}] = \left[\begin{array}{c|c|c} [K_{i,i}]_i & [K_{i,j}]_i & \{K_{i,V}\}_i \\ \hline [K_{j,i}]_i & [K_{j,j}]_i & \{K_{j,V}\}_i \\ \hline \{K_{V,i}\}_i^T & \{K_{V,j}\}_i^T & \{K_{V,V}\}_i \end{array}\right] \tag{5.62}$$

In Eq. (5.62), $\{K_{i,V}\}_i$ and $\{K_{j,V}\}_i$ are vectors of size 3×1 and $\{K_{V,i}\}_i^T$ and $\{K_{V,j}\}_i^T$ are of size 1×3. Also, $\{K_{V,V}\}_i$ is a 1×1 scalar term. Afterwards, the global piezo stiffness matrix is then compiled with matrix components from shared nodes added together, in a similar fashion to Eq. (5.43):

$[K_b] =$

$$\left[\begin{array}{c|c|c|c|c|c|c}
[K_{1,1}]_1 & [K_{1,2}] & 0_{3\times3} & \cdots & \cdots & 0_{3\times3} & \{K_{1,V}\}_1 \\ \hline
[K_{2,1}]_1 & \begin{matrix}[K_{2,2}]_1\\ +[K_{2,2}]_2\end{matrix} & [K_{2,3}]_2 & \ddots & \cdots & \vdots & \begin{matrix}\{K_{2,V}\}_1\\ +\{K_{2,V}\}_2\end{matrix} \\ \hline
0_{3\times3} & [K_{3,2}]_2 & \begin{matrix}[K_{3,3}]_2\\ +\dots\end{matrix} & \ddots & \ddots & \vdots & \begin{matrix}\{K_{3,V}\}_2\\ +\dots\end{matrix} \\ \hline
\vdots & \ddots & \ddots & \ddots & \ddots & 0_{3\times3} & \vdots \\ \hline
\vdots & \cdots & \ddots & \ddots & \begin{matrix}\dots+\\ [K_{N-1,N-1}]_{N-1}\end{matrix} & [K_{N-1,N}]_{N-1} & \begin{matrix}\dots+\\ \{K_{N-1,V}\}_{N-1}\end{matrix} \\ \hline
0_{3\times3} & \cdots & \cdots & 0_{3\times3} & [K_{N,N-1}]_{N-1} & [K_{N,N}]_{N-1} & \{K_{N,V}\}_{N-1} \\ \hline
\{K_{V,1}\}_1^T & \begin{matrix}\{K_{V,2}\}_1^T\\ +\{K_{V,2}\}_2^T\end{matrix} & \begin{matrix}\{K_{V,3}\}_2^T\\ +\dots\end{matrix} & \cdots & \begin{matrix}\dots+\\ \{K_{V,N-1}\}_{N-1}^T\end{matrix} & \{K_{V,N}\}_{N-1}^T & \begin{matrix}\{K_{V,V}\}_1+\dots\\ +\{K_{V,V}\}_{N-1}\end{matrix}
\end{array}\right] \tag{5.63}$$

The global piezo mass matrix $[M_p]$ is constructed exactly as the global mass matrix for the base layer, $[M_b]$, from Eq. (5.42), except with piezo material properties instead of aluminum.

5.7 Equation of Motion and Input Forces

The general equation of motion for a system is:

$$\begin{aligned}
&\Big[[M_b]+[M_p]\Big]\left\{\ddot{\delta}\right\}+\Big[[K_b]+[K_p]\Big]\{\delta\}=\{Q\} \\
&[M]\left\{\ddot{\delta}\right\}+[K]\{\delta\}=\{Q\}
\end{aligned} \tag{5.64}$$

In Eq. (5.64), $[M]$ is the sum of global mass matrix for the base and piezo layer and $[K]$ is the sum of the global stiffness matrices for the base and piezo layers. $\{Q\}$ represents the vector of input forces acting on the disc. The forces acting on the disc result only from the pressure in the resonator tube, meaning the only rows of $\{Q\}$ that are non zero correspond with the w_i rows in the global deflection vector $\{\delta\}$. The value for each non-zero row of $\{Q\}$ corresponding to node i in the system can be approximated as follows:

$$F_i = p_t A_{ni} \tag{5.65}$$

In Eq. (5.65), P_t is the pressure in the resonator tube as is defined in Chapters 3 and 4, and where A_{ni} is the area of each node as circumscribed by axially symmetric lines midway between node i and nodes $i-1$ and $i+1$. Therefore, for node i corresponding to radius r_i with length L defining the distance between nodes $(r_j - r_i)$, A_{ni} can be expressed as:

$$\begin{aligned} A_{ni} &= \pi(r_i + \frac{L}{2})^2 - \pi(r_i - \frac{L}{2})^2 \\ &= 2\pi r_i L \end{aligned} \tag{5.66}$$

But in the case where $r_i = 0$, as in the center of the disc at node 1:

$$A_{n1} = \pi \frac{L^2}{4} \tag{5.67}$$

And in the case of the N$^{\text{th}}$ node, where $r = R$, the radius of the disc:

$$
\begin{aligned}
A_{nN} &= \pi R^2 - \pi(R - \frac{L}{2})^2 \\
&= \pi \left(RL - \frac{L^2}{4} \right)
\end{aligned} \tag{5.68}
$$

Therefore the vector $\{Q\}$ can be expressed as:

$$
\begin{aligned}
\{Q\} &= p_t \left\{ \begin{array}{cccccccccccc} 0 & A_{n1} & 0 & \dots & 0 & A_{ni} & 0 & \dots & 0 & A_{nN} & 0 & 0 \end{array} \right\}^T \\
&= p_t \{Q^*\}
\end{aligned} \tag{5.69}
$$

Considering boundary conditions, since the disc is anchored at the outer radius, or in other words, since the N$^{\text{th}}$ node is fixed, the rows and columns of $[M]$, $[K]$, and $\{Q\}$ corresponding with the terms u_N, w_N, and $\left(\frac{dw}{ds}\right)_N$ in $\{\delta_e\}$ are eliminated. Also, because the system is axisymmetric it is assumed that u_1 and $\left(\frac{dw}{ds}\right)_1$, corresponding to the center of the disc is also equal to zero and the corresponding rows and columns are also eliminated.

5.8 Reformatting Electric Displacement Equation

In this section, static condensation, (Guyan Reduction) is performed on the system. Beginning by reformatting the second line of Eq. (5.44).

$$
\begin{aligned}
D_z &= \left\{ \begin{array}{cc} e_1 & e_1 \end{array} \right\} [B_2]\{\delta_e\} + \eta_3 \left\{ \begin{array}{ccc} 0 & 0 & \frac{1}{t} \end{array} \right\} [N_s]\{\delta_e\} \\
&= \{E_1\}^T\{\delta_e\} + \{E_2\}^T\{\delta_e\} \\
&= \{E_{eq}\}^T\{\delta_e\}
\end{aligned} \tag{5.70}
$$

In Eq. (5.70), the term $\{E_{eq}\}^T$ is a 1×7 vector. The term D_z is the electric displacement for each element corresponding to the element deflection vector $\{\delta_e\}$. Therefore, it can be stated for each element:

$$
\begin{aligned}
Q_1 &= \int_{r_1}^{r_2} D_1 dA = \int_0^L \{E_{eq}\}^T 2\pi(r_1+s)\{\delta_1\}ds = \{E_{eq}\}_1^T \{\delta_1\} \\
Q_2 &= \int_{r_2}^{r_3} D_2 dA = \int_0^L \{E_{eq}\}^T 2\pi(r_1+s)\{\delta_2\}ds = \{E_{eq}\}_2^T \{\delta_2\} \\
&\vdots \\
Q_{N-1} &= \int_{r_{N-1}}^{r_N} D_{N-1} dA = \int_0^L \{E_{eq}\}^T 2\pi(r_1+s)\{\delta_{N-1}\}ds = \{E_{eq}\}_{N-1}^T \{\delta_{N-1}\}
\end{aligned}
\tag{5.71}
$$

Then it can be said:

$$
\begin{aligned}
D_{piezo} &= \frac{Q}{A} = \frac{1}{A}\left(Q_1 + Q_2 + \ldots + Q_{N-1}\right) \\
&= \frac{1}{A}\left(\begin{array}{c} \{E_{eq}\}_1^T \{\delta_1\} + \{E_{eq}\}_2^T \{\delta_2\} + \ldots \\ + \{E_{eq}\}_{N-1}^T \{\delta_{N-1}\} \end{array}\right)
\end{aligned}
\tag{5.72}
$$

In Eq. (5.72), Q is the charge on the entire piezo disc, and A is the area of the piezo disc, or in other words, $A = \pi R^2$. As stated before, the term $\{E_{eq}\}^T$ is a 1×7 vector. Decomposing this term:

$$\{E_{eq}\}_i^T = \left\{ \begin{array}{ccccccc} E_{eq}(1)_i & E_{eq}(2)_i & E_{eq}(3)_i & E_{eq}(4)_i & E_{eq}(5)_i & E_{eq}(6)_i & E_{eq}(7)_i \end{array} \right\} \tag{5.73}$$

Therefore, by substituting $\{\delta_i\}$ from Eq. (5.44), Eq. (5.72) can be restated:

$$\begin{aligned} D_{piezo} = \; & \frac{1}{A}\left[E_{eq}(1)_1 u_1 + E_{eq}(1)_2 u_2 + \ldots + E_{eq}(1)_{N-1} u_{N-1} \right] \\ & + \frac{1}{A}\left[E_{eq}(2)_1 w_1 + E_{eq}(2)_2 w_2 + \ldots + E_{eq}(2)_{N-1} w_{N-1} \right] \\ & + \frac{1}{A}\left[E_{eq}(3)_1 \left(\tfrac{dw}{ds}\right)_1 + E_{eq}(3)_2 \left(\tfrac{dw}{ds}\right)_2 + \ldots + E_{eq}(3)_{N-1} \left(\tfrac{dw}{ds}\right)_{N-1} \right] \\ & + \frac{1}{A}\left[E_{eq}(4)_1 u_2 + E_{eq}(4)_2 u_3 + \ldots + E_{eq}(4)_{N-1} u_N \right] \\ & + \frac{1}{A}\left[E_{eq}(5)_1 w_2 + E_{eq}(5)_2 w_3 + \ldots + E_{eq}(5)_{N-1} w_N \right] \\ & + \frac{1}{A}\left[E_{eq}(6)_1 \left(\tfrac{dw}{ds}\right)_2 + E_{eq}(6)_2 \left(\tfrac{dw}{ds}\right)_3 + \ldots + E_{eq}(6)_{N-1} \left(\tfrac{dw}{ds}\right)_N \right] \\ & + \frac{1}{A}\left[E_{eq}(7)_1 + \ldots + E_{eq}(7)_{N-1} \right] V \end{aligned} \tag{5.74}$$

Rearranging Eq. (5.74):

$$\begin{aligned} D_{piezo} = \; & \frac{1}{A}\left[E_{eq}(1)_1\right] u_1 + \frac{1}{A}\left[E_{eq}(2)_1\right] w_1 + \frac{1}{A}\left[E_{eq}(3)_1\right] \left(\frac{dw}{ds}\right)_1 \\ & + \frac{1}{A}\left[E_{eq}(4)_1 + E_{eq}(1)_2\right] u_2 + \frac{1}{A}\left[E_{eq}(5)_1 + E_{eq}(2)_2\right] w_2 \\ & + \frac{1}{A}\left[E_{eq}(6)_1 + E_{eq}(3)_2\right] \left(\frac{dw}{ds}\right)_2 + \frac{1}{A}\left[E_{eq}(4)_2 + E_{eq}(1)_3\right] u_3 \\ & + \ldots \\ & + \frac{1}{A}\left[E_{eq}(4)_{N-2} + E_{eq}(1)_{N-1}\right] u_{N-1} + \frac{1}{A}\left[E_{eq}(5)_{N-2} + E_{eq}(2)_{N-1}\right] w_{N-1} \\ & + \left[E_{eq}(6)_{N-2} + E_{eq}(3)_{N-1}\right] \left(\frac{dw}{ds}\right)_{N-1} + \frac{1}{A}\left[E_{eq}(4)_{N-1}\right] u_N \end{aligned}$$

$$+\frac{1}{A}\left[E_{eq}(5)_{N-1}\right]w_N+\frac{1}{A}\left[E_{eq}(6)_{N-1}\right]\left(\frac{dw}{ds}\right)_N$$
$$+\frac{1}{A}\left[E_{eq}(7)_1+\ldots+E_{eq}(7)_{N-1}\right]V \tag{5.75}$$

which can be reformatted into:

$$D_{piezo}=\frac{Q}{A}=\{E_{total}\}^T\{\delta\} \tag{5.76}$$

The term $\{\delta\}$ from the second line of Eq. 5.76 is the global deflection vector from Eq. (5.55). Therefore $\{E_{total}\}^T$ is a vector of size $1\times(3N+1)$ corresponding to $\{\delta\}$. Therefore, from Eq. (5.75), the components of $\{E_{total}\}^T$ can be expressed as:

$$\begin{aligned}
E_{total}(1) &= \frac{1}{A}\left[E_{eq}(1)_1\right]\\
E_{total}(2) &= \frac{1}{A}\left[E_{eq}(2)_1\right]\\
E_{total}(3) &= \frac{1}{A}\left[E_{eq}(3)_1\right]\\
E_{total}(4) &= \frac{1}{A}\left[E_{eq}(4)_1+E_{eq}(1)_2\right]\\
E_{total}(5) &= \frac{1}{A}\left[E_{eq}(5)_1+E_{eq}(2)_2\right]\\
E_{total}(6) &= \frac{1}{A}\left[E_{eq}(6)_1+E_{eq}(3)_2\right]\\
E_{total}(7) &= \frac{1}{A}\left[E_{eq}(4)_2+E_{eq}(1)_2\right]\\
&\vdots\\
E_{total}(3N-5) &= \frac{1}{A}\left[E_{eq}(4)_{N-2}+E_{eq}(1)_{N-1}\right]\\
E_{total}(3N-4) &= \frac{1}{A}\left[E_{eq}(5)_{N-2}+E_{eq}(2)_{N-1}\right]\\
E_{total}(3N-3) &= \frac{1}{A}\left[E_{eq}(6)_{N-2}+E_{eq}(3)_{N-1}\right]
\end{aligned}$$

$$\begin{aligned}
E_{total}(3N-2) &= \frac{1}{A}\left[E_{eq}(4)_{N-1}\right] \\
E_{total}(3N-1) &= \frac{1}{A}\left[E_{eq}(5)_{N-1}\right] \\
E_{total}(3N) &= \frac{1}{A}\left[E_{eq}(6)_{N-1}\right] \\
E_{total}(3N+1) &= \frac{1}{A}\left[E_{eq}(7)_{1}+\ldots+E_{eq}(7)_{N-1}\right]
\end{aligned} \tag{5.77}$$

5.9 Model Reduction

Model reduction of this system begins by transforming Eq. (5.64) into the frequency domain as follows:

$$\begin{aligned}
[M]\left\{\ddot{\delta}\right\}+[K]\{\delta\} &= \{Q\} \\
\left[-\omega^2\,[M]+[K]\right]\{\delta\} &= \{Q\}
\end{aligned} \tag{5.78}$$

Solving for $\dot{Q}$ by transforming Eq. (5.76) into the frequency domain yields:

$$\dot{Q}=I=i\omega A\left\{E_{total}\right\}^T\{\delta\} \tag{5.79}$$

Applying the boundary conditions discussed in section 5.7, to both Eq. (5.78) and Eq. (5.79), the rows and columns of $[-\omega^2\,[M]+[K]]$ corresponding to the terms u_N, w_N, and $\left(\frac{dw}{ds}\right)_N$, u_1 and $\left(\frac{dw}{ds}\right)_1$ are eliminated. Additionally, the columns of $\{E_{total}\}^T$ and the rows of $\{Q\}$ are similarly eliminated. This transforms $\{\delta\}$ into a new $(3N-4)\times 1$ vector as follows:

$$\{\delta\} = \left\{ \begin{array}{cccccccccc} w_1 & u_2 & w_2 & \left(\frac{dw}{ds}\right)_2 & \cdots & u_{N-1} & w_{N-1} & \left(\frac{dw}{ds}\right)_{N-2} & V \end{array} \right\}^T \tag{5.80}$$

A new expression is created combining Eq. (5.78) and Eq. (5.79):

$$\begin{bmatrix} -\omega^2 [M] + [K] \\ i\omega A \{E_{total}\}^T \end{bmatrix} \{\delta\} = \left\{ \begin{array}{c} Q \\ I \end{array} \right\} \tag{5.81}$$

Then $\{\delta\}$ is the reordered into primary and secondary points, specifically, the first term in $\{\delta\}$, w_1 is moved to the second to last term:

$$\begin{aligned} \{\delta\} &= \left\{ \begin{array}{ccccccc|cc} u_2 & w_2 & \left(\frac{dw}{ds}\right)_2 & \cdots & u_{N-1} & w_{N-1} & \left(\frac{dw}{ds}\right)_{N-2} & w_1 & V \end{array} \right\}^T \\ &= \left\{ \begin{array}{c|c} \delta_s & \delta_p \end{array} \right\}^T \end{aligned} \tag{5.82}$$

In Eq. (5.82), $\{\delta_s\}$ is the first $3N - 6$ terms of the new, reordered $\{\delta\}$ vector and $\{\delta_p\}$ is the last two, specifically w_1 and V. This reordering requires to first column of $\begin{bmatrix} -\omega^2 [M] + [K] \\ i\omega \{E_{total}\}^T \end{bmatrix}$ to be moved to the second to last column. Next the rows of $\left\{ \begin{array}{c} Q \\ I \end{array} \right\}$ and $\begin{bmatrix} -\omega^2 [M] + [K] \\ i\omega \{E_{total}\}^T \end{bmatrix}$ are reordered such that the first row is moved to become the second to last as well. This results in the rearrangement of Eq. (5.81) to look like:

$$\left[\begin{array}{c|c} K_{ss} & K_{sp} \\ \hline K_{ps} & K_{pp} \end{array}\right] \left\{\begin{array}{c} \delta_s \\ \hline \delta_p \end{array}\right\} = \left\{\begin{array}{c} Q_s \\ \hline Q_p \end{array}\right\} = \left\{\begin{array}{c} Q(2) \\ \vdots \\ Q(3N-6) \\ \hline Q(1) \\ I \end{array}\right\} \tag{5.83}$$

The sizes of the matrix components from Eq. (5.83) are as follows: $[K_{ss}]$ is of size $(3N-5) \times (3N-6)$, $[K_{sp}]$ is of size $(3N-5) \times 2$, $[K_{ps}]$ is of size $2 \times (3N-6)$, and $[K_{pp}]$ is of size 2×2. Also, Q_s is of size $(3N-5) \times 1$. Note that from Eq. (5.69), $Q(1) = A_{n1} p_t$ Taking the first row of Eq. (5.83):

$$[K_{ss}]\{\delta_s\} + [K_{sp}]\{\delta_p\} = \{Q_s\} \tag{5.84}$$

Multiplying this expression by $[K_{ss}]^T$:

$$[K_{ss}]^T [K_{ss}]\{\delta_s\} + [K_{ss}]^T[K_{sp}]\{\delta_p\} = [K_{ss}]^T\{Q_s\} \tag{5.85}$$

Now solving for $\{\delta_s\}$:

$$\{\delta_s\} = -\Big[[K_{ss}]^T[K_{ss}]\Big]^{-1} [K_{ss}]^T[K_{sp}]\{\delta_p\} + \Big[[K_{ss}]^T[K_{ss}]\Big]^{-1} [K_{ss}]^T\{Q_s\} \tag{5.86}$$

Taking the second row of Eq. (5.83):

$$[K_{ps}]\{\delta_s\} + [K_{pp}]\{\delta_p\} = \{Q_p\} \tag{5.87}$$

Incorporating $\{\delta_s\}$ from Eq. (5.86) into Eq. (5.87) and simplifying:

$$\begin{aligned} &\left[[K_{pp}] - [K_{ps}]\left[[K_{ss}]^T[K_{ss}]\right]^{-1}[K_{ss}]^T[K_{sp}]\right]\{\delta_p\} \\ &= -[K_{ps}]\left[[K_{ss}]^T[K_{ss}]\right]^{-1}[K_{ss}]^T\{Q_s\} + \{Q_p\} \end{aligned} \tag{5.88}$$

For convention call:

$$[R] = \left[[K_{pp}] - [K_{ps}]\left[[K_{ss}]^T[K_{ss}]\right]^{-1}[K_{ss}]^T[K_{sp}]\right] \tag{5.89}$$

where $[R]$ is a 2×2 matrix. Also for convention, because Q_s is a $(3N-5) \times 1$ that is function of p_t:

$$p_t \begin{Bmatrix} Q_{s1} \\ Q_{s2} \end{Bmatrix} = -[K_{ps}]\left[[K_{ss}]^T[K_{ss}]\right]^{-1}[K_{ss}]^T\{Q_s\} \tag{5.90}$$

Therefore using Eq. (5.90), Eq. (5.89) and substituting the expression for $\{Q_p\}$from Eq. (5.83), Eq. (5.88) can be rewritten as:

$$[R]\{\delta_p\} = p_t \begin{Bmatrix} Q_{s1} \\ Q_{s2} \end{Bmatrix} + \begin{Bmatrix} A_{n1}p_t \\ I \end{Bmatrix} = \begin{bmatrix} Q_{s1} + A_{n1} & 0 \\ Q_{s2} & 1 \end{bmatrix} \begin{Bmatrix} p_t \\ I \end{Bmatrix} \tag{5.91}$$

Rearranging and substituting the expression for $\{\delta_p\}$ from Eq. (5.83):

$$\begin{bmatrix} Q_{s1} + A_{n1} & 0 \\ Q_{s2} & 1 \end{bmatrix}^{-1} [R] \begin{Bmatrix} w_1 \\ V \end{Bmatrix} = \begin{Bmatrix} p_t \\ I \end{Bmatrix}$$

$$\Big[F(i\omega)\Big] \begin{Bmatrix} w_1 \\ V \end{Bmatrix} = \begin{Bmatrix} p_t \\ I \end{Bmatrix} \tag{5.92}$$

In Eq. (5.92), $\Big[F(i\omega)\Big]$ is a 2×2 matrix in the frequency domain. For convention set:

$$\Big[F(i\omega)\Big] = \begin{bmatrix} F_{i\omega}(1) & F_{i\omega}(2) \\ F_{i\omega}(3) & F_{i\omega}(4) \end{bmatrix} \tag{5.93}$$

Therefore from Eq. (5.92):

$$\begin{bmatrix} F_{i\omega}(1) & F_{i\omega}(2) \\ F_{i\omega}(3) & F_{i\omega}(4) \end{bmatrix} \begin{Bmatrix} w_1 \\ V \end{Bmatrix} = \begin{Bmatrix} p_t \\ I \end{Bmatrix} \tag{5.94}$$

Therefore, rearranging this expression yields:

$$\begin{bmatrix} F_{i\omega}(1) - \frac{F_{i\omega}(2)F_{i\omega}(3)}{F_{i\omega}(4)} & \frac{F_{i\omega}(2)}{F_{i\omega}(4)} \\ -\frac{F_{i\omega}(3)}{F_{i\omega}(4)} & \frac{1}{F_{i\omega}(4)} \end{bmatrix} \begin{Bmatrix} w_1 \\ I \end{Bmatrix} = \begin{Bmatrix} p_t \\ V \end{Bmatrix} \tag{5.95}$$

Eq. (5.95) presents a two-part impedance matrix of the coupled electromechanical system of the composite piezoelectric diaphragm. The next section of the chapter will show some plots from this finite element analysis.

5.10 Plots from Finite Element Model

The frequency response of V and w_1 from the reduced system, assuming the piezo is unloaded, is seen in Fig. 5.3. This being the case, the current across the piezo is zero, and the voltage can be easily calculated for a sinusoidal pressure input in Eq. (5.95). For a two element system, the most basic finite element model for the system, the calculated first mode peak for the aluminum-piezo combined disc is located at 1,532 Hz for both the center of the disc and the voltage across the piezo-disc.

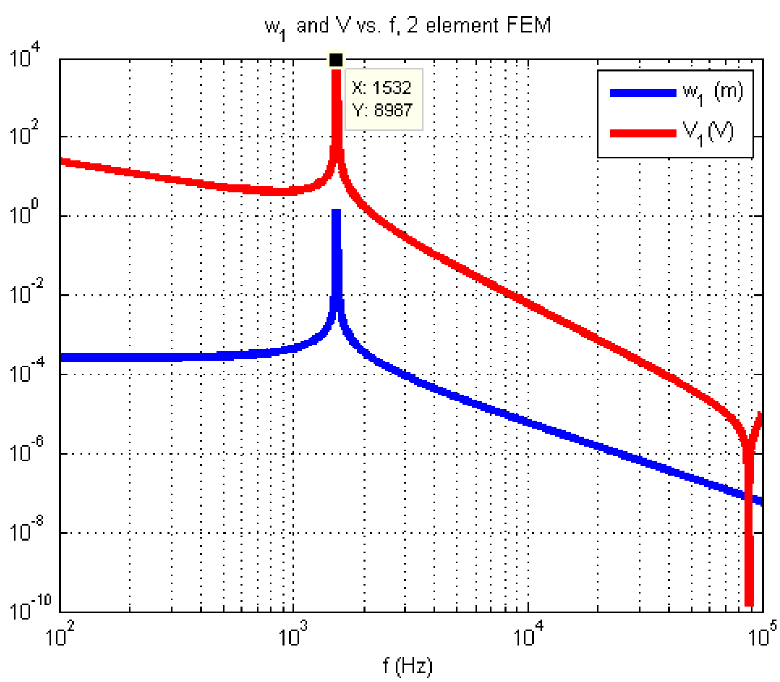

Figure 5.3: Frequency response plot for w_1 and V from the reduced system model, 2 element system.

To confirm the results from Fig. 5.3, a laser-vibrometer was used to calculate the displacement amplitude of the center of the piezo disc due to sinusoidal forcing input from a shaker. Experimental set-up is discussed in Chapter 7. Samples were manually taken every 50Hz from the laser-vibrometer. This is plotted in Fig. 5.4 over the frequency range of 600-1600 Hz.

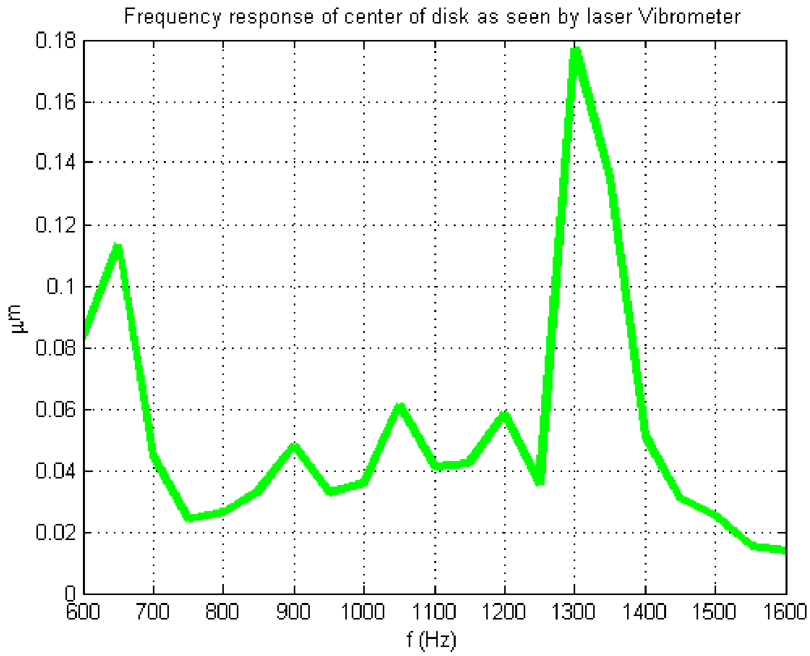

Figure 5.4: Frequency response of the composite piezoelectric disc as determine by the laser vibrometer.

The laser vibrometer gives a plot of the displacement amplitude at a given input frequency. The displacement amplitude of the piezo-disc as seen by the laser vibrometer is shown in Fig. 5.5. The image shows the displacement amplitude of the top half of the composite piezo disc combined system as analyzed by the laser vibrometer. Since the system is symmetrical, the bottom half is assumed to be a mirror image of the top half. Also seen in Fig. 5.5 is the black and white image of the stinger connected to the shaker used to excite the system. As can be seen in the figure, at $1300Hz$ the center of the disc is calculated to oscillate with an amplitude of $177.3nm$. The image shows that the oscillation at $1300Hz$ is the first mode of vibration for the disc system.

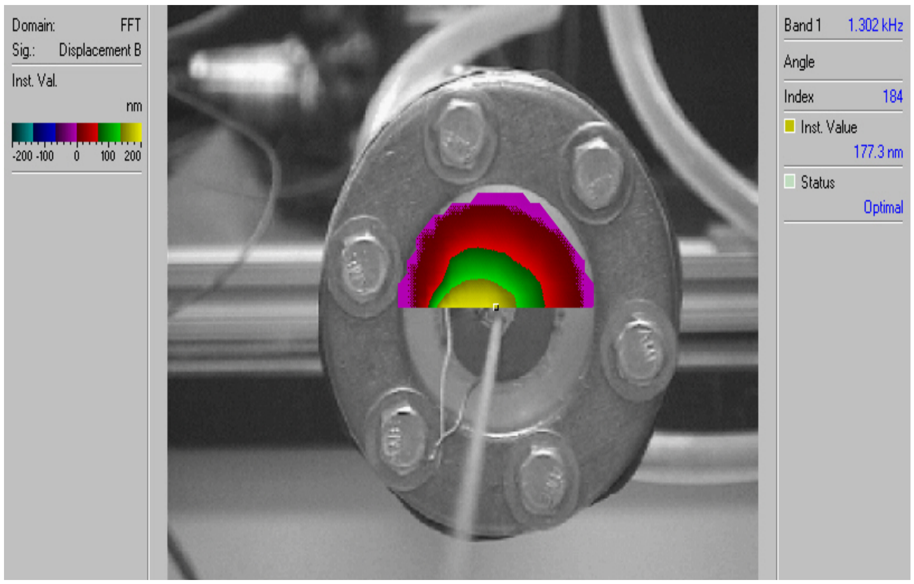

Figure 5.5: Displacement amplitude as measured by laser vibrometer at 1300 Hz.

The plot of the disc system as modeled by ANSYS calculates the first mode of vibration to be $1250Hz$, as seen in Fig. 5.6. The text file used for the ANSYS simulation and the next three modes of oscillation for the disc can be seen in Appendix D. ANSYS produces a finer mesh than the relatively simple two element model discussed in this chapter, and the figure clearly shows the disc in the first mode of oscillation.

Another plot of the frequency response of the system was generated by exciting the disc system using the shaker, but instead of exciting at specific frequencies, a white-noise input was applied to the shaker. Then, using Fast Fourier Transform (FFT) of the open circuit output from the electrodes of the piezo-disc, a frequency

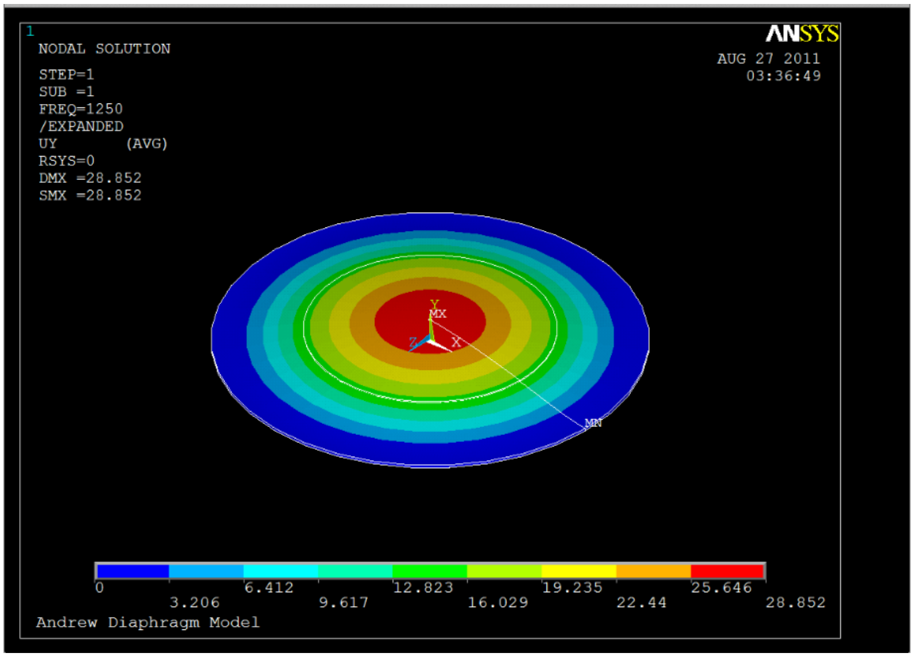

Figure 5.6: Plot of first mode of composite piezoelectric disc system as measured by ANSYS. Frequency is calculated to be 1250 Hz.

plot was generated. This is seen in Fig. 5.7 and shows a peak centered at $1220Hz$.

Tabulating these methods of calculating the first mode of vibration in Tab. 5.1, it can be seen that while the two element FEM model gives an estimate for the first mode of vibration in the ballpark of the experimental values, the ANSYS model, with a finer mesh of elements gives a very close calculation of the experimental values.

MODE 1 NATURAL FREQUENCIES: THEORY AND EXPERIMENT

	Theoretical		*Experimental*	
	2 Element FEM	ANSYS	White-noise frequency response	Laser-Vibrometer analysis
frequency (Hz)	1532	1250	1220	~1300

Table 5.1: Theoretical and experimental first natural frequency of the composite piezoelectric disc

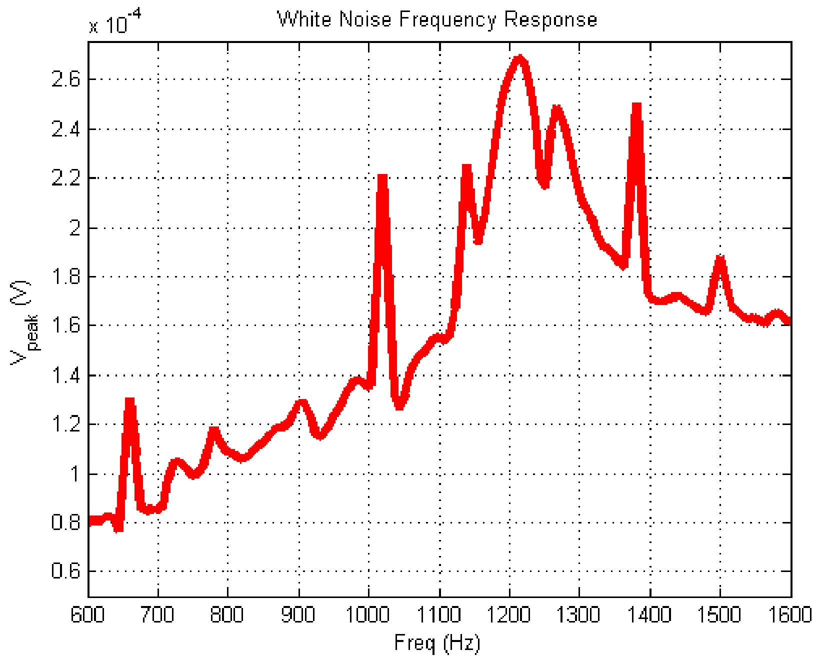

Figure 5.7: Frequency response of the composite piezoelectric disc due to white noise input.

5.11 Using the FEM Model to Interface with DeltaEC

DeltaEC requires the real and imaginary impedance input from the aluminum and piezo combined structure. In order to determine this, the two-part impedance matrix needs to be modified to include the volume flow rate due to movement of the disc instead of the deflection w. The equation for volume flow rate for each element can be determined as follows:

$$\overset{*}{V}_e = \int_{r_i}^{r_j} \dot{w} 2\pi r dr \tag{5.96}$$

Which, incorporating equation 5.45 and 5.18 and 5.19 can be written as:

$$
\begin{aligned}
\overset{*}{V}_e &= \int_0^L \left\{ \begin{array}{ccc} 0 & 1 & 0 \end{array} \right\} [N_s]\{\dot{\delta}_e\} 2\pi(r_i + s) ds \\
&= \int_0^L \left\{ \begin{array}{ccc} 0 & 1 & 0 \end{array} \right\} [N_s] 2\pi(r_i + s) ds \{\dot{\delta}_e\} \\
&= \{Z_{eq}\}^T \{\dot{\delta}_e\} \qquad (5.97)
\end{aligned}
$$

In Eq. (5.97), the term $\{Z_{eq}\}^T$ is a 1×7 vector. Therefore, it can be stated for each element:

$$
\begin{aligned}
\overset{*}{V}_1 &= \{Z_{eq}\}_1^T \{\dot{\delta}_1\} \\
\overset{*}{V}_2 &= \{Z_{eq}\}_2^T \{\dot{\delta}_2\} \\
&\vdots \\
\overset{*}{V}_{N-1} &= \{Z_{eq}\}_{N-1}^T \{\dot{\delta}_{N-1}\} \qquad (5.98)
\end{aligned}
$$

Then, it can be said:

$$
\begin{aligned}
\overset{*}{V} &= \overset{*}{V}_1 + \overset{*}{V}_2 + \ldots + \overset{*}{V}_{N-1} \\
&= \{Z_{eq}\}_1^T \{\dot{\delta}_1\} + \{Z_{eq}\}_2^T \{\dot{\delta}_2\} + \ldots + \{Z_{eq}\}_{N-1}^T \{\dot{\delta}_{N-1}\} \qquad (5.99)
\end{aligned}
$$

As stated before, $\{Z_{eq}\}^T$ is a 1×7 vector. Decomposing this term:

$$
\{Z_{eq}\}_i^T = \left\{ \begin{array}{ccccccc} Z_{eq}(1)_i & Z_{eq}(2)_i & Z_{eq}(3)_i & Z_{eq}(4)_i & Z_{eq}(5)_i & Z_{eq}(6)_i & Z_{eq}(7)_i \end{array} \right\} \qquad (5.100)
$$

Therefore, by substituting $\{\delta_i\}$ from Eq. (5.44), Eq. (5.99) can be restated:

$$
\begin{aligned}
\overset{*}{V} = \; & i\omega \Big[Z_{eq}(1)_1 u_1 + Z_{eq}(1)_2 u_2 + \ldots + Z_{eq}(1)_{N-1} u_{N-1} \\
& + Z_{eq}(2)_1 w_1 + Z_{eq}(2)_2 w_2 + \ldots + Z_{eq}(2)_{N-1} w_{N-1} \\
& + Z_{eq}(3)_1 \left(\frac{dw}{ds}\right)_1 + Z_{eq}(3)_2 \left(\frac{dw}{ds}\right)_2 + \ldots + Z_{eq}(3)_{N-1} \left(\frac{dw}{ds}\right)_{N-1} \\
& + Z_{eq}(4)_1 u_2 + Z_{eq}(4)_2 u_3 + \ldots + Z_{eq}(4)_{N-1} u_N \\
& + Z_{eq}(5)_1 w_2 + Z_{eq}(5)_2 w_3 + \ldots + Z_{eq}(5)_{N-1} w_N \\
& + Z_{eq}(6)_1 \left(\frac{dw}{ds}\right)_2 + Z_{eq}(6)_2 \left(\frac{dw}{ds}\right)_3 + \ldots + Z_{eq}(6)_{N-1} \left(\frac{dw}{ds}\right)_N \\
& + \left[Z_{eq}(7)_1 + \ldots + Z_{eq}(7)_{N-1} \right] V \Big]
\end{aligned}
\tag{5.101}
$$

Rearranging Eq. (5.101):

$$
\begin{aligned}
\overset{*}{V} = \; & i\omega \left[Z_{eq}(1)_1 \right] u_1 + i\omega \left[Z_{eq}(2)_1 \right] w_1 + i\omega \left[Z_{eq}(3)_1 \right] \left(\frac{dw}{ds}\right)_1 \\
& + i\omega \left[Z_{eq}(4)_1 + Z_{eq}(1)_2 \right] u_2 + i\omega \left[Z_{eq}(5)_1 + Z_{eq}(2)_2 \right] w_2 \\
& + i\omega \left[Z_{eq}(6)_1 + Z_{eq}(3)_2 \right] \left(\frac{dw}{ds}\right)_2 + i\omega \left[Z_{eq}(4)_2 + Z_{eq}(1)_3 \right] u_3 \\
& + \ldots \\
& + i\omega \left[Z_{eq}(4)_{N-2} + Z_{eq}(1)_{N-1} \right] u_{N-1} + i\omega \left[Z_{eq}(5)_{N-2} + Z_{eq}(2)_{N-1} \right] w_{N-1} \\
& + \left[Z_{eq}(6)_{N-2} + Z_{eq}(3)_{N-1} \right] \left(\frac{dw}{ds}\right)_{N-1} + i\omega \left[Z_{eq}(4)_{N-1} \right] u_N \\
& + i\omega \left[Z_{eq}(5)_{N-1} \right] w_N + i\omega \left[Z_{eq}(6)_{N-1} \right] \left(\frac{dw}{ds}\right)_N \\
& + i\omega \left[Z_{eq}(7)_1 + \ldots + E_{eq}(7)_{N-1} \right] V
\end{aligned}
\tag{5.102}
$$

which can be reformatted into:

$$\overset{*}{V} = i\omega \left\{ Z_{total} \right\}^T \left\{ \delta \right\} \tag{5.103}$$

The term $\{\delta\}$ from Eq. (5.103) is the global deflection vector from Eq. (5.55). Therefore $\{Z_{total}\}^T$ is a vector of size $1 \times (3N+1)$ corresponding to $\{\delta\}$. Therefore, from Eq. (5.102), the components of $\{Z_{total}\}^T$ can be expressed as:

$$\begin{aligned}
Z_{total}(1) &= i\omega \left[Z_{eq}(1)_1 \right] \\
Z_{total}(2) &= i\omega \left[Z_{eq}(2)_1 \right] \\
Z_{total}(3) &= i\omega \left[Z_{eq}(3)_1 \right] \\
Z_{total}(4) &= i\omega \left[Z_{eq}(4)_1 + Z_{eq}(1)_2 \right] \\
Z_{total}(5) &= i\omega \left[Z_{eq}(5)_1 + Z_{eq}(2)_2 \right] \\
Z_{total}(6) &= i\omega \left[Z_{eq}(6)_1 + Z_{eq}(3)_2 \right] \\
Z_{total}(7) &= i\omega \left[Z_{eq}(4)_2 + Z_{eq}(1)_2 \right] \\
&\vdots \\
Z_{total}(3N-5) &= i\omega \left[Z_{eq}(4)_{N-2} + Z_{eq}(1)_{N-1} \right] \\
Z_{total}(3N-4) &= i\omega \left[Z_{eq}(5)_{N-2} + Z_{eq}(2)_{N-1} \right] \\
Z_{total}(3N-3) &= i\omega \left[Z_{eq}(6)_{N-2} + Z_{eq}(3)_{N-1} \right] \\
Z_{total}(3N-2) &= i\omega \left[Z_{eq}(4)_{N-1} \right] \\
Z_{total}(3N-1) &= i\omega \left[Z_{eq}(5)_{N-1} \right] \\
Z_{total}(3N) &= i\omega \left[Z_{eq}(6)_{N-1} \right] \\
Z_{total}(3N+1) &= i\omega \left[Z_{eq}(7)_1 + \ldots + Z_{eq}(7)_{N-1} \right] \qquad (5.104)
\end{aligned}$$

By using Eq. (5.79) and Eq. (5.103):

$$\left\{ \begin{array}{c} \overset{*}{V} \\ \\ I \end{array} \right\} = i\omega \left\{ \begin{array}{c} \{Z_{total}\}^T \{\delta\} \\ \\ A\{E_{total}\}^T \{\delta\} \end{array} \right\} \tag{5.105}$$

Decomposing this expression by extracting the last term from $\{\delta_e\}$, that is, V from Eq. (5.105):

$$\begin{aligned} \left\{ \begin{array}{c} \overset{*}{V} \\ \\ I \end{array} \right\} &= i\omega \left\{ \left[\begin{array}{ccc} Z_{total}(1) & \dots & Z_{total}(3N) \\ \\ AE_{total}(1) & \dots & AE_{total}(3N) \end{array} \right] \{\delta\}_{3N} + \left\{ \begin{array}{c} Z_{total}(3N+1) \\ \\ AE_{total}(3N+1) \end{array} \right\} V \right\} \\ &= i\omega \left\{ [ZE]_{3N} \{\delta\}_{3N} + \{ZE\}_{3N+1} V \right\} \end{aligned} \tag{5.106}$$

where:

$$[ZE]_{3N} = \left[\begin{array}{ccc} Z_{total}(1) & \dots & Z_{total}(3N) \\ \\ AE_{total}(1) & \dots & AE_{total}(3N) \end{array} \right] \tag{5.107}$$

and:

$$\{ZE\}_{3N+1} = \left\{ \begin{array}{c} Z_{total}(3N+1) \\ \\ AE_{total}(3N+1) \end{array} \right\} \tag{5.108}$$

In Eq. (5.106), the term $\{\delta\}_{3N}$ refers to the first $3N$ terms of $\{\delta\}$. Therefore, from Eq. (5.78), with grouping terms, it can be stated that:

$$
\begin{array}{l}
\left[-\omega^2 [M] + [K]\right]\{\delta\} = \{Q^*\}p_t \\
\left[\begin{array}{c|c}
\left[-\omega^2 [M] + [K]\right]_{\delta\delta} & \left[-\omega^2 [M] + [K]\right]_{\delta V} \\
\hline
\left[-\omega^2 [M] + [K]\right]_{V\delta} & \left[-\omega^2 [M] + [K]\right]_{VV}
\end{array}\right]
\left\{\begin{array}{c} \delta_{3N} \\ V \end{array}\right\} = \left\{\begin{array}{c} \{Q^*\}_{3N}p_t \\ 0 \end{array}\right\} \\
\left[\begin{array}{c|c}
[\omega MK]_{\delta\delta} & [\omega MK]_{\delta V} \\
\hline
[\omega MK]_{V\delta} & [\omega MK]_{VV}
\end{array}\right]
\left\{\begin{array}{c} \delta_{3N} \\ V \end{array}\right\} = \left\{\begin{array}{c} \{Q^*\}_{3N}p_t \\ 0 \end{array}\right\}
\end{array}
\tag{5.109}
$$

For convention, say $\left[-\omega^2 [M] + [K]\right] = [\omega MK]$. In Eq. 5.109, $[\omega MK]_{\delta\delta}$ refers to the first $3N$ rows and columns of $\left[-\omega^2 [M] + [K]\right]$, $[\omega MK]_{\delta V}$ refers to the first $3N$ rows of the last column of $[\omega MK]$, while $[\omega MK]_{V\delta}$ refers to the first $3N$ columns of the last row of the matrix, and $[\omega MK]_{VV}$ refers to the last term in the matrix. Also, $\{Q^*\}_{3N}$ refers to the first $3N$ terms of $\{Q^*\}$ as defined in Eq. (5.70). Applying the boundary conditions discussed in section 5.7, to Eq. (5.109), the rows and columns of $[\omega MK]$ corresponding to the terms u_N, w_N, and $\left(\frac{dw}{ds}\right)_N$, u_1 and $\left(\frac{dw}{ds}\right)_1$ are eliminated. Additionally, the columns of $\{E_{total}\}^T$, $\{Z_{total}\}^T$, and the rows of $\{Q^*\}_{3N}$ are similarly eliminated.

From the first row of Eq. (5.109):

$$
[\omega MK]_{\delta\delta}\{\delta\}_{3N} + [\omega MK]_{\delta V} V = \{Q^*\}_{3N}p_t \tag{5.110}
$$

which reduces to:

$$
\{\delta\}_{3N} = -[\omega MK]_{\delta\delta}^{-1}[\omega MK]_{\delta V} V + [\omega MK]_{\delta\delta}^{-1}\{Q^*\}_{3N}p_t \tag{5.111}
$$

Therefore, Eq. (5.107) can be restated as:

$$\left\{ \begin{array}{c} \overset{*}{V} \\ \\ I \end{array} \right\} = i\omega \left\{ \begin{array}{l} [ZE]_{3N} \left[\omega MK\right]_{\delta\delta}^{-1} \{Q^*\}_{3N} p_t \\ \\ + \left[\{ZE\}_{3N+1} - \left[\omega MK\right]_{\delta\delta}^{-1} \left[\omega MK\right]_{\delta V}\right] V \end{array} \right\} \tag{5.112}$$

Therefore:

$$\left\{ \begin{array}{c} \overset{*}{V} \\ \\ I \end{array} \right\} = i\omega \left[\begin{array}{ccc} \left\{[ZE]_{3N} \left[\omega MK\right]_{\delta\delta}^{-1} \{Q^*\}_{3N}\right\} & , & \left\{ \begin{array}{l} \{ZE\}_{3N+1} \\ \\ - \left[\omega MK\right]_{\delta\delta}^{-1} \left[\omega MK\right]_{\delta V} \end{array} \right\} \end{array} \right] \left\{ \begin{array}{c} p_t \\ \\ V \end{array} \right\} \tag{5.113}$$

Therefore, the 2×2 matrix from which the impedance for the aluminum piezo combined disc is determined, $[Z_p]$ can be defined as:

$$[Z_p] = i\omega \left[\left\{[ZE]_{3N} \left[\omega MK\right]_{\delta\delta}^{-1} \{Q^*\}_{3N}\right\} \quad , \quad \left\{\{ZE\}_{3N+1} - \left[\omega MK\right]_{\delta\delta}^{-1} \left[\omega MK\right]_{\delta V}\right\} \right] \tag{5.114}$$

Therefore:

$$\left\{ \begin{array}{c} \overset{*}{V} \\ \\ I \end{array} \right\} = [Z_p] \left\{ \begin{array}{c} P_t \\ \\ V \end{array} \right\} \tag{5.115}$$

Rearranging this expression:

$$\left\{ \begin{array}{c} P_t \\ \\ V \end{array} \right\} = [Z_p]^{-1} \left\{ \begin{array}{c} \overset{*}{V} \\ \\ I \end{array} \right\} \tag{5.116}$$

The result of this analysis gives a 2×2 matrix coupling the mechanical and electrical impedance of the composite piez-disc system which make up the end cap of the resonator section of the TWTAE. At $91.6Hz$, the acting frequency of the pressure oscillations in the TWTAE, the expression for $[Z_p]^{-1}$ was determined to be:

$$\begin{Bmatrix} P_t \\ \\ V \end{Bmatrix} = \begin{bmatrix} 0 - 4.006 \times 10^8 i & 0 + 1.100 \times 10^5 i \\ \\ 0 - 1.260 \times 10^6 i & 0 - 4.000 \times 10^4 i \end{bmatrix} \begin{Bmatrix} \overset{*}{V} \\ \\ I \end{Bmatrix} \tag{5.117}$$

These values are the implemented in the `IEDUCER` segment of the DeltaEC code shown in Chapter 6.

5.12 Summary

This chapter has presented an axisymmetric finite element model of a composite piezo-disc which is used to convert the acoustic energy of the thermoacoustic engine into electrical energy. The model is used to develop a two-part impedance matrix of the piezo-disc which can be easily integrated with the software DeltaEC to predict the performance to the TWTAE. The predictions of the developed FEM are validated against the predictions of the commercial software package ANSYS and experimentally using a scanning laser vibrometer. The predictions of the model are shown to be in excellent agreement with ANSYS prediction as well as experimental results.

Chapter 6

DeltaEC Numerical Analysis of the TWTAE

DeltaEC is a software which is capable of numerically analyzing sophisticated acoustic systems and solving for complex pressure and volume flow rate [13]. The system assumes the systems behave sinusoidally and determines the frequency and amplitude. The text file code upon which DeltaEC used to analyze this lab's TWTAE is written below in Section 6.1. Meanwhile, the user defined gas mixture used for the code is seen below. The gas mixture used is 0% helium and 100% air.

6.1 DeltaEC traveling wave thermoacoustic engine code

Fig. 6.1 and Fig. 6.2 shows the DeltaEC model of the experimental prototype of the TWTAE which is described in Chapter 7.

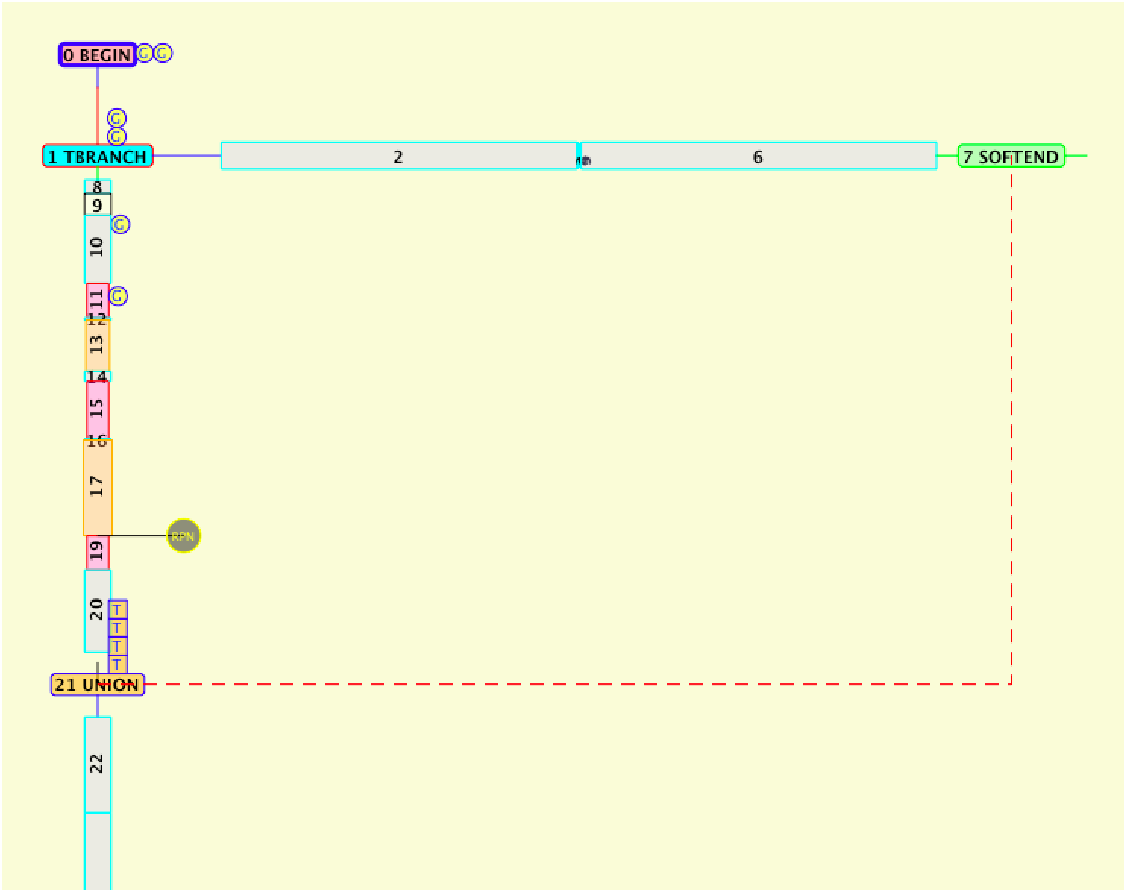

Figure 6.1: Schematic of looped portion of the TWTAE analyzed by DeltaEC.

The code of the DeltaEC software which is used to model the prototype of the TWTAE is listed in Table 6.1.

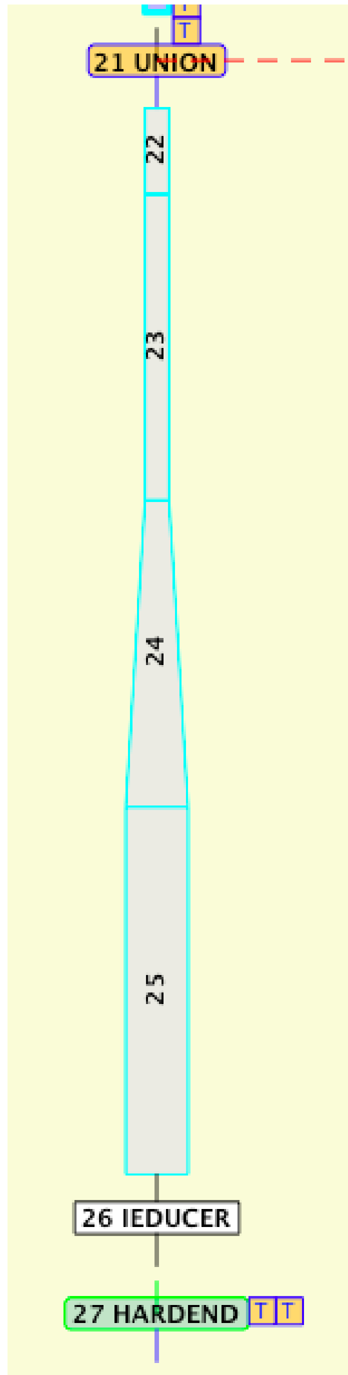

Figure 6.2: Schematic of resonator portion of the TWTAE analyzed by DeltaEC.

Meanwhile the gas mixture text file used for the DeltaEC program is shown in Table 6.1.

Table 6.1 - DeltaEC Code

```
\Save6_no_surface_piezo_354_7W.out
!Created@18:00:58  27-Sep-2011 with DeltaEC version 6.2b3 under win32,
using Win 5.1.2600 (Service Pack 3) under Python DeltaEC.
!---------------------------------  0 ---------------------------------
BEGIN      the setup
 8.2737E+05 a Mean P Pa
   89.195   b Freq   Hz       G
  300.07    c TBeg   K
 1.9557E+05 d |p|    Pa       G
     0.0000 e Ph(p)  deg
     0.0000 f |U|    m^3/s
     0.0000 g Ph(U)  deg
     0.0000 i Ndot   mol/s
     0.0000 j nL
air_0.tpm           Gas type
!---------------------------------  1 ---------------------------------
TBRANCH    Split up the flow
-4.1073E+07 a Re(Zb) Pa-s/m^3 G         1.9557E+05 A |p|    Pa
 6.5203E+07 b Im(Zb) Pa-s/m^3 G             0.0000 B Ph(p)  deg
     0.0000 d NdotBr mol/s              2.5378E-03 C |U|    m^3/s
     0.0000 e NLdotB mol/s              -122.21    D Ph(U)  deg
                                        -132.27    E HtotBr W
                                        -132.27    F EdotBr W
                                         132.27    G EdotTr W
!---------------------------------  2 ---------------------------------
DUCT       180 bend plus brass connecting flange (pg 27 book 4)
 3.0000E-04 a Area   m^2      Mstr      1.6876E+05 A |p|    Pa
 6.1399E-02 b Perim  m        2a           2.1973  B Ph(p)  deg
    0.2600  c Length m                  9.2381E-03 C |U|    m^3/s
                                         -97.824   D Ph(U)  deg
                                        -132.27    E Htot   W
stainless           Solid type          -135.65    F Edot   W
!---------------------------------  3 ---------------------------------
CONE       4" to 3" Concentric reducer (pg 36 book 4)
 3.0000E-04 a AreaI  m^2      Mstr      1.6856E+05 A |p|    Pa
 6.1368E-02 b PerimI m        3a           2.2101  B Ph(p)  deg
 1.0000E-03 c Length m                  9.2582E-03 C |U|    m^3/s
 2.0000E-04 d AreaF  m^2      Mstr       -97.803   D Ph(U)  deg
 5.0134E-02 e PerimF m        3d        -132.27    E Htot   W
stainless           Solid type          -135.66    F Edot   W
```

DeltaEC Code Continued

```
!--------------------------------- 4 ---------------------------------
DUCT       3" FB Duct - Length given in concept.skf
 2.0000E-04 a Area   m^2      Mstr       1.6831E+05 A |p|    Pa
 5.0134E-02 b Perim  m        4a            2.2259  B Ph(p)  deg
 1.0000E-03 c Length m                   9.2743E-03 C |U|    m^3/s
                                          -97.786   D Ph(U)  deg
                                         -132.27    E Htot   W
stainless           Solid type           -135.68    F Edot   W
!--------------------------------- 5 ---------------------------------
CONE       3.5" to 3" Long radius reducing elbow (pg 36 book 4)
 2.0000E-04 a AreaI  m^2      Mstr       1.6811E+05 A |p|    Pa
 5.0134E-02 b PerimI m        5a            2.2387  B Ph(p)  deg
 1.0000E-03 c Length m                   9.2943E-03 C |U|    m^3/s
 3.0000E-04 d AreaF  m^2      Mstr        -97.764   D Ph(U)  deg
 6.1413E-02 e PerimF m        5d         -132.27    E Htot   W
stainless           Solid type           -135.7     F Edot   W
!--------------------------------- 6 ---------------------------------
DUCT       FB connector/part of tee (Pg 55 book 4 concept.skf)
 3.0000E-04 a Area   m^2      Mstr       1.1188E+05 A |p|    Pa
 6.1414E-02 b Perim  m        6a            6.2867  B Ph(p)  deg
    0.2600  c Length m                   1.4609E-02 C |U|    m^3/s
                                          -93.596   D Ph(U)  deg
                                         -132.27    E Htot   W
stainless           Solid type           -140.26    F Edot   W
!--------------------------------- 7 ---------------------------------
SOFTEND    End of feedback branch
     0.0000 a Re(z)                      1.1188E+05 A |p|    Pa
     0.0000 b Im(z)                         6.2867  B Ph(p)  deg
     0.0000 c Htot   W                   1.4609E-02 C |U|    m^3/s
                                          -93.596   D Ph(U)  deg
                                         -132.27    E Htot   W
                                         -140.26    F Edot   W
                                        -0.11821    G Re(z)
                                            0.6785  H Im(z)
                                          300.07    I T      K
                                        -0.32112    J p2OHL  Pa
                                             0.0000 K nL
!--------------------------------- 8 ---------------------------------
DUCT Change Me
 3.0000E-04 a Area   m^2      Mstr       1.9593E+05 A |p|    Pa
 6.1399E-02 b Perim  m        8a        -7.2465E-02 B Ph(p)  deg
 1.0000E-02 c Length m                   2.3007E-03 C |U|    m^3/s
                                           54.031   D Ph(U)  deg
                                          132.27    E Htot   W
ideal           Solid type                132.15    F Edot   W
```

```
!--------------------------------  9 --------------------------------
MINOR      minor loss here
 2.9364E-05 a Area   m^2      G          1.8975E+05 A |p|    Pa
    0.8000  b K+                           -2.7367  B Ph(p)  deg
 7.0000E-02 c K-                         2.3007E-03 C |U|    m^3/s
                                           54.031   D Ph(U)  deg
                                          132.27    E Htot   W
                                          119.62    F Edot   W
!-------------------------------- 10 --------------------------------
DUCT       jetting space
 3.0000E-04 a Area   m^2      Mstr       1.9086E+05 A |p|    Pa
 6.1435E-02 b Perim  m        10a          -3.0809  B Ph(p)  deg
 5.0000E-02 c Length m                   1.3615E-03 C |U|    m^3/s
                                           20.494   D Ph(U)  deg
                                          132.27    E Htot   W
ideal           Solid type                119.08    F Edot   W
!-------------------------------- 11 --------------------------------
HX Change Me
 3.0000E-04 a Area   m^2                 1.9095E+05 A |p|    Pa
    0.6800  b GasA/A                       -3.3629  B Ph(p)  deg
 2.5000E-02 c Length m                   1.2202E-03 C |U|    m^3/s
 3.4000E-04 d y0     m                  -0.91343    D Ph(U)  deg
 -232.9     e HeatIn W        G          -100.64    E Htot   W
     0.0000 f SolidT K                    116.40    F Edot   W
     0.0000 g FracQN                      300.07    G GasT   K
                                          235.55    H SolidT K
ideal           Solid type               -100.64    I H2k    W
!-------------------------------- 12 --------------------------------
DUCT       Regen cold end dead space due to ribs (pg 91 book 3)
 3.0000E-04 a Area   m^2      Mstr       1.9095E+05 A |p|    Pa
 6.1410E-02 b Perim  m        12a          -3.3745  B Ph(p)  deg
 1.7500E-03 c Length m                   1.2189E-03 C |U|    m^3/s
                                           -3.2006  D Ph(U)  deg
                                         -100.64    E Htot   W
stainless           Solid type            116.38    F Edot   W
!-------------------------------- 13 --------------------------------
STKSCREEN  Regenerator (pg 92 book 3) (Ks frac est:pg 20 book 4)
 3.5500E-04 a Area   m^2                 1.2753E+05 A |p|    Pa
    0.6800  b VolPor                        9.1551  B Ph(p)  deg
 3.7500E-02 c Length m                   3.6692E-03 C |U|    m^3/s
 6.7512E-05 d rh     m                    -34.537   D Ph(U)  deg
    0.3000  e ksFrac                     -100.64    E Htot   W
                                          169.17    F Edot   W
                                          300.07    G TBeg   K
                                          812.94    H TEnd   K
stainless           Solid type           -100.64    I H2k    W
```

```
!--------------------------------- 14 ---------------------------------
DUCT       All regen hot end dead space (pg 92 book 3)(area is avg)
 3.0000E-04 a Area   m^2      Mstr       1.2740E+05 A |p|    Pa
 6.1398E-02 b Perim  m        14a           9.0999  B Ph(p)  deg
 7.0000E-03 c Length m                   3.7598E-03 C |U|    m^3/s
                                          -36.004   D Ph(U)  deg
                                         -100.64    E Htot   W
stainless           Solid type            169.05    F Edot   W
!--------------------------------- 15 ---------------------------------
HX         HHX (pg 93 book 4) heat xfer area used/not acoustic area
 3.0000E-04 a Area   m^2                 1.2473E+05 A |p|    Pa
    0.6700  b GasA/A                        9.1257  B Ph(p)  deg
 4.2000E-02 c Length m                   4.1979E-03 C |U|    m^3/s
 3.4000E-04 d y0     m                    -43.142   D Ph(U)  deg
  301.00    e HeatIn W        OP          200.36    E Htot   W
     0.0000 f SolidT K                    160.22    F Edot   W
     0.0000 g FracQN                      812.94    G GasT   K
                                          848.15    H SolidT K
stainless           Solid type            200.36    I H2k    W
!--------------------------------- 16 ---------------------------------
DUCT       hhx dead space (pg 94 book 3) stainless used for Qdot
 3.0000E-04 a Area   m^2      Mstr       1.2471E+05 A |p|    Pa
 6.1419E-02 b Perim  m        16a           9.1180  B Ph(p)  deg
 1.0000E-03 c Length m                   4.2123E-03 C |U|    m^3/s
                                          -43.297   D Ph(U)  deg
                                          200.36    E Htot   W
stainless           Solid type            160.20    F Edot   W
!--------------------------------- 17 ---------------------------------
STKDUCT    Straight section of pulse tube (pg 101 bk 4)
 3.5000E-04 a Area   m^2      Mstr       1.2200E+05 A |p|    Pa
 6.6336E-02 b Perim  m        17a           8.3554  B Ph(p)  deg
 7.0000E-02 c Length m                   5.3972E-03 C |U|    m^3/s
 6.4500E-05 d WallA  m^2                  -52.505   D Ph(U)  deg
                                          200.36    E Htot   W
                                          160.31    F Edot   W
                                          812.94    G TBeg   K
                                          300.07    H TEnd   K
stainless           Solid type            200.36    I H2k    W
!--------------------------------- 18 ---------------------------------
RPN        how much heat must be rejected here? Resonator is insulated
     0.0000 a G or T                    1182.5                     A ChngeMe
15e -1483.50565298 + ~
```

```
!-------------------------------- 19 --------------------------------
HX Change Me
 3.0000E-04 a Area   m^2                1.1785E+05 A |p|    Pa
    0.6700  b GasA/A                      7.7353  B Ph(p)  deg
 2.5000E-02 c Length m                  5.6621E-03 C |U|    m^3/s
 2.5000E-04 d y0     m                   -54.273  D Ph(U)  deg
  -75.00    e HeatIn W                   125.36   E Htot   W
     0.0000 f SolidT K                   156.59   F Edot   W
     0.0000 g FracQN                     300.07   G GasT   K
                                         286.06   H SolidT K
ideal           Solid type               125.36   I H2k    W
!-------------------------------- 20 --------------------------------
DUCT       PT connector (see pg 55 book 4 and concept.skf)
 3.0000E-04 a Area   m^2      Mstr      1.1188E+05 A |p|    Pa
 6.1414E-02 b Perim  m        20a         6.2867  B Ph(p)  deg
 6.0000E-02 c Length m                  6.5598E-03 C |U|    m^3/s
                                         -58.523  D Ph(U)  deg
                                         125.36   E Htot   W
stainless           Solid type           156.18   F Edot   W
!-------------------------------- 21 --------------------------------
UNION      Rejoin
  7         a SegNum                    1.1188E+05 A |p|    Pa
 6.0649E+04 b |p|Sft Pa       =21A        6.2867  B Ph(p)  deg
    7.7486  c Ph(p)S deg      =21B      2.0330E-02 C |U|    m^3/s
  300.07    d TSoft  K        =21G       -82.911  D Ph(U)  deg
-0.80185    e p20HLS Pa       =21H        -6.9023  E Htot   W
     0.0000 f nLSoft                      15.925  F Edot   W
                                         300.07   G T      K
                                       -0.32112   H p20HL  Pa
                                           0.0000 I nL
!-------------------------------- 22 --------------------------------
DUCT       Initial section of resonator
 3.0000E-04 a Area   m^2      Mstr      8.5453E+04 A |p|    Pa
 6.1419E-02 b Perim  m        22a         6.1984  B Ph(p)  deg
 7.0000E-02 c Length m                  2.1337E-02 C |U|    m^3/s
                                         -82.961  D Ph(U)  deg
                                          -6.9023  E Htot   W
stainless           Solid type            13.368  F Edot   W
!-------------------------------- 23 --------------------------------
DUCT       Continuation of resonator
 3.0000E-04 a Area   m^2      Mstr      1.5419E+04 A |p|    Pa
 6.1416E-02 b Perim  m        23a       -171.87   B Ph(p)  deg
    0.2500  c Length m                  2.2631E-02 C |U|    m^3/s
                                         -83.048  D Ph(U)  deg
                                          -6.9023  E Htot   W
stainless           Solid type             3.5989  F Edot   W
```

DeltaEC Code Continued

```
!-------------------------------- 24 --------------------------------
CONE       7 degree cone - 10.02" final diameter
 3.0000E-04 a AreaI  m^2      Mstr       5.2878E+04 A |p|    Pa
 6.1417E-02 b PerimI m        24a        -172.95    B Ph(p)  deg
    0.2500  c Length m                   1.6958E-02 C |U|    m^3/s
 2.0300E-03 d AreaF  m^2      Mstr        -83.063   D Ph(U)  deg
    0.15971 e PerimF m        24d          -6.9023  E Htot   W
stainless           Solid type              0.88259 F Edot   W
!-------------------------------- 25 --------------------------------
DUCT       10" duct                     P8
 2.0300E-03 a Area   m^2      Mstr       5.9783E+04 A |p|    Pa
    0.15971 b Perim  m        25a        -172.99    B Ph(p)  deg
    0.3000  c Length m                   1.8595E-14 C |U|    m^3/s
                                           -4.3972  D Ph(U)  deg
                                           -6.9023  E Htot   W
stainless           Solid type          -5.4485E-10 F Edot   W
!-------------------------------- 26 --------------------------------
IEDUCER Change Me
     0.0000 a Re(Ze) ohms                5.9783E+04 A |p|    Pa
-4.0000E+04 b Im(Ze) ohms                -172.99    B Ph(p)  deg
     0.0000 c Re(T1) V-s/m^3             1.8595E-14 C |U|    m^3/s
 1.2600E+06 d Im(T1) V-s/m^3               -4.3972  D Ph(U)  deg
     0.0000 e Re(T2) Pa/A                  -6.9023  E Htot   W
 1.1000E+05 f Im(T2) Pa/A               -5.4485E-10 F Edot   W
     0.0000 g Re(Zm) Pa-s/m^3           -9.2515E-15 G WorkIn W
 4.0058E+08 h Im(Zm) Pa-s/m^3               0.4120  H Volts  V
 1.0300E-05 i |I|    A        IP         1.0300E-05 I Amps   A
     0.0000 j Ph(I)  deg                  -90.00    J Ph(Ze) deg
                                            1.1330  K |Px|   Pa
                                           90.000   L Ph(Px) deg
!-------------------------------- 27 --------------------------------
HARDEND    end of duct
     0.0000 a R(1/z)          =27G       5.9783E+04 A |p|    Pa
     0.0000 b I(1/z)          =27H       -172.99    B Ph(p)  deg
     0.0000 c Htot   W                   1.8595E-14 C |U|    m^3/s
     0.0000 d Ndot   mol/s                 -4.3972  D Ph(U)  deg
                                           -6.9023  E Htot   W
                                        -5.4485E-10 F Edot   W
                                        -5.0104E-13 G R(1/z)
                                         1.0113E-13 H I(1/z)
                                             0.0000 I Ndot   mol/s
```

DeltaEC Code Continued

```
! The restart information below was generated by a previous run
! and will be used by DeltaEC the next time it opens this file.
guessz   0b   0d   1a   1b   9a  11e
xprecn  1.9504E-05    -1.8686    357.16      167.49
   4.3719E-10 -2.3176E-03
targs   21b  21c  21d  21e  27a  27b
mstr-slave 16 2 -2 3 -9 4 -2 5 -9 6 -2 8 -2 10 -2 12 -2
14 -2 16 -2 17 -2 20 -2 22 -2 23 -2 24 -9 25 -2
! Plot start, end, and step values.  May be edited if you wish.
! Outer Loop:                     | Inner Loop .
pltvar  15e  26i  0b   0d   1a   1b   9a  11e
  354.7     301 -0.02685       0 1.03e-005 1.1444e-006
```

Table 6.1: Code used by DeltaEC to analyze TWTAE

User-Defined gas code used by DeltaEC

```
! m_helium(kg/mole) m_air(kg/mole) gamma_helium gamma_air:
0.004 28.97e-3 1.6667 1.4
! k pure helium (W/m-K):
0. 0. 0. 0. 0. .0025672 0.716
! k pure air (W/m-K):
0. 0. 0. 0. 0. 5.0499e-6 1.5
! mu pure helium (kg/m-s):
0. 0. 0. 0. 0. 0.412e-6 0.68014
! mu pure air (kg/m-s):
0. 0. 0. 0. 0. 3.5526e-9 1.5
! k mixture (W/m-K):
0.
! mu mixture (kg/m-s):
0.
! D12 (m2/s):
0.53E-4 0. 1.72
! kT:
0.0267 1.0 1.0
```

Table 6.2: User defined gas code used by DeltaEC

6.2 DeltaEC Results

Fig. 6.3 displays the performance characteristics of the TWTAE prototype as predicted by the DeltaEC software.

The figure shows the effect of the input thermal heat in watts on the pressure amplitude (labeled (a) in Fig. 6.3), temperature (labeled (b) in Fig. 6.3), frequency of self-sustained oscillation (labeled (c) in Fig. 6.3), and volume flow rate (labeled (d) in Fig. 6.3).

Comparisons between DeltaEC predictions and the predictions of the lumped-parameter model as well as the experimental results are reported in Chapter 8.

6.3 Summary

This chapter has presented a model of the experimental prototype of the TWTAE using DeltaEC software.

The predictions of the basic performance characteristics of the experimental prototype are determined for different levels of input thermal power that induce self-sustained oscillations.

These predictions will be evaluated against the predictions of the lumped-parameter model and against the experimental results in Chapter 8.

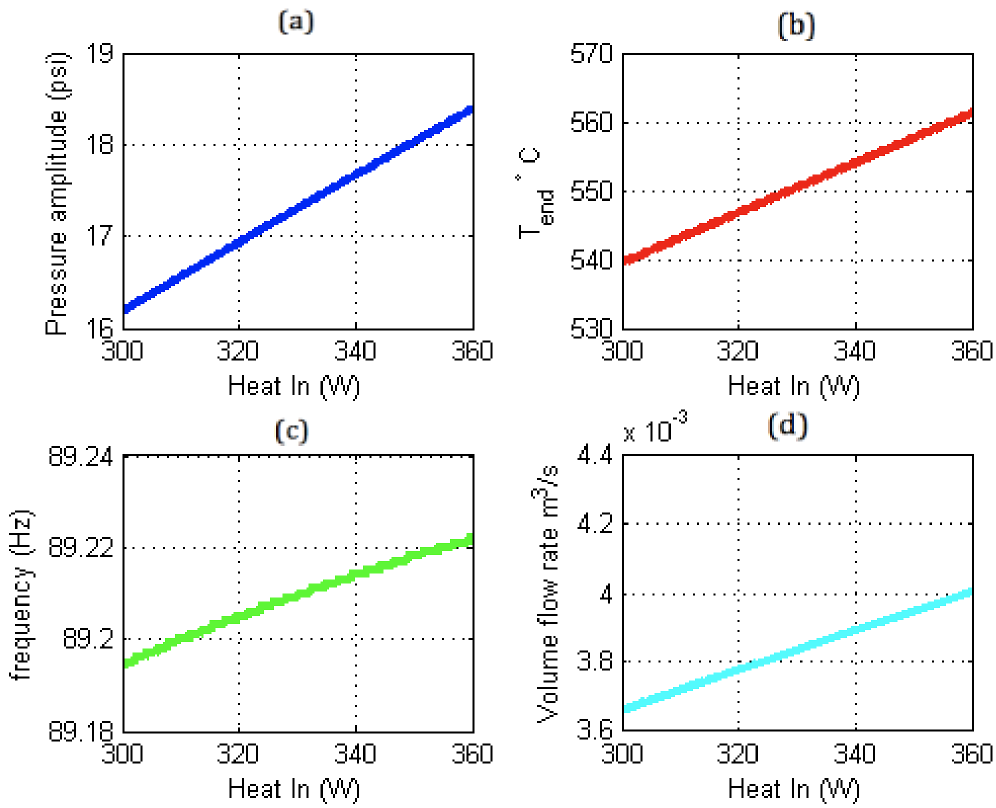

Figure 6.3: Results of the DeltaEC simulation displaying pressure amplitude (a), Hot-end temperature (b, pressure oscillation frequency and volume flow rate through the regenerator (d) as each varies according to input power.

Chapter 7

Experimental Setup

7.1 Traveling wave thermoacoustic engine construction

The experimental set up constructed by D. Sun et. al. in 2004 possesses many similarities to the prototype of the TWTAE constructed at the Smart Systems Laboratory at the University of Maryland (UMD). The design also has similar components as those described by Backhaus and Swift in 1999. The design includes a feedback loop with an inertance, and a buffer tube with an ambient or cold temperature heat exchangers bracketing the hot heat exchanger. The heat source for the UMD prototype TWTAE are four heating cartridges at the hot heat exchanger location, similar to D. Sun's set up. The ambient heat exchanger uses water to remove heat from the engine. The schematic drawing of the UMD prototype can be seen in Fig. 7.1 and Fig. 7.2.

Fig. 7.1 shows the torus section of the UMD TWTAE. The regenerator section is shown in Fig. 7.2. Dimensions and parts are labelled in the figures. The engine design is several times smaller than other realizations which are discussed in the literature review in Chapter 2. After heating, the engine creates pressure oscillations and is acceptable in terms of performing experimental verification of theoretical analyses.

An image of the actual construction can be seen in Fig. 7.3. Some notable

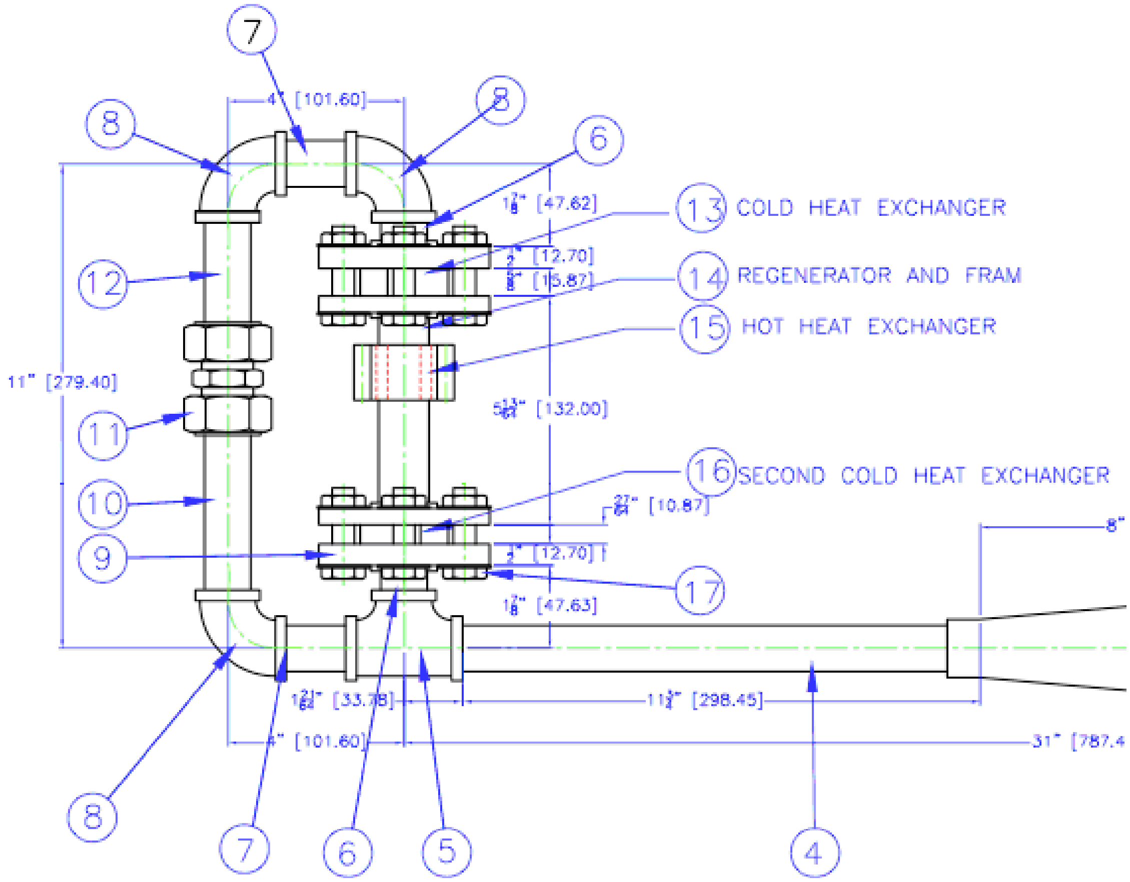

Figure 7.1: Schematic drawing for the UMD traveling wave thermoacoustic engine, torus section.

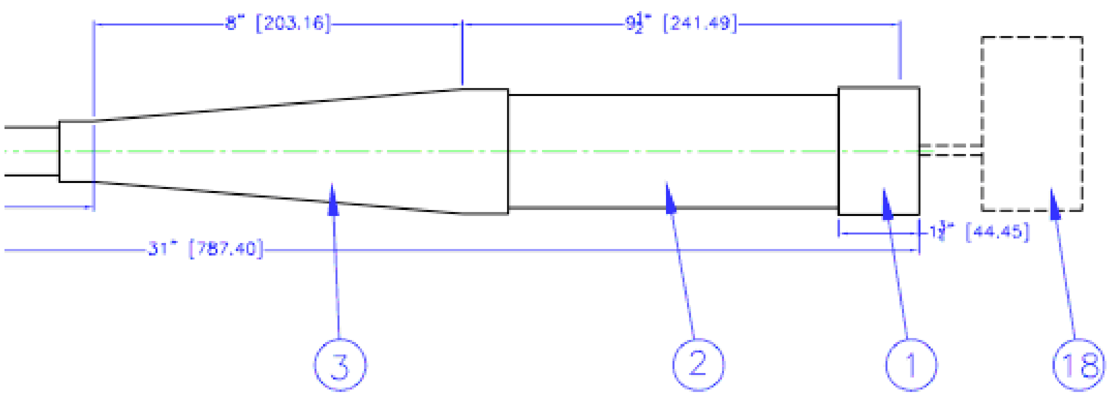

Figure 7.2: Schematic drawing for the UMD traveling wave thermoacoustic engine; resonator.

aspects include the transparent plastic resonator to the right of the figure. The plastic tubing used for the cold heat exchangers are also visible. Not shown in the image is the location behind the resonator used to pressurize the engine to approximately 100psi.

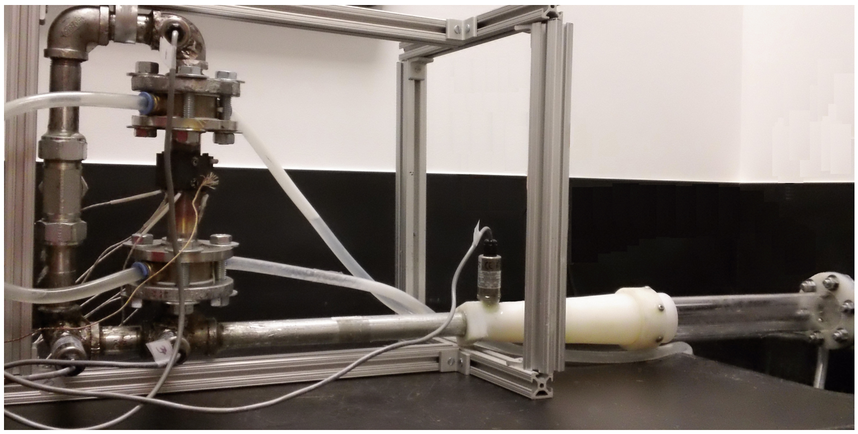

Figure 7.3: Physical realization of traveling wave thermoacoustic engine.

The components of the engine, shown in Fig. 7.3 are more properly labelled for the analyses performed in Chapter 3 and Chapter 4 in Fig. 7.4.

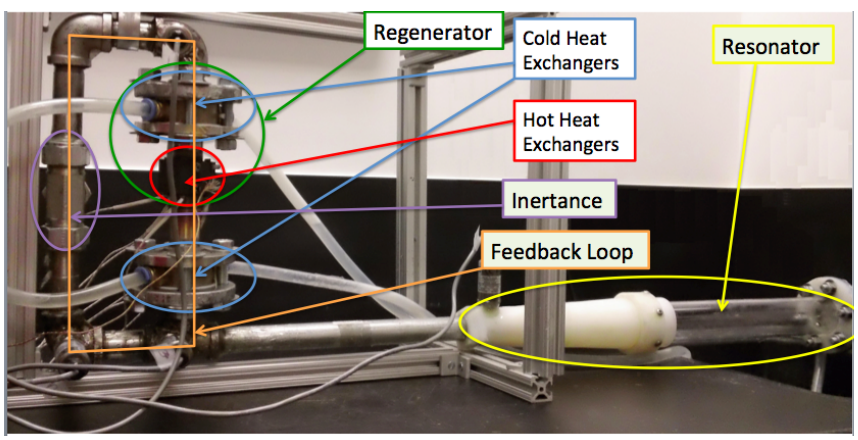

Figure 7.4: Labeling of the TWTAE to correspond to theoretical analyses.

Two components of the engine are isolated for inspection. Fig. 7.5 shows the ambient heat exchanger used in the engine. The ambient heat exchanger is made of copper and has laser-etched grooves in the center of the disc which allow air to pass through. The copper between the channels acts as a heat sink for the air. This heat is then removed from the heat exchanger by cold water running through an inner channel separate from the laser etched channel. The hole allowing water through the cold heat exchanger is visible in the outer surface of the heat exchanger.

Figure 7.5: Closeup of ambient heat exchanger. There are two cold heat exchangers in this engine.

Fig. 7.6 shows the stacked screen cylinder used in the regenerator. The regenerator requires a porous medium with high thermal conductivity characteristics in order to create the temperature gradient necessary for thermoacoustic oscillations. Some engines use steel wool for this material, for example. This engine uses a hollow cylinder filled with steel meshes cut into circles stacked on top of one another. Three of the screens are taken out for inspection and are seen below the cylinder in Fig. 7.6.

Fig. 7.5 shows the ambient heat exchanger used in the regenerator. The hot-

Figure 7.6: Closeup of the stack screen, the most important component of the the regenerator.

heat exchanger is wrapped around the hot end of the regenerator and is powered using four resistance heater cartridges. These are powered in parallel from the AC wall outlet. The resistance across the heater cartridges mounted in parallel was measured to be $R = 20.3\Omega$. The maximum voltage that the wall outlet is capable of providing is 120V. Because AC power is supplied, the root mean squared voltage (V_{RMS}) is calculated by dividing the supplied AC voltage by $\sqrt{2}$. The maximum power supplied to the engine is then calculated as follows:

$$\begin{aligned} P_{max} &= \frac{V_{RMS}^2}{R} = \frac{(120V)^2}{2 \cdot 20.3\Omega} \\ &= 354.7W \end{aligned} \tag{7.1}$$

The power that is supplied to the engine can be adjusted as a percentage of this maximum value using a VariAC. This VariAC can be seen in Fig. 7.8 as the red box with the black dial sitting to the left of the TWTAE.

7.2 Pressure and Piezo-Voltage Experimental Setup

In Chapter 3, the lumped-parameter model is used to create plots demonstrating the transient pressure and temperature versus time for the UMD TWTAE. Chapter 6 also has utilized DeltaEC to numerically predict these plots. The experimental setup described in this chapter is used to verify these figures. The pressure and piezo output voltages are measured using pressure transducers and a $1.25in$ diameter piezo-electric disc attached to the end of the resonator. Simultaneously, the temperature of the hot heat exchanger was measured using a thermocouple. The placement of these sensors attached to the TWTAE can be seen in Fig. 7.7.

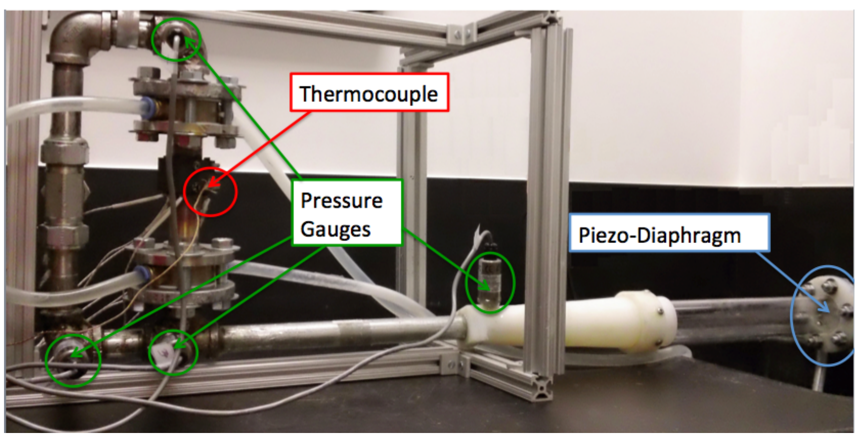

Figure 7.7: Locations of sensors attached to TWTAE.

Outputs from all the sensors of this experimental setup can be seen in Chapter 8. Chapter 8 compares the hot heat exchanger pressure and temperature responses due to changing power inputs.

7.3 Modal Characteristics of the Composite Piezo Disc System

From Chapter 5, the resonant frequency of the composite piezo disc is theoretically determined from the developed axisymmetric FEM. Fig. 5.3, displays the frequency response of the disc modeled by two finite elements as described in that chapter. This was compared with the outputs from ANSYS as shown in Fig. 5.6. Table 5.1 tabulates the natural frequencies from two experimental methods, and compares those values with the corresponding theoretical values. The experimental values were determined from FFT response to a white noise input, and also from the output of a scanning laser vibrometer. The setup for these experiments are seen in Fig 7.8.

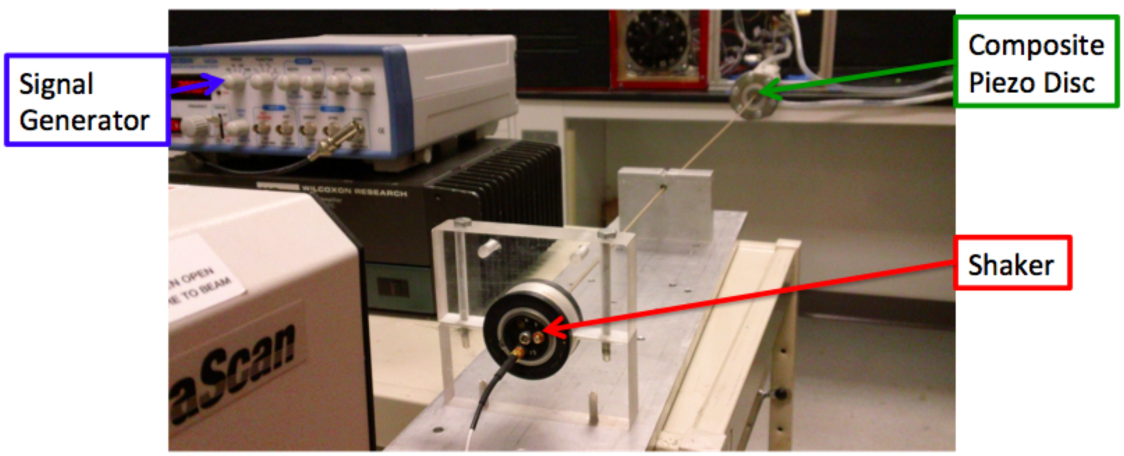

Figure 7.8: Setup of disc natural frequency experiment.

A soft plastic stinger connects the end of the shaker to the center of the disc sitting at the end of the TWTAE. For the white noise response experiment, the shaker is provided a white noise input from an analyzer, and then FFT is performed on the voltage output from the piezo disc. The frequency plot for this can be seen in Fig. 5.7.

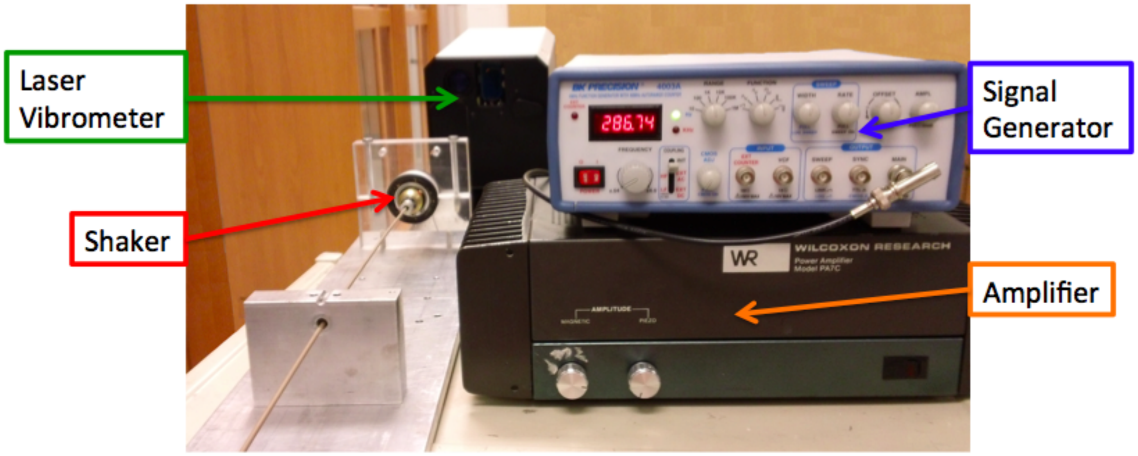

Figure 7.9: Reverse view of Fig. 7.8, orientation of laser vibrometer (located behind shaker with stinger attached) is seen.

Fig. 7.9 shows the reverse view of Fig. 7.8. Seen here is the relative position of the laser vibrometer to the shaker which excites the composite piezo disc system. The location on the piezo-disc where the stinger is attached is seen in Fig. 7.10. Also seen in this figure are the wires which connect to the electrodes of the piezo disc from which the voltage is measured.

The laser vibrometer uses a camera to create a mesh on the surface of the piezo discwhose velocity or displacement amplitude is to be measured. The laser vibrometer then at each point in the mesh captures the displacement and velocity profile vs. time and creates a contour plot of the amplitude. A screen capture of the contour plot is seen in Fig. 5.5.

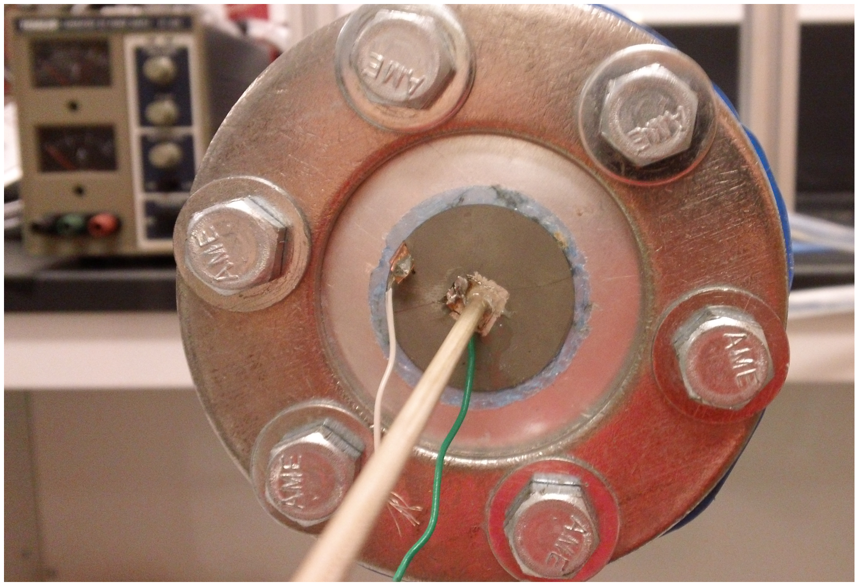

Figure 7.10: Closeup of the stinger attachment to the center of the piezo disc system.

7.4 Summary

This chapter has presented the detailed design features of the UMD experimental prototype of the TWTAE. Also included in this chapter is the instrumentation utilized to monitor the system performance.

Chapter 8

Results

8.1 Pressure Transducer, Piezo Voltage and Thermocouple Plots

This chapter displays the results of the experimental setup described in Section 7.2. The experiments aim at validating the theoretical predictions generated in Chapter 3. Recall from Chapter 3 that an important component to Fig. 3.9 and Fig. 3.10 was the oscillating nature of the pressure amplitude and regenerator hot-end temperature. The theory is that there is some threshold temperature at which the pressure oscillations begin in the engine, but then the action of oscillation causes the heat to fall due to enthalpy. The results of this chapter attempt to verify or disprove this theory. Beginning by determining the frequency of the oscillations and the noise from the sensors, Fig. 8.1 displays the FFT of the voltage output from the pressure transducers when the engine experiences an input power of 354.7W. This is the maximum amount of power that the can be supplied to the engine according to Eq. 7.1.

As can be seen from the voltage output of the pressure transducers in the frequency domain, there is a strong peak at $60Hz$, the frequency of the AC current supplied from the electrical outlets. The next peak is at 91.64Hz, corresponding to the first mode frequency at which the TWTAE oscillates. This frequency is verified in Fig. 8.2. Other peaks seen in the figure are multiples of the 60Hz.

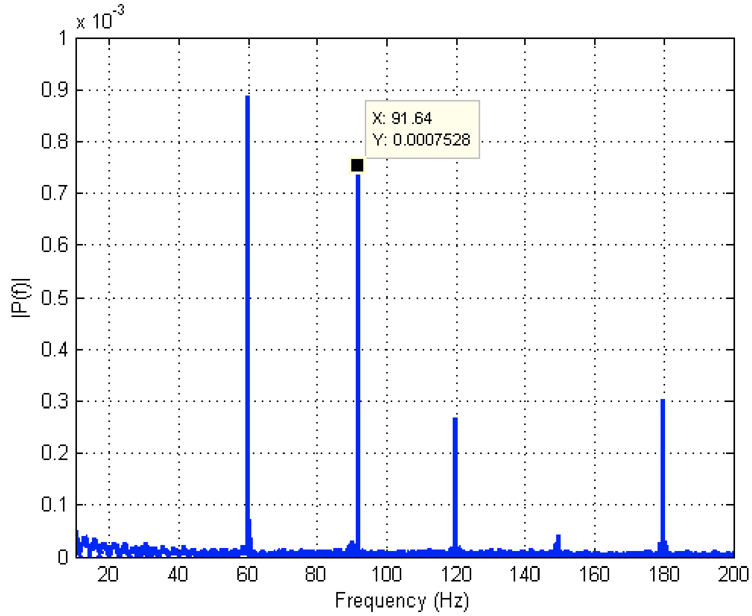

Figure 8.1: FFT of unfiltered pressure data for $P_{avg} = 354.7W$ input power.

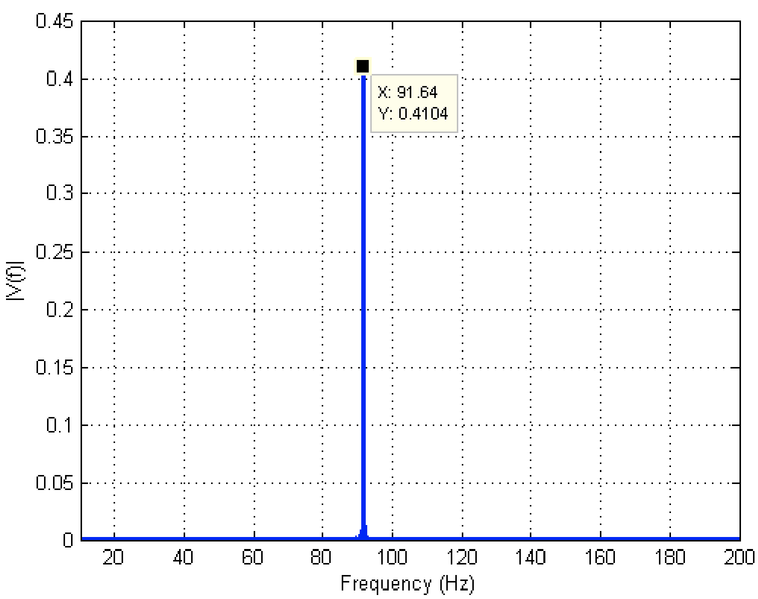

Figure 8.2: FFT of unfiltered piezo data for $P_{avg} = 354.7W$ input power.

Fig. 8.2 shows the frequency domain voltage output of the piezo disc attached to the end of the TWTAE resonator. The piezo disc output is not affected by noise from AC power lines and as a result, only the 91.64Hz peak of theTWTAE oscillations are seen. The noise from the AC power lines seen in Fig. 8.1, the peaks at multiples of 60Hz, require the pressure measurements to be filtered with a software bandpass filter from the LabVIEW library. Even so, the measurements are noticeably noisy.

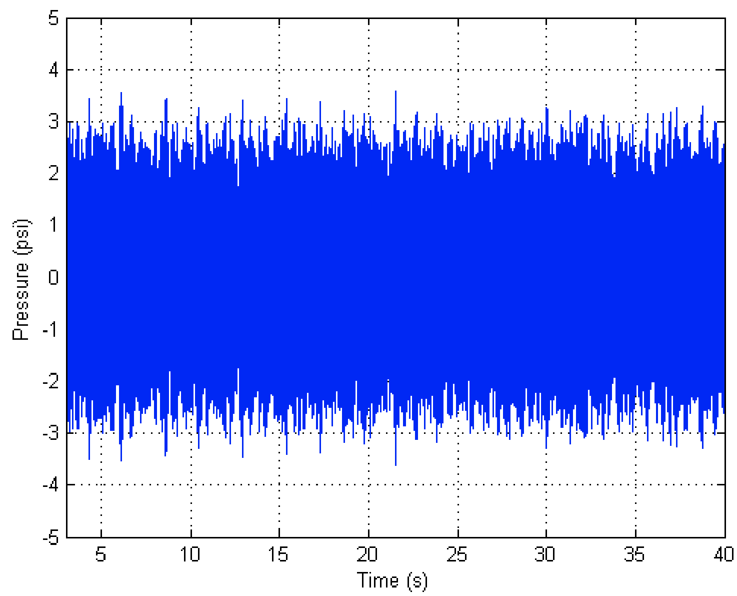

Figure 8.3: Pressure vs. time for $P_{avg} = 354.7W$ input power.

Because the pressure oscillations are sinusoidal, the signal can be more easily interpreted by time averaging multiple local maximums (peaks) together in order to get an idea of the system amplitude as it changes with time. Fig. 8.3 shows the bandpass filtered pressure transducer output across time. Fig. 8.4 shows the pressure output amplitude of Fig. 8.3 in psi by averaging 20 peaks. The pressure transducers read an oscillating amplitude about the mean pressure of about 2.4 psi.

Fig. 8.5 show the peak averaged amplitude plot of the piezo voltage output

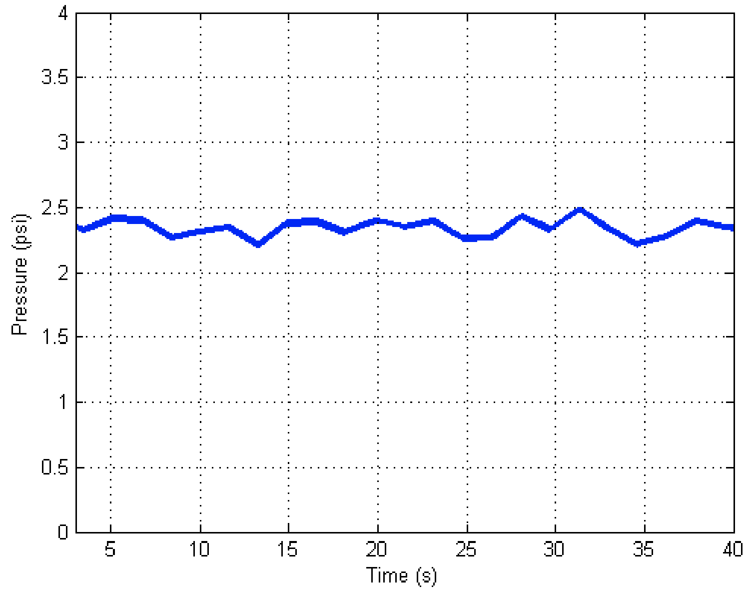

Figure 8.4: Pressure amplitude vs. time for $P_{avg} = 354.7W$ input power.

for a maximum power input (354.7W). The plot continues to rise slightly over the 40 seconds pictured. Presumably this means the system has not yet reached steady state and that as the temperature continued to rise, so would the amplitude of the pressure and voltage oscillations. Even without a load resistor across the electrodes of the piezo disc, the amplitude of the output voltage was slightly higher than 0.4V. As can be seen Fig. 8.5 and in Fig. 8.6, which shows 9 periods of piezo voltage oscillation, the output of the piezo disc is not encumbered by noise.

After demonstrating that the maximum amount of output power results in stable oscillations, the next plots attempt to find the power setting which causes the temperature in the hot end of the heat exchanger to hover about the threshold temperature. This threshold temperature will presumably cause the pressure measured in the system to begin oscillating, and as the theory purported in Chapter 3,

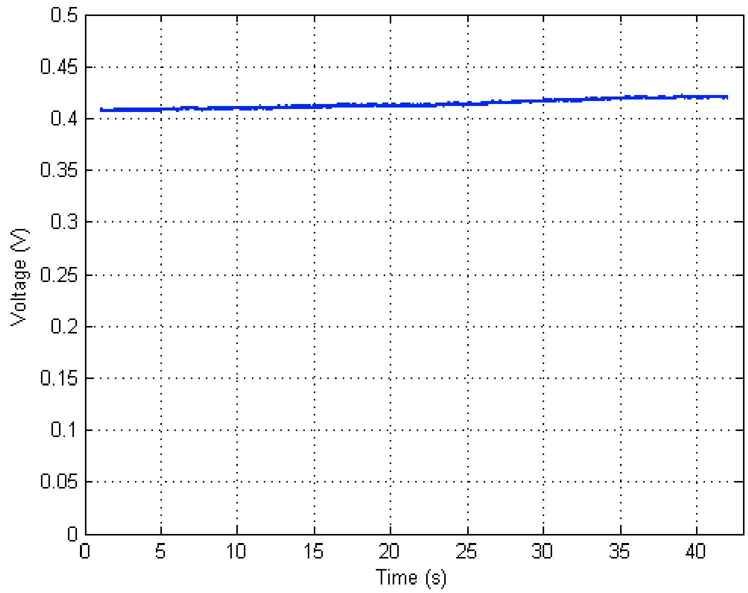

Figure 8.5: Piezo voltage amplitude vs. time for $P_{avg} = 354.7W$ input power.

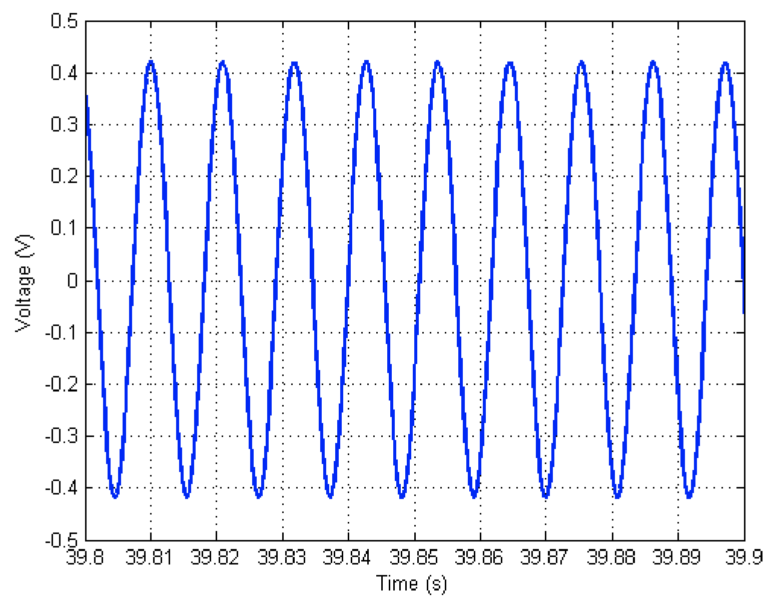

Figure 8.6: Piezo voltage vs. time oscillations over 9 periods for $P_{avg} = 354.7W$ input power.

stop oscillating as the temperature decreases due to enthalpy and once again begin oscillating due to temperature increase. Fig. 8.7 and Fig. 8.8 shows the bandpass filtered and peak averaged amplitude of the pressure transducer output, respectively, of the TWTAE with the power input at 85% of the maximum (301.5W). The engine was oscillating at that point when the power input was dropped abruptly to 85% of its maximum. These plots show the pressure output as the oscillations die out.

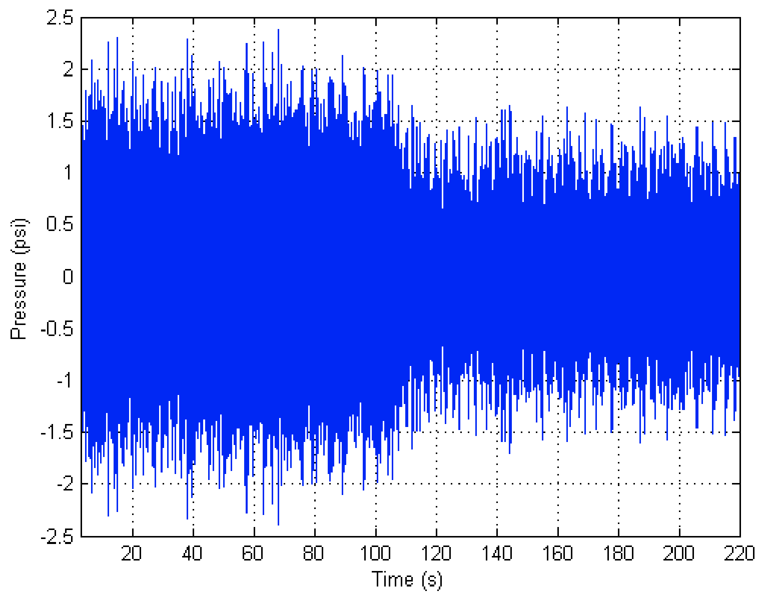

Figure 8.7: Pressure vs. time for $P_{avg} = 301.5W$ input power.

The peak averaged piezo output voltage for an input power of 301.5W can be seen in Fig. 8.9. Note that although Fig. 8.8 still reads a positive pressure amplitude after the drop off, Fig. 8.9 shows that oscillation have clearly died. The theory indicates that the amplitudes for all three figures, Fig. 8.7, Fig. 8.8, and Fig. 8.9, should all increase as the temperature rises. It can be seen in Fig. 8.9 and Fig. 8.8 that the amplitude of the piezo voltage and pressure does not rise again, indicating that this power input is too low to restart oscillations.

At 90% of the maximum power input to the engine, 319.2W, there is sufficient

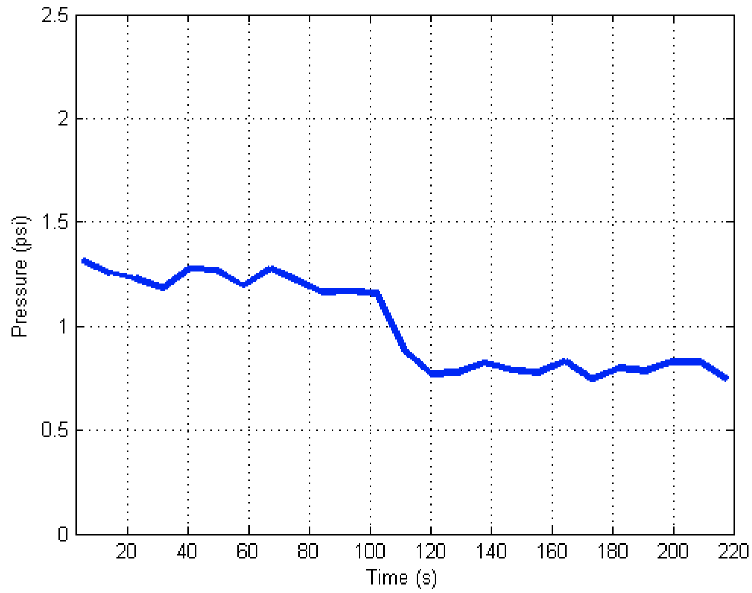

Figure 8.8: Pressure amplitude vs. time for $P_{avg} = 301.5W$ input power.

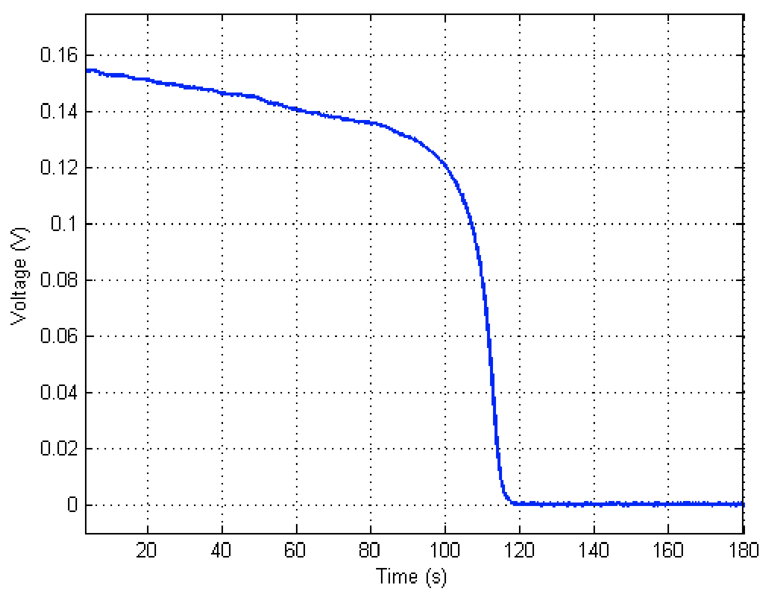

Figure 8.9: Piezo voltage amplitude vs. time for $P_{avg} = 301.5W$ input power.

power to initiate oscillations, as can be seen in the bandpass filtered and peak averaged amplitude of the pressure transducers seen in Fig. 8.10 and Fig. 8.11

respectively. These figures demonstrate that, similar to the plots of the engine operating at 85% of maximum, that the oscillations do not stop and start due to enthalpy, but once the threshold temperature is met the oscillations level toward steady state. Fig. 8.12 shows the peak averaged piezo voltage amplitude for this power setting. Plots for initiating oscillations for power settings below 90% are not shown, for an input power of 319.2W was the minimum determined power setting which would initiate oscillations.

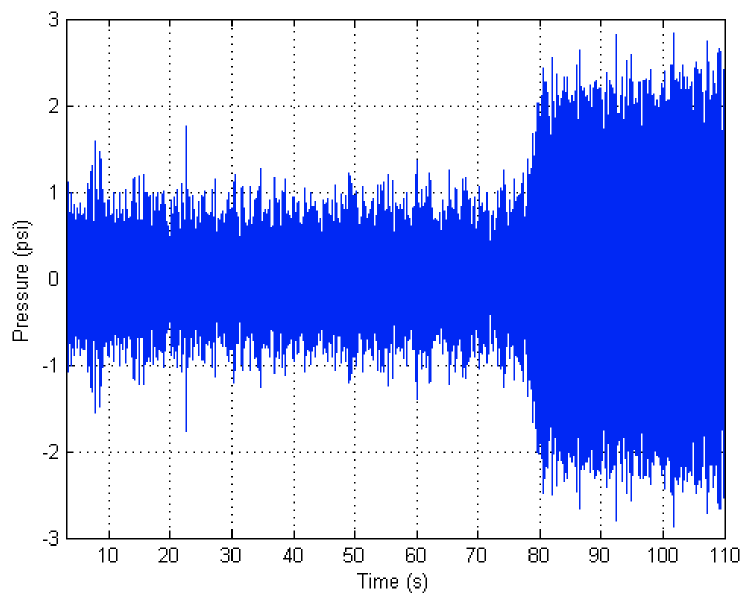

Figure 8.10: Pressure vs. time for $P_{avg} = 319.2W$ input power.

In order to more closely determine the temperature threshold, the temperature output from the hot end of the regenerator is monitored with a thermocouple to determine when steady state is reached in the engine. The following plots show the peak-averaged voltage amplitude of the piezoelectric disc plotted with the thermocouple output. For each of these plots, the oscillations were initiated using the

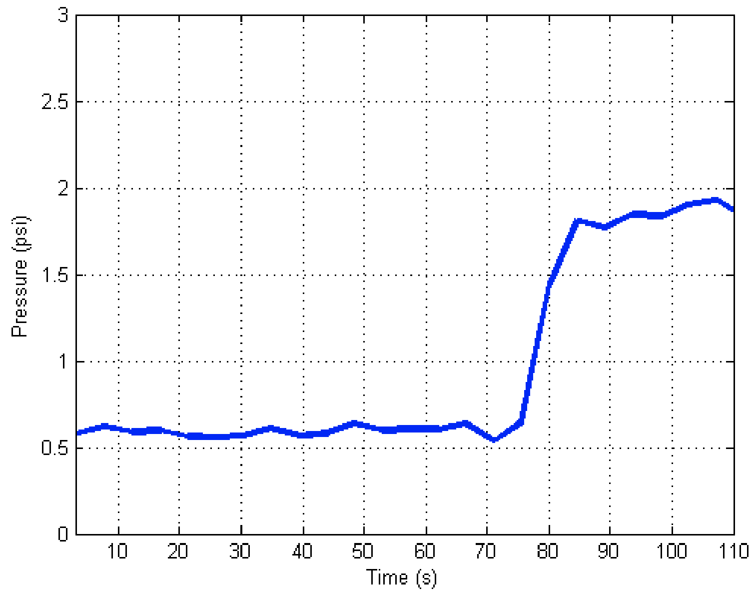

Figure 8.11: Pressure amplitude vs. time for $P_{avg} = 319.2W$ input power.

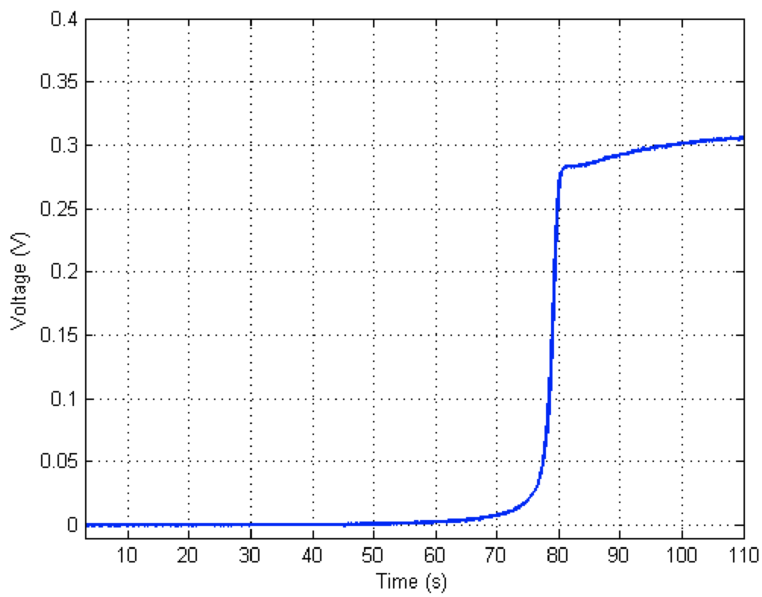

Figure 8.12: Piezo voltage amplitude vs. time for $P_{avg} = 319.2W$ input power.

maximum power input, then the power input was dropped and the system was allowed to reach steady state as determined by the thermocouples. Fig. 8.13 shows the hot-end temperature approaching steady state in conjunction with the piezo voltage output due to power input of 319.2W (90% of maximum). As can be seen in Fig. 8.14, which is a closeup for the system between 800-1100 seconds, between 925 and 1100 seconds both the piezo voltage and the temperature increase. The reason for this temperature increase was due to the air conditioning in the room switching off, and the reduced convection about the engine allowed the temperature to increase. The temperature increase did not occur because the reduced pressure oscillations in the regenerator which in turn caused a reduction in enthalpy.

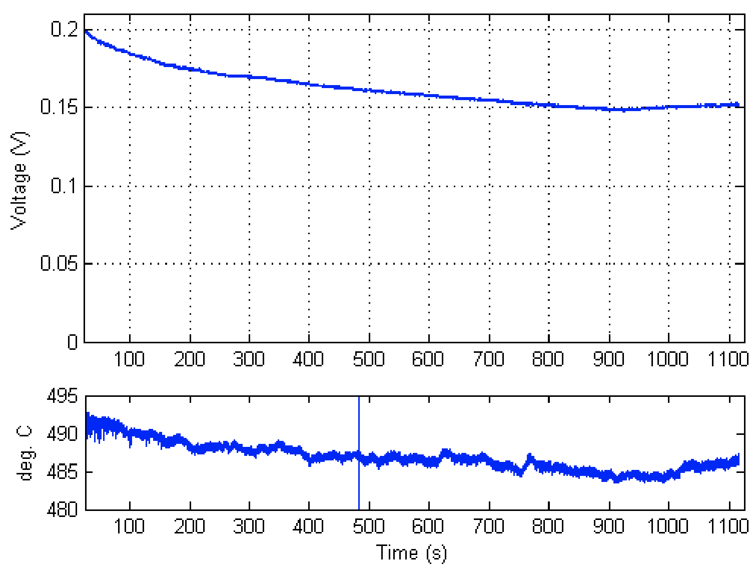

Figure 8.13: Piezo-voltage amplitude and regenerator hot-end temperature vs. time for $P_{avg} = 319.2W$ input power.

Because the engine was capable of maintaining pressure oscillations at steady state due to a power input of 319.2W, the input power was then reduced to 312.1W. The next 20 minutes saw the piezo voltage amplitude and hot end temperature dropping steadily, but oscillations were maintained. Fig. 8.15 represents this situation.

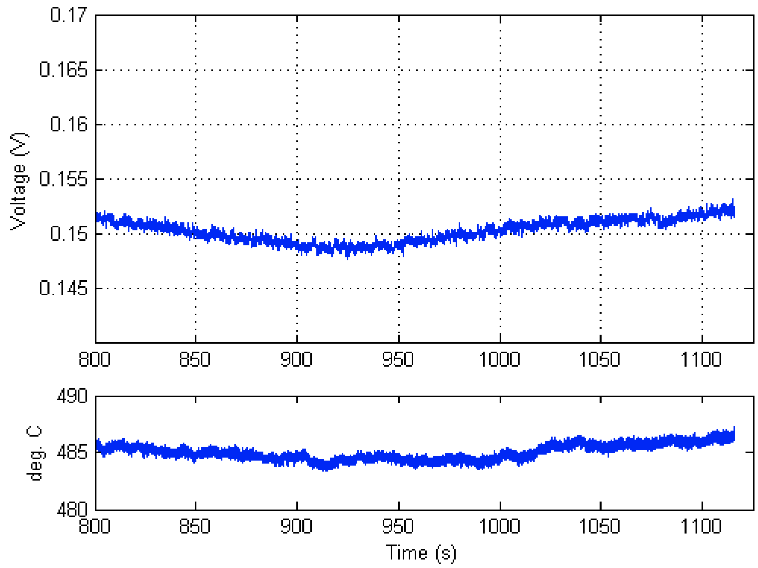

Figure 8.14: Close-up piezo-voltage amplitude and regenerator hot-end temperature vs. time for $P_{avg} = 319.2W$ input power.

As can be seen, at the 1300s mark, the air conditioning unit in the room once again shut off, and the temperature once again began to rise. Fig. 8.16 shows the piezo voltage and temperature plots for an input power of 305.0W. As can be seen, there is insufficient input power to maintain steady oscillations.

The theory discussed in Chapter 3, where enthalpy due to pressure oscillations causes the temperature to drop and therefore oscillation amplitude to die down, which in turn causes the temperature to rise, was not exhibited in the results of the experiments shown in this chapter. As oscillations were maintained and the input power was decreased, leading to a drop in both temperature and oscillations, the only time the temperature began to rise again was due to the air conditioning in the room shutting off during its cycle. The reduction in air movement and cooling within the room caused the temperature to rise within the engine, and also caused the

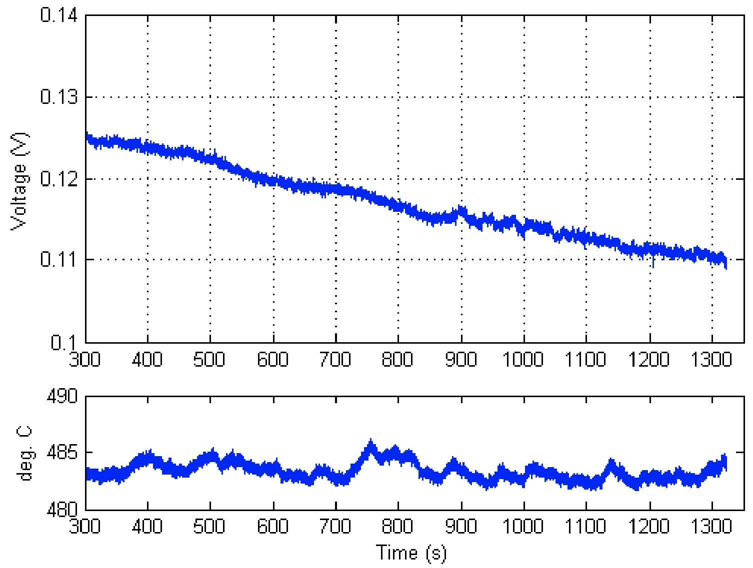

Figure 8.15: Piezo-voltage amplitude and regenerator hot-end temperature vs. time for $P_{avg} = 312.1W$ input power.

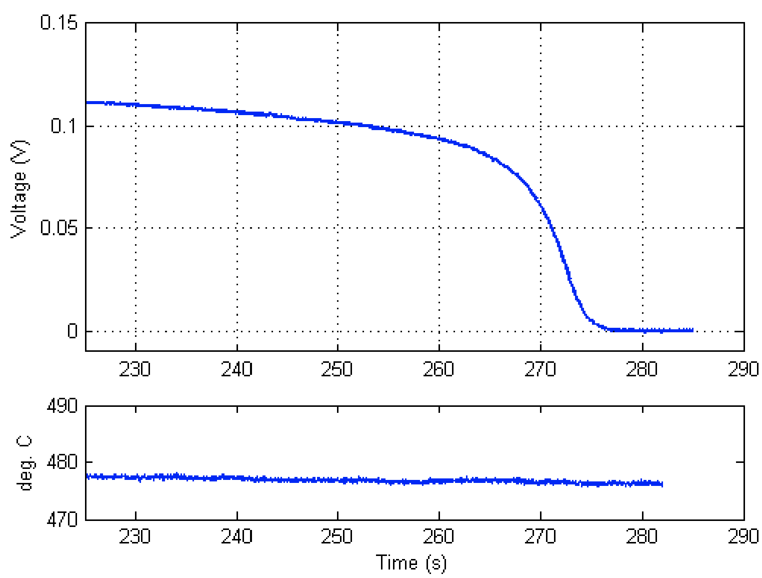

Figure 8.16: Close-up piezo-voltage amplitude and regenerator hot-end temperature vs. time for $P_{avg} = 305.0W$ input power.

oscillation amplitude to rise as well. The theory of a single threshold temperature, one which would cause this inverting rising and falling action of both the pressure oscillation amplitude and the temperature to rise and fall relative to one another, does not appear to be easily found.

A noteworthy observation which resulted from the experiment is the location of the threshold temperature which initiates and ceases oscillation. The lowest discovered input power required for the UMD engine to initiate oscillation was 90% of the maximum, or 319.2W. This was not repeatable and often the power needed to initiate oscillations was 92% of the maximum power input, or 326.3W. This corresponded to a temperature of 487°. Input power below this amount did not seem to be able to initiate oscillations. In the reverse direction, the temperature threshold which ceased pressure oscillations was not the same. With an input power of 312.1W, and a temperature of about 483°, oscillations were able to be maintained at steady state. Instead of having a precise threshold temperature at the brink of pressure oscillations, one which would cause the root locus plot in Fig. 3.4 to move into the right side of the imaginary axis, this observation suggests a range of temperatures within which pressure oscillations cannot be initiated, but can be maintained. This implies that a lower input power is required to maintain pressure oscillations than is necessary to initiate them. There is no theory available to reflect this observation, and developing an analytical model to support this observation is left to future work.

8.2 Experimental and Theoretical Results Comparison

This section will compare the results from the following models: the lumped-parameter model discussed from Chapter 3, the DeltaEC model from Chapter 6, and the experimental results from this chapter. The theoretical and experimental results for the FEM of the aluminum-piezo combination disc is compared in Chapter **??** and will be excluded from this section. Beginning with a comparison of the operating frequency of the TWTAE, Table 8.1 compares the frequency determined from the root locus plot from Fig. 3.3, the DeltaEC output, and the FFT plot from Fig. 8.2.

Lumped-parameter	*DeltaEC*	*Experimental FFT*
269.8 Hz	89.195 Hz	91.64 Hz

Table 8.1: Theoretical and experimental operating frequencies of TWTAE comparing lumped-parameter model, numerical DeltaEC analysis and piezoelectric FFT response.

As can be seen, the numerical DeltaEC analysis gives a very accurate approximation of the operating frequency of the TWTAE. From Fig. 6.3, there is minor change in operating frequency depending on input power (which in turn affects hot-end regenerator temperature), but the change is insignificant over the input power range. Table 8.2 compares the TWTAE oscillating pressure amplitude determined from the theoretical transient response of Fig. 3.9 and Fig. 3.13 , the DeltaEC plots from Fig. 6.3, and experimental results from Fig. 8.4, Fig. 8.8 and Fig. 8.11. Plots for the lumped-parameter model for thermal power inputs of 301.5W and 319.2W are not shown, but the results are indicated in the table.

The lumped-parameter model, from Fig. 3.9, when modeled at 500 W gener-

Input Power	*Lumped-parameter*	*DeltaEC*	*Experiment*
301.5W	8.0 psi	16.25 psi	No Oscillation
319.2W	8.3 psi	17 psi	1.9 psi
354.7W	9.12 psi	18 psi	2.4 psi
500W	11.1 psi	-	-

Table 8.2: Theoretical and experimental oscillating pressure amplitudes of TWTAE comparing lumped-parameter model, numerical DeltaEC analysis and pressure transducer output.

ates a steady state oscillating pressure amplitude of 11.1 psi. At 301.5W heat input, the pressure amplitude is predicted to be 8.0 psi. These values come after a period of oscillations before the pressure amplitude settles around a steady state value. This behavior is not observed in the pressure transducer output. Over the input power range inspected, DeltaEC provides an oscillating pressure corresponding linearly to the power input, but the calculated pressure amplitude is much higher than the measured pressure from the transducers. The reason for this difference could be the effect of noise and improper orientation of the pressure transducers, or perhaps DeltaEC is not accounting appropriately for losses in the TWTAE. A problematic aspect of the DeltaEC model is the inability to analyze a situation where oscillations are not present, unlike the lumped-parameter model. By default, DeltaEC assumes oscillations exist and determines a solution which matches the inputs.

Input Power	*Lumped Capacity*	*DeltaEC*	*Experiment*
305.0W	1030 °C	542 °C	475 °C
312.1W	1030 °C	545 °C	484 °C
319.2W	1030 °C	548 °C	487 °C
500W	1030 °C	-	-

Table 8.3: Theoretical and experimental regenerator hot-end temperature comparing lumped-parameter model, numerical DeltaEC analysis and thermocouple output.

Table 8.3 compares the regenerator hot-end temperature determined from the theoretical transient response of Fig. 3.9, the DeltaEC plots from Fig. 6.3, and Experimental results from Fig. 8.14, Fig. 8.15, and Fig. 8.16. The lumped-parameter model transient plot of Fig. 3.9 shows the hot-end temperature oscillating about and eventually settling to the temperature of 1030 °C, the threshold temperature determined from the root locus plot in Fig. 3.3. This temperature is what is considered the threshold temperature which moves the system from the stable to unstable region of the s-plane in the lumped-parameter model. This value is far above the threshold temperature determined from experimental thermocouple outputs. Additionally, these steady-state values do not change over the range of power inputs suggesting a problem with the lumped-parameter model. The DeltaEC results are approximately 60 °C above the measured temperature. This difference could be due to systematic errors in the thermocouple measuring apparatus. It could be due to thermocouple placement; the thermocouple was placed outside the regenerator, and the internal temperature is hotter.

8.3 Discussion of Experimental Errors

There are several possible sources of experimental errors in the experiments described in Chapter 7. The most obvious source is the noise experienced by the pressure transducers. They noise is clearly affecting the pressure measurements and it is unclear just how great the effect is. Another source of error is potential pressure loss in the TWTAE. Over the course of several hours, due to small leaks in the engine, the equilibrium pressure, p_0, is reduced and will affect pressure and piezo-voltage readings.

As far as temperature readings for this chapter are concerned, because the thermocouples are outside the engine, it is expected that the temperature readings are below the actual value within the regenerator. This could explain the difference between the DeltaEC approximations and the experimental results.

Another source of error that is difficult to quantify is the degradation of the engine through use. Because the regenerator uses such high heat, and the pressure inside the engine is so high, the stacked screens become terrible oxidized while the engine is used. Because it is unclear how degraded the stacked screens are within the enclosed engine, it is very possible that the thermal contact within the regenerator becomes successively reduced every time the TWTAE is used, affecting pressure readings. Furthermore, the piezo discs are also prone to breaking. As can be seen in several plots, while initially the piezo disc provided voltages above $0.4V$ at maximum power input and $0.32V$ for 90% power input, these readings were greatly reduced in subsequent testings. This is possibly due to small fractures which are difficult to detect and affect the voltage readings.

8.4 Summary

This chapter has presented the experimental performance characteristics of a prototype of the TWTAE. The onset of self-sustained oscillations is demonstrated experimentally and the threshold of such oscillations is determined under various scenarios. The experimental threshold agrees closely with the predictions of the DeltaEC model but not with those of the lumped-paramter model.

Similarly the experimental magnitude of the pressure and temperature of the self-sustained oscillation condition match closely with those predicted by the DeltaEC model.

Chapter 9

Conclusions and Future Work

9.1 Overview

This thesis has covered theoretical and numerical methods for analyzing performance characteristics of the traveling wave thermoacoustic engine (TWTAE). In 2009, A.T.A.M. deWaele published a paper proposing a lumped-parameter method for determining the volume flow rate and pressure amplitude of a TWTAE, and also proposes a transient response model in which thermal considerations are included [10]. This thesis has analyzed this lumped-parameter model, and expanded it to an equivalent electrical circuit which represents the TWTAE. This equivalent circuit is capable of incorporating a piezoelectric disc seamlessly. The lumped-parameter model was used to derive analytical values for transient operating properties for oscillating pressure amplitude and frequency, regenerator hot-end temperature, and volume flow rate for a prototype of the TWTAE which was built and tested in the course of this study.

In Chapter 6, this thesis has employed a numerical approach to analyzing the TWTAE. By using DeltaEC [13], properties of the TWTAE were predicted, such as oscillating pressure amplitude, operating frequency, and regenerator hot end temperature. The DeltaEC model included a representation for the composite piezo end cap for the regenerator. This can be seen in the segment `IEDUCER` of the model. To use the `IEDUCER` segment, a 2×2 matrix defining the electromechanical impedance of the composite piezo-disc is required. In order to find the four values of this matrix, an axisymmetric finite element model was developed in Chapter 5. These values can be seen in Eq. 5.117.

In order to validate the predictions of the finite element model, the first mode natural frequency determined from the frequency plot in Fig. 5.3 (1532 Hz), is compared with values determined from excited white noise FFT response in Fig. 5.7 (1220 Hz), laser vibrometer response in Fig. 5.5 ($\sim$1300 Hz), and ANSYS finite element analysis (1250 Hz). From these measurements, it was determined that the ANSYS FEM analysis is a very good approximation of the experimental results, and the two element FEM from Chapter 5 is considered as a first step towards a more accurate model.

Comparisons are made between the lumped-parameter model, the numerical DeltaEC model, and the experimental results. These results are compared in Section 8.2. For the frequency, the lumped-parameter model oscillations are estimated at 269.8Hz, while the DeltaEC model nearly matches the experimental FFT response of the pressure transducer output are determined at 89.195 Hz and 91.64 Hz respectively.

Over the range of input powers analyzed, the pressure amplitude for DeltaEC was related linearly with the input power, ranging between 16.25 psi to 18 psi for input powers between 301.5W and 354.7W. The experiment, on the other hand, measures 2.4 psi pressure amplitude for 354.7W, and no oscillations for an input power of 301.5W. The lumped-parameter model was estimated to settle at approximately

11.6 psi for an input thermal power of 500W. The differences between results could be due to a number of factors, including noisy pressure transducers, imprecision in the DeltaEC model, and estimation errors within the lumped-parameter model. For example, when changing the value for heat capacitance C_H in the lumped-parameter model, the pressure oscillations converge to a lower value. This implies that results could be more closely related to the experimental output with a better estimate of thermal capacity. Another problematic consideration is that the DeltaEC model was unable to account for situations where oscillations were not present.

For regenerator hot-end temperature measurements, the lumped-parameter model estimates the temperature threshold at 1030 °C. Meanwhile for power inputs between 305W and 319.2W, the DeltaEC model estimated hot-end temperatures between 542 °C and 548 °C. From thermocouple readings, for the same power inputs, temperature readings were between 475 and 487 °C. Differences could be due to estimation errors in the DeltaEC model regarding heat losses and temperature distribution, or the external placement of the thermocouples could cause the experimental readings to be cooler than the actual internal temperature of the regenerator. As far as a threshold temperature existing between a quiet engine and pressure oscillations, it was observed that a temperature value of 483 °C was sufficient to maintain pressure oscillations, but a temperature value of 487 °C was required to initiate oscillations. This may be a small enough gap to determine that an exact threshold temperature may exist between these two values, but the control over the input power and environmental conditions is not fine enough to achieve this precise value.

The values for volume flow rate through the regenerator from Fig. 6.3 was approximated to have values between 3.65×10^{-3} and 4×10^{-3} $^{m^3}/_{s}$ corresponding to input powers between 300W and 360W. Meanwhile, from the lumped-parameter model, the volume flow rate through the pulse tube settled at about 0.04 $^{m^3}/_{s}$, or about 10 times the volume flow rate estimated from DeltaEC. The volume flow rate was not determined experimentally, and that process is left to future work.

This thesis analyzes a TWTAE using several theoretical and numerical methods. The lumped-parameter model published by deWaele presents a method for determining transient values for pressure oscillation amplitude and volume flow rate. The generated transient behavior, where the pressure amplitude appears to act like an underdamped second order system where oscillations rise and fall before settling at a steady-state value was not exhibited in the experimental transient plots. It was observed that a precise temperature threshold which explicitly which separates a quiet engine from an oscillating engine, does not appear to exist. It does appear as though a range of temperatures exist which can maintain oscillations but cannot initiate them. There are many potentially identified faults in the lumped-parameter model. It could be that the lumped-parameter assumption, where certain components act exclusively as inertances or compliances break down as the engines size is reduced, as is the case in the UMD TWTAE prototype. Another explanation could be an overexagerated emphasis on the rolls of enthalpy flow rate in the transient response model. If this term were reduced, perhaps the model would behave more like a first order system like the experimental results suggest. Additionally, certain terms in the model are difficult to determine and therefore modeling becomes imprecise.

The DeltaEC model presents excellent results for frequency, but the pressure amplitude and temperature are reported higher than the experimental values. This could be due to a number of approximation errors in the DeltaEC model. The two element FEM model used to model the composite piezo disc is a good first step towards an accurate model, but the estimated frequency is too high. The model is not robust and is too susceptible to small adjustments which greatly affects the frequency plot. The ANSYS model, alternatively, presents a very accurate representation of the first mode natural frequency. This implies that the two element FEM model needs better development and as a result, its representation in the DeltaEC model does not yet give accurate values for piezo-voltage.

9.2 Future Work

There are some aspects of this thesis that can be strengthened or expanded upon. The theoretical outcome of Chapter 3, in which the pressure oscillations in the TWTAE rise and fall in conjunction with the regenerate hot end temperature was not demonstrated experimentally. This implies a potential flaw in the heat transfer modeling, potentially by placing too strong an emphasis on the role of enthalpy. More can be done to strengthen the heat transfer aspects of the lumped-parameter model. The concept of a threshold temperature, a temperature which incites oscillations did not correspond with the temperature which ceases oscillations. The observation, then, is that there exists a range of temperatures in which oscillations can be maintained but not initiated. Theory which demonstrates this observation is not in place and requires a re-evalutaion of the lumped-parameter model. By using the circuit analogy to simplify the process can be done, but incorporating an accurate representation of the piezo disc to estimate output voltages has not yet been performed.

Also from a theoretical standpoint, the finite element model of the composite piezo disc can be made to be more robust, as small changes in thickness and radius values have a large effect on the performance of the finite element model. Furthermore, the finite element model currently employs only 2 elements, and a larger number of elements, such as ANSYS employs, could result in a more accurate representation of the composite piezo disc system.

Further experimental analysis can be performed, such as particle image velocimetry (PIV) of the resonator section, which can confirm the volume flow rate as theorized in Chapter 3. This can be performed in conjunction with sharper filtering processes in order to get a crisper output from the pressure transducers.

Finally, geometric adjustments can be made to the TWTAE in order to match the composite piezo disc with the operating frequency of the engine. Incorporating a load resistor or a shunted network across the electrodes of the piezo disc will also change the impedance properties of the composite piezo disc system. This can be done in conjunction with geometric modifications of the engine so that resonant operant conditions are met.

Appendix A

Derivation of A.T.A.M. deWaele's Equations

This appendix describes in detail the verification of deWaele's equations derived from his lumped-parameter model [10]. Beginning with the assumption that the volumes (d), (t), and (R) are connected by frictionless, isobaric tubes, as seen in Fig. 3.2, it can be said that

$$p_t = p_d = P_R \tag{A.1}$$

Taking the time derivative yields:

$$\frac{dp_t}{dt} = \frac{dp_d}{dt} = \frac{dp_R}{dt} \tag{A.2}$$

As a convention, define:

$$\delta p_t = p_t - p_o \tag{A.3}$$

In Eq. (A.3), p_o is the initial pressure in the system. Also as convention, define:

$$p_r = p_t - p_c \tag{A.4}$$

Therefore p_r can be thought of as the pressure across the inertance piston M_i. As mentioned before, the masses of "pistons" M_i and M_r are defined as the mass of the gas within the column. Therefore:

$$M_i = \rho_0 A_i L_i \tag{A.5}$$

and:

$$M_i = \rho_0 A_i L_i M_i = \rho_0 A_i L_i \tag{A.6}$$

where ρ_0 is the density of air at initial pressure, A_i is the cross sectional area of the inertance, L_i is the length of the inertance. By using Newton's 2$^{\text{nd}}$ law, the acceleration of mass M_i is defined as:

$$M_i \frac{d^2 x_i}{dt^2} = (p_t - p_c)\, A_i = p_r A_i \tag{A.7}$$

In Eq. (A.7) x_i is the defined as the position of the inertance piston, and the force acting on the piston is the pressure across the piston, p_r, multiplied by the area of the piston, A_i. The variable t refers to time. Similarly, for the piston in the resonator:

$$M_R \frac{d^2 x_R}{dt^2} = (p_t - p_0)\, A_R = \delta p_t A_R \tag{A.8}$$

where x_R is the position of the resonator piston along the axis of the resonator, and δp_t is the pressure across the resonator piston. Given that the volume of section (d) is the initial volume plus the displacement volume of the inertance piston:

$$V_d = V_{d0} + A_i x_i \tag{A.9}$$

Rearranging Eq. (A.9) in terms of x_i:

$$x_i = \frac{V_d}{A_i} - \frac{V_{d0}}{A_i} \tag{A.10}$$

Taking the 2nd derivative of Eq. (A.10) in terms of t, knowing that V_{d0} and A_i are constants:

$$\frac{d^2 x_i}{dt^2} = \frac{1}{A_i} \frac{d^2 V_d}{dt^2} \tag{A.11}$$

Inserting Eq. (A.11) into Eq. (A.7) yields:

$$M_i \frac{1}{A_i} \frac{d^2 V_d}{dt^2} = p_r A_i \tag{A.12}$$

and therefore:

$$\frac{d^2 V_d}{dt^2} = p_r \frac{A_i^2}{M_i} \tag{A.13}$$

Using the same process for V_r with Eq. (A.8):

$$\frac{d^2 V_R}{dt^2} = \delta p_t \frac{A_R^2}{M_R} \tag{A.14}$$

Incorporating the following conventions:

$$a_R = \frac{A_R^2}{M_R} \tag{A.15}$$

and:

$$a_i = \frac{A_i^2}{M_i} \tag{A.16}$$

Then Eq. (A.13) and Eq. (A.14) become:

$$\frac{d^2V_d}{dt^2} = a_i p_r \tag{A.17}$$

and:

$$\frac{d^2V_R}{dt^2} = a_R \delta p_t \tag{A.18}$$

In determining the volume flow rates for $\overset{*}{V}_c$, $\overset{*}{V}_d$, $\overset{*}{V}_t$, and $\overset{*}{V}_b$, earh of the components of the decomposed model are identified as one of the three flow situations. The first is where volume flows into and out of a control volume. The second is a situation where volume flows into a volume with a moving piston, and the third is where volume flows from (or into) a volume connected by a valve with flow conductance C. These are depicted below in Fig. A.1:

From Fig. A.1, the element labeled (a) is the generalized model of the pulse tube, or the component (t) from Fig. 3.2. The element labeled (b) is the generalized model of the compliance, the feedback tube, and the resonator tube; components (c), (d), and (R) respectively from Fig. 3.2. The element labeled (c) is the generalized model of the buffer tube; component (b) from Fig. 3.2.

A.T.A.M. de Waeles paper describes the relationship for volume flow rates $\overset{*}{V}_1$ and $\overset{*}{V}_2$ of element (a) from Fig. A.1 and is given as [10]:

$$\overset{*}{V}_1 = \overset{*}{V}_2 + \frac{V}{\gamma p}\frac{dp}{dt} \tag{A.19}$$

In Eq. (A.19), V refers to the volume of the element; in this case a fixed

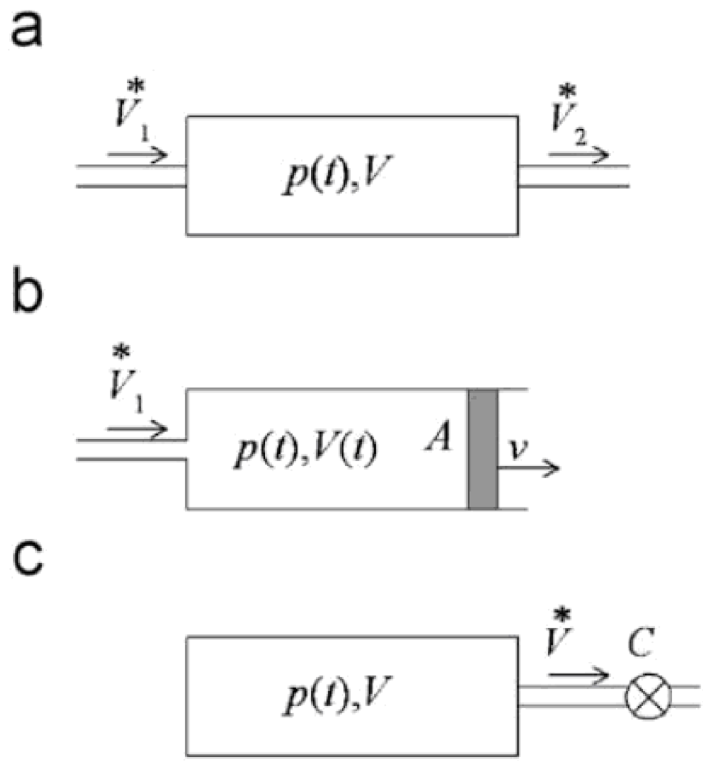

Figure A.1: Three generalized component models as analyzed by A.T.A.M. de Waele [10].

volume, p refers to the pressure of the element, and γ is the specific heat ratio of the working gas. This relationship works on a few assumptions. First, the process that takes place in element (a) from Fig. A.1 is that of an adiabatic ideal gas. Secondly, the oscillations about the initial pressure, p_0 are small relative to p_0. Also, each element is considered discrete and well mixed, meaning the pressure, density, and temperature in the element is considered uniform at all points. To prove this equation, consider the fixed size control volume V. The mass m of the air in the control volume is defined as:

$$m = \rho V \tag{A.20}$$

In Eq. (A.20), ρ is the density of the air in the control volume. Because the inlet and outlet flow rates are not necessarily equal, the system may gain or lose mass. The time differential of Eq. (A.20) is:

$$\frac{dm}{dt} = \frac{d\rho}{t}V + \frac{dV}{dt}\rho \tag{A.21}$$

But for element (a), the volume is invariable, therefore:

$$\frac{dV}{dt} = 0 \tag{A.22}$$

Therefore, Eq. (A.21) becomes:

$$\frac{dm}{dt} = \frac{d\rho}{dt}V \tag{A.23}$$

Which therefore implies:

$$\frac{d\rho}{dt} = \frac{1}{V}\frac{dm}{dt} \tag{A.24}$$

This first order approximation relationship between the pressure and the density is fairly accurate for small pressure oscillations about the initial pressure p_0. The relationship is given as [27]:

$$p = c^2\rho \tag{A.25}$$

In Eq. (A.25), c is the speed of sound defined for an ideal, adiabatic gas is defined as [27]:

$$c = \sqrt{\frac{\gamma p}{\rho}} \tag{A.26}$$

For the derivation, c is considered a constant independent of time because of the small magnitude of the pressure oscillations relative to the initial pressure. Taking the time derivative of Eq. (A.25):

$$\frac{dp}{dt} = c^2 \frac{d\rho}{dt} \tag{A.27}$$

Combining Eq. (A.24) and Eq. (A.27):

$$\frac{dp}{dt} = \frac{c^2}{V} \frac{m}{dt} \tag{A.28}$$

Now define the time derivative of the mass in the control volume as the difference between the mass flow rate entering the control volume subtracted by the mass flowing out of the control volume:

$$\frac{dm}{dt} = \frac{dm_1}{dt} - \frac{dm_2}{dt} \tag{A.29}$$

The relationship between mass flow rate and volume flow rate are defined as follows [15]:

$$\frac{dm}{dt} = \rho \overset{*}{V} \tag{A.30}$$

This gives:

$$\frac{dm}{dt} = \rho\left(\overset{*}{V}_1 - \overset{*}{V}_2\right) \tag{A.31}$$

Which combined with Eq. (A.28) and Eq. (A.26) to become Eq. (A.19), which verifies the volume flow governing equation for element (a) from Fig. A.1. As the process is assumed to be adiabatic, meaning no heat is transferred from the engine aside from the heat exchangers, it is logical that the derived expression in Eq. (A.19) does not depend on temperature. The expression for volume flow rates of element (b) from Fig. A.1 is reported as [10]:

$$\overset{*}{V}_1 = vA + \frac{V}{\gamma p}\frac{dp}{dt} \tag{A.32}$$

In Eq. (A.32), v is the velocity of the piston depicted in element (b) of Fig. A.1, while A is the cross sectional area of the volume. In this case, consider the control volume time dependant on the position of the piston. The volume is assumed to be adiabatic, and it is also assumed that the pressure oscillations about p_0 are small relative to p_0. Again, it is assumed that pressure, density, and temperature are uniform within the control volume. Because of these assumptions, Eq. (A.25) and Eq. (A.26) hold. Begin by assuming that the rate of change of the control volume is dependent on the motion of the piston:

$$\frac{dV}{dt} = vA \tag{A.33}$$

Combining Eq. (A.34) with Eq. (A.21):

$$\frac{dm}{dt} = \frac{d\rho}{dt}V + vA\rho \tag{A.34}$$

In Eq. (A.29), it is assumed that:

$$\frac{dm_2}{dt} = 0 \tag{A.35}$$

Therefore with Eq. (A.26), Eq. (A.27) and Eq. (A.30), Eq. (A.35) becomes Eq. (A.32) as reported by deWaele. The expression for volume flow rates of element (c) from Fig. A.1 is reported as [10]:

$$0 = C\left(p - p_0\right) + \frac{V}{\gamma p}\frac{dp}{dt} \tag{A.36}$$

In this case, the control volume is a constant. Therefore in this situation, Eq. (A.23) is valid. The volume is again assumed to be adiabatic, and it is also assumed that the pressure oscillations about p_0 are small relative to p_0. Again, it is assumed that pressure, density and temperature are uniform within the control volume. Because of these assumptions, Eq. (A.25) and Eq. (A.26) hold. It is assumed that the volume flow rate leaving the tank is dependant on the pressure across the valve multiplied by the flow conductance. Therefore:

$$\overset{*}{V} = C\left(p - p_0\right) \tag{A.37}$$

Because the figure only depicts mass leaving the tank, from Eq. (A.29 let:

$$\frac{dm_1}{dt} = 0 \tag{A.38}$$

and let:

$$\frac{dm_2}{dt} = -\rho \overset{*}{V} \tag{A.39}$$

By combining Eq. (A.37) and Eq. (A.39) with Eq. (A.29):

$$\frac{dm}{dt} = -\rho C \left(p - p_0\right) \tag{A.40}$$

Which combines with Eq. (A.24), Eq. (A.26) and Eq. (A.27) to give Eq. (A.36). By using the expressions derived in Eq. (A.19), Eq. (A.32), and Eq. (A.36), the volume flow rates for $\overset{*}{V}_c$, $\overset{*}{V}_d$, $\overset{*}{V}_t$, and $\overset{*}{V}_b$ can be determined. Beginning with $\overset{*}{V}_b$, it is assumed that the buffer volume is large enough that the pressure inside remains approximately p_0. Therefore, with flow conductance C_0, and the pressure across the valve values at δp_t:

$$\overset{*}{V}_b = C_0 \delta p_t \tag{A.41}$$

Introducing a new convention, because the pressure oscillations about p_0 are small compared the p_0, the values for ${}^{V}/_{\gamma p}$ in Eq. (A.19), Eq. (A.32), and Eq. (A.36) will be replaced by average values ${}^{V_0}/_{\gamma p}$. Therefore, for $i = R, c, d,$ and t, let:

$$w_i = \frac{\gamma p_0}{V_{i0}} \tag{A.42}$$

Therefore, for the pulse tube component labelled (t) in Fig. A.1, using Eq. (A.19) and Eq. (A.42):

$$\overset{*}{V}_h = \overset{*}{V}_t + \frac{1}{w_t}\frac{dp_t}{dt} \tag{A.43}$$

Therefore, for the feedback tube component labelled (d) in Fig. A.1, using Eq. (A.32) and Eq. (A.42):

$$\overset{*}{V}_d = \frac{1}{w_d}\frac{dp_d}{dt} + vA \tag{A.44}$$

Therefore Eq. (A.44) in conjunction with Eq. (A.34) gives:

$$\overset{*}{V}_d = \frac{1}{w_d}\frac{dp_d}{dt} + \frac{dV_d}{dt} \tag{A.45}$$

Taking into account Eq. (A.2):

$$\overset{*}{V}_d = \frac{1}{w_d}\frac{dp_t}{dt} + \frac{dV_d}{dt} \tag{A.46}$$

By similar process as for the component labelled (d), it can be seen that the equation describing the volume flow rate through resonator component, labelled (R) in Fig. A.1 can be derived as:

$$\overset{*}{V}_R = \frac{1}{w_R}\frac{dp_t}{dt} + \frac{dV_R}{dt} \tag{A.47}$$

and for the component labelled (c) in Fig. A.1, incorporating Eq. (A.32), Eq. (A.34) gives:

$$-\overset{*}{V}_c = \frac{1}{w_c}\frac{dp_c}{dt} + \frac{dV_c}{dt} \tag{A.48}$$

and since:

$$\frac{dV_c}{dt} = -\frac{dV_d}{dt} \tag{A.49}$$

Therefore:

$$\overset{*}{V}_c = -\frac{1}{w_c}\frac{dp_c}{dt} + \frac{dV_d}{dt} \tag{A.50}$$

It is assumed that the regenerator in the engine, with an input volumetric flow rate of $\overset{*}{V}_c$ and an outlet flow rate of $\overset{*}{V}_h$, is without volume and is therefore treated like a node point. By conservation of mass, it must be that:

$$\frac{dm_c}{dt} = \frac{dm_h}{dt} \tag{A.51}$$

Incorporating Eq. (A.30) into Eq. (A.51):

$$\overset{*}{V}_h \rho_h = \overset{*}{V}_c \rho_c \tag{A.52}$$

Assuming that even though the regenerator is without volume, $\overset{*}{V}_c$ enters the regenerator at temperature T_a. Because there is excellent thermal contact within the regenerator due to the small hydraulic radius of the regenerator medium, this is a safe assumption. Also assume that $\overset{*}{V}_h$ leaves the regenerator at the hot heat exchanger with a temperature T_t. It is given that one of the definitions of density is as follows [15]:

$$\rho = \frac{Mp}{RT} \tag{A.53}$$

In Eq. (A.53), M refers to the molar mass of air. R refers to the universal gas constant, p is the pressure, and T is the absolute temperature. Both M and R are the same for both $\overset{*}{V}_c$ and $\overset{*}{V}_h$. Because it is assumed that the regenerator is without volume, then the pressures must also be the same. Therefore, using Eq. (A.53) in Eq. (A.52), the relationship between $\overset{*}{V}_c$ and $\overset{*}{V}_h$ can be described as:

$$\overset{*}{V}_h = \tau_t \overset{*}{V}_c \tag{A.54}$$

where in Eq. (A.54), τ_t is the ratio between the hot (T_t) and cold (T_a) heat exchanger temperatures. De Waele [10] presents a linear approximation for in terms of the pressure drop across the regenerator (p_r):

$$\overset{*}{V}_c = -C_r p_r \tag{A.55}$$

In Eq. (A.55), C_r is the flow conductance of the regenerator defined:

$$C_r = \frac{1}{\eta_a Z_r} \tag{A.56}$$

In Eq. (A.56), η_a is the viscocity of air at room temperature, and Z_r is defined as:

$$Z_r = \frac{z_r L_r}{A_r} \tag{A.57}$$

where in Eq. (A.57), L_r is the length of the regenerator, A_r is the cross sectional area of the resonator, and z_r is the specific flow resistance. Also note that:

$$\frac{d\delta p_t}{dt} = \frac{dp_t}{dt} \tag{A.58}$$

Using Eq. (A.54), Eq. (A.55) and Eq. (A.58), Eq. (A.43) becomes:

$$-\tau_t C_r p_r = \overset{*}{V}_t + \frac{1}{w_t}\frac{d\delta p_t}{dt} \tag{A.59}$$

Which can be rearranged to be:

$$\overset{*}{V}_t = -\tau_t C_r p_r - \frac{1}{w_t}\frac{d\delta p_t}{dt} \tag{A.60}$$

Eq. (A.58) also alters Eq. (A.46) and Eq. (A.47) to be:

$$\begin{aligned} \overset{*}{V}_d &= \frac{1}{w_d}\frac{d\delta p_t}{dt} + \frac{dV_d}{dt} \\ \overset{*}{V}_R &= \frac{1}{w_R}\frac{d\delta p_t}{dt} + \frac{dV_R}{dt} \end{aligned} \tag{A.61}$$

The volumes in the model are connected by frictionless isobaric connections. Performing nodal conservation of mass analysis at the following point in the engine yields an expression relating $\overset{*}{V}_d$, $\overset{*}{V}_t$, $\overset{*}{V}_R$ and $\overset{*}{V}_b$.

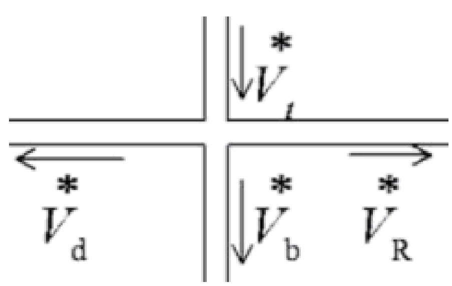

Figure A.2: Isobaric connection between components (t), (d), (b) and (R.) [10]

By applying conservation of mass at the juncture depicted in Fig. A.2, and treating the terms flowing towards the junction as positive and those flowing away as negative, the following expression is related:

$$\overset{*}{V}_t = \overset{*}{V}_d + \overset{*}{V}_b + \overset{*}{V}_R \tag{A.62}$$

Which, with Eq. (A.60), Eq. (A.61) and Eq. (A.41) yields:

$$\tau_t C_r p_r + \frac{1}{w_t}\frac{d\delta p_t}{dt} + \frac{1}{w_d}\frac{d\delta p_t}{dt} + \frac{dV_d}{dt} + \frac{1}{w_R}\frac{d\delta p_t}{dt} + \frac{dV_R}{dt} + C_0 \delta p_t = 0 \tag{A.63}$$

Combining like terms in Eq. (A.63) gives:

$$\tau_t C_r p_r + \left(\frac{1}{w_t} + \frac{1}{w_d} + \frac{1}{w_R}\right)\frac{d\delta p_t}{dt} + \frac{dV_d}{dt} + \frac{dV_R}{dt} + C_0 \delta p_t = 0 \tag{A.64}$$

Introducing the following notation:

$$w_e = \frac{\gamma p_0}{V_t + V_{d0} + V_{R0}} \tag{A.65}$$

Then, incorporating Eq. (A.65) into Eq. (A.64) with some rearranging yields:

$$-\frac{d\delta p_t}{dt} = \tau_t w_e C_r p_r + w_e \frac{dV_d}{dt} + w_e \frac{dV_R}{dt} + w_e C_0 \delta p_t \tag{A.66}$$

Meanwhile, combining Eq. (A.50) and Eq. (A.55) yields:

$$C_r p_r = \frac{1}{w_c}\frac{dp_c}{dt} - \frac{dV_d}{dt} \tag{A.67}$$

Replacing $\frac{dp_c}{dt}$ with $\frac{dp_t}{dt} - \frac{dp_r}{dt}$ in Eq. (A.67):

$$C_r p_r = \frac{1}{w_c}\left(\frac{dp_t}{dt} - \frac{dp_r}{dt}\right) - \frac{dV_d}{dt} \tag{A.68}$$

Combining Eq. (A.66) with Eq. (A.68):

$$w_c C_r p_r + \frac{dp_r}{dt} + w_c \frac{dV_d}{dt} = -\left(\tau_t w_e C_r p_r + w_e \frac{dV_d}{dt} + w_e \frac{dV_R}{dt} + w_e C_0 \delta p_t\right) \tag{A.69}$$

Rearranging and combining like terms gives:

$$-\frac{dp_r}{dt} = (w_e + w_c)\frac{dV_d}{dt} + (w_c C_r + \tau_t w_e C_r)\, p_r + w_e C_0 \delta p_t + w_e \frac{dV_R}{dt} \tag{A.70}$$

Meanwhile, taking the time derivative of Eq. (A.66) yields:

$$-\frac{d^2 \delta p_t}{dt^2} = \tau_t w_e C_r \frac{dp_r}{dt} + w_e \frac{d^2 V_d}{dt^2} + w_e \frac{d^2 V_R}{dt^2} + w_e C_0 \frac{d\delta p_t}{dt} \tag{A.71}$$

Substituting Eq. (A.17) and Eq. (A.18) into Eq. (A.71) and rearranging gives:

$$\frac{d^2 \delta p_t}{dt^2} + w_e C_0 \frac{d\delta p_t}{dt} + w_e a_R \delta p_t = -\tau_t w_e C_r \frac{dp_r}{dt} - w_e a_i p_r \tag{A.72}$$

Also, differentiating Eq. (A.70) with respect to time gives:

$$-\frac{d^2 p_r}{dt^2} = (w_e + w_c)\frac{d^2 V_d}{dt^2} + (w_c C_r + \tau_t w_e C_r)\frac{p_r}{dt} + w_e C_0 \frac{\delta p_t}{dt} + w_e \frac{d^2 V_R}{dt^2} \tag{A.73}$$

Substituting Eq. (A.17) and Eq. (A.18) into Eq. (A.73) and rearranging gives:

$$-w_e C_0 \frac{\delta p_t}{dt} - w_e a_R \delta p_t = \frac{d^2 p_r}{dt^2} + \left(w_c C_r + \tau_t w_e C_r\right) \frac{p_r}{dt} + \left(w_e + w_c\right) a_i p_r \tag{A.74}$$

Eq. (A.73) and Eq. (A.74) are two independent differential equations with two unknown variables p_r and δp_t. The following depicts the procedure for eliminating p_r to create one equation governing the parameter δp_t, that is, the pressure oscillation of the pulse tube and resonator about the initial pressure p_0. Defining the following conventions:

$$\begin{aligned} a &= \left(\tau_t w_e C_r + w_c C_r\right) \\ b &= \left(w_e + w_c\right) a_i \\ c &= -w_e C_0 \\ f &= -w_e a_R \end{aligned} \tag{A.75}$$

Additionally, define the following conventions:

$$\begin{aligned} k &= w_e C_0 \\ l &= w_e a_R \\ m &= -\tau_t w_e C_r \\ n &= -w_e a_i \end{aligned} \tag{A.76}$$

Substitution of Eq. (A.75) into Eq. (A.74) yields:

$$c \frac{\delta p_t}{dt} + f \delta p_t = \frac{d^2 p_r}{dt^2} + a \frac{p_r}{dt} + b p_r \tag{A.77}$$

and substitution of Eq. (A.76) into Eq. (A.72) yields:

$$\frac{d^2\delta p_t}{dt^2} + k\frac{d\delta p_t}{dt} + l\delta p_t = m\frac{dp_r}{dt} + np_r \tag{A.78}$$

Multiplying Eq. (A.78) with the following operator:

$$O_a = \frac{d^2}{dt^2} + a\frac{d}{dt} + b \tag{A.79}$$

Yields:

$$\left(\frac{d^2}{dt^2} + a\frac{d}{dt} + b\right)\left(\frac{d^2\delta p_t}{dt^2} + k\frac{d\delta p_t}{dt} + l\delta p_t\right) = \left(\frac{d^2}{dt^2} + a\frac{d}{dt} + b\right)\left(m\frac{dp_r}{dt} + np_r\right) \tag{A.80}$$

Due to the linearity of differential operators, the right hand side of Eq. (A.80) can be rearranged:

$$\left(\frac{d^2}{dt^2} + a\frac{d}{dt} + b\right)\left(\frac{d^2\delta p_t}{dt^2} + k\frac{d\delta p_t}{dt} + l\delta p_t\right) = \left(m\frac{d}{dt} + n\right)\left(\frac{d^2 p_r}{dt^2} + a\frac{dp_r}{dt} + bp_r\right) \tag{A.81}$$

By combining Eq. (A.77) with Eq. (A.81):

$$\left(\frac{d^2}{dt^2} + a\frac{d}{dt} + b\right)\left(\frac{d^2\delta p_t}{dt^2} + k\frac{d\delta p_t}{dt} + l\delta p_t\right) = \left(m\frac{d}{dt} + n\right)\left(c\frac{\delta p_t}{dt} + f\delta p_t\right) \tag{A.82}$$

Eq. (A.82) is now a single degree of freedom fourth order differential equation. By expanding the equation and condensing terms:

$$0 = \frac{d^4\delta p_t}{dt^4} + a_3\frac{d^3\delta p_t}{dt^3} + a_2\frac{d^2\delta p_t}{dt^2} + a_1\frac{d\delta p_t}{dt} + a_0\delta p_t \tag{A.83}$$

where:

$$
\begin{aligned}
a_3 &= k + a \\
a_2 &= l + ak - mc + b \\
a_1 &= al - mf - nc + bk \\
a_0 &= bl - nf
\end{aligned}
\tag{A.84}
$$

Replacing values for a, b, c, f, k, l, m, and n from Eq. (A.75) and Eq. (A.76) yields:

$$
\begin{aligned}
a_3 &= w_e C_0 + \tau_t w_e C_r + w_c C_r \\
a_2 &= w_e a_R + w_c C_r w_e C_0 + (w_e + w_c) a_i \\
a_1 &= w_c C_r w_e a_R + w_c a_i w_e C_0 \\
a_0 &= w_c a_i w_e a_R
\end{aligned}
\tag{A.85}
$$

Appendix B

Algebraic Analysis of Chapter 4

B.1 TWTAE Electric Analogue With Piezo End Cap

Beginning with Fig. 4.2, the following electric relationships can be described. For current flowing through the regenerator:

$$I_2 = \tau I_1 \tag{B.1}$$

In Eq. (B.1), τ is the ratio between the absolute hot and cold ends of the regenerator, T_H/T_C, as derived earlier by both Ceperly [4] and here in Chapter 3. In this case, τ represent current gain as defined by Eq. (A.54) and by the acoustic-electric analogies in Tab. 4.1. Continuing with other components of Fig. 4.2, define I_{tdR} as the sum of the currents through capacitor elements C_t, C_d, and C_R. To calculate the current across a capacitor for each of these components:

$$\begin{aligned} I_t &= V_t C_t s \\ I_d &= V_t C_d s \\ I_R &= V_t C_R s \end{aligned} \tag{B.2}$$

Therefore:

$$\begin{aligned} I_{tdR} &= I_t + I_d + I_R \\ &= V_t\left(C_t + C_d + C_R\right)s \end{aligned} \tag{B.3}$$

By using Kirchoff's voltage law:

$$I_2 = I_3 + I_4 + I_{tdR} \tag{B.4}$$

and also:

$$I_4 = I_c + I_1 \tag{B.5}$$

To calculate current across a resistance, as in the case of I_1:

$$I_1 = -(V_t - V_c)C_r \tag{B.6}$$

and to calculate the current across an inductor as in the case of I_4:

$$I_4 = (V_t - V_c)\frac{1}{L_i s} \tag{B.7}$$

and to calculate the current across the capacitor labelled C_c as in the case of Eq. (B.2):

$$I_c = V_c C_c s \tag{B.8}$$

Calculating the current I_3:

$$I_3 = V_t \frac{s}{M_D s^2 + Z\phi^2 s + \frac{K_p}{A_R^2}} \tag{B.9}$$

By using the convention $V_r = V_t - V_c$, and combining Eq. (B.1), Eq. (B.3), Eq. (B.7) and Eq. (B.9) into Eq. (B.4):

$$-\tau V_r C_r = V_t \frac{s}{M_D s^2 + Z\phi^2 s + \frac{K_p}{A_R^2}} + V_r \frac{1}{L_i s} + V_t (C_t + C_d + C_R) s \tag{B.10}$$

Using the convention $V_r = V_t - V_c$, and combining Eq. (B.6), Eq. (B.7) and Eq. (B.8) into Eq. (B.5) yields:

$$V_r \frac{1}{L_i s} = (V_t - V_r) C_c s - V_r C_r \tag{B.11}$$

Separating V_r and V_t terms in Eq. (B.11):

$$V_r = V_t \left(\frac{C_c L_i}{C_c L_i s^2 + C_r L_i s + 1} \right) \tag{B.12}$$

Separating V_r and V_t terms in Eq. (B.10) and applying Eq. (B.12):

$$\begin{aligned} -V_t \left(\frac{C_c L_i}{C_c L_i s^2 + C_r L_i s + 1} \right) & \left(\begin{array}{c} -\tau C_r L_i M_D s^3 + [M_D + \tau C_r L_i Z\phi^2] s^2 \\ + \left[Z\phi^2 + \tau C_r L_i \frac{K_p}{A_R^2} \right] s + \frac{K_p}{A_R^2} \end{array} \right) \\ = V_t & \left(\begin{array}{c} (C_t + C_d + C_R) M_D L_i s^2 + [C_t + C_d + C_R] Z\phi^2 L_i s \\ \left[L_i + (C_t + C_d + C_R) \frac{K_p}{A_R^2} L_i \right] \end{array} \right) \end{aligned} \tag{B.13}$$

Introducing the following convention:

$$\frac{1}{w_e} = C_t + C_d + C_R \tag{B.14}$$

and:

$$\frac{1}{w_c} = C_c \tag{B.15}$$

Simplifying Eq. (B.13) and incorporating Eq. (B.14) and Eq. (B.15):

$$0 = V_t \left[\begin{array}{l} \left(\frac{1}{w_c w_e} M_D L_i^2\right) s^4 \\ + \left(\frac{1}{w_c}\tau C_r M_D L_i^2 + \frac{1}{w_e} C_r M_D L_i^2 + \frac{1}{w_c w_e} L_i^2 Z \phi^2\right) s^3 \\ + \left(\begin{array}{l} \frac{1}{w_c} M_D L_i + \frac{1}{w_c}\tau C_r L_i^2 Z \phi^2 + \frac{1}{w_e} M_D L_i \\ + \frac{1}{w_e} C_r L_i^2 Z \phi^2 + \frac{1}{w_c} L_i^2 + \frac{1}{w_c w_e} \frac{K_p}{A_R^2} L_i^2 \end{array} \right) s^2 \\ + \left(\frac{1}{w_c} L_i Z \phi^2 + \frac{1}{w_c}\tau C_r L_i^2 \frac{K_p}{A_R^2} + \frac{1}{w_e} L_i Z \phi^2 + C_r L_i^2 + \frac{1}{w_e} C_r L_i^2 \frac{K_p}{A_R^2}\right) s \\ + C_c L_i \frac{K_p}{A_R^2} + L_i + \frac{1}{w_e} \frac{K_p}{A_R^2} L_i \end{array} \right] \tag{B.16}$$

Simplifying further and including Eq. (4.13):

$$
0 = V_t \left[\begin{array}{l}
\left(\frac{1}{w_c w_e} L_i^2 M_D R_L C_p\right) s^5 \\
+\left(\frac{1}{w_c}\tau C_r L_i^2 M_D R_L C_p + \frac{1}{w_c w_e} L_i^2 M_D + \frac{1}{w_e} C_r L_i^2 M_D R_L C_p\right) s^4 \\
+\left(\begin{array}{l}
\frac{1}{w_c}\tau L_i^2 C_r M_D + \frac{1}{w_c} L_i M_D R_L C_p + \frac{1}{w_e} C_r L_i^2 M_D \\
+\frac{1}{w_e} M_D L_i R_L C_p + \frac{1}{w_c w_e} L_i^2 R_L \phi^2 + \frac{1}{w_c} L_i^2 R_L C_p \\
+\frac{1}{w_c w_e} \frac{K_p}{A_R^2} L_i^2 R_L C_p
\end{array} \right) s^3 \\
+\left(\begin{array}{l}
\frac{1}{w_c} L_i M_D + \frac{1}{w_c}\tau C_r L_i^2 R_L \phi^2 + \frac{1}{w_c}\tau C_r L_i^2 \frac{K_p}{A_R^2} R_L C_p \\
+\frac{1}{w_e} M_D L_i + \frac{1}{w_e} C_r L_i^2 R_L \phi^2 + \frac{1}{w_c} L_i^2 \\
+\frac{1}{w_c w_e} \frac{K_p}{A_R^2} L_i^2 + C_r L_i^2 R_L C_p + \frac{1}{w_e} \frac{K_p}{A_R^2} C_r L_i^2 R_L C_p
\end{array} \right) s^2 \\
+\left(\begin{array}{l}
\frac{1}{w_c} L_i R_L \phi^2 + \frac{1}{w_c}\tau C_r L_i^2 \frac{K_p}{A_R^2} + \frac{1}{w_c} \frac{K_p}{A_R^2} L_i R_L C_p + \frac{1}{w_e} L_i R_L \phi^2 \\
+C_r L_i^2 + \frac{1}{w_e} \frac{K_p}{A_R^2} C_r L_i^2 + L_i R_L C_p + \frac{1}{w_e} \frac{K_p}{A_R^2} L_i R_L C_p
\end{array} \right) s \\
+\frac{1}{w_c} \frac{K_p}{A_R^2} L_i + \frac{1}{w_e} \frac{K_p}{A_R^2} L_i + L_i
\end{array} \right] \tag{B.17}
$$

Using Eq. (4.4) and Eq. (4.10), the following conventions can be made:

$$
\begin{aligned}
a_R &= \frac{A_R^2}{m_p} = \frac{1}{M_D} \\
a_i &= \frac{A_i^2}{M_i} = \frac{1}{L_i}
\end{aligned} \tag{B.18}
$$

Then, incorporating Eq. (4.12) and Eq. (B.18), Eq. (B.17) can be simplified to the following format:

$$
0 = V_t \left(s^5 + a_4 s^4 + a_3 s^3 + a_2 s^2 + a_1 s + a_0\right) \tag{B.19}
$$

where the coefficients a_0 through a_4 in Eq. (B.20) are:

$$
\begin{aligned}
a_4 &= \frac{1}{R_L C_p}(1 + \tau C_r w_e R_L C_p + w_c C_R R_L C_p) \\
a_3 &= \frac{1}{R_L C_p}\begin{pmatrix} \tau C_r w_e + a_i w_e R_L C_p + w_c C_r \\ + a_R R_L \frac{d^2 K_p^2}{A_R^2} + a_R w_e R_L C_p + a_R R_L C_p \frac{K_p^2}{A_R^2} \end{pmatrix} \\
a_2 &= \frac{1}{R_L C_p}\begin{pmatrix} a_i w_e + \tau a_R w_e C_r R_L \frac{d^2 K_p^2}{A_R^2} + \tau a_R w_e C_r \frac{K_p^2}{A_R^2} R_L C_p + w_c a_i \\ + a_R w_c C_r R_L \frac{d^2 K_p^2}{A_R^2} + a_R w_e + a_R \frac{K_p^2}{A_R^2} \\ + a_R w_c C_r \frac{K_p^2}{A_R^2} R_L C_p \end{pmatrix} \\
a_1 &= \frac{1}{R_L C_p}\begin{pmatrix} a_R a_i w_e R_L \frac{d^2 K_p^2}{A_R^2} + \tau a_R w_e C_r \frac{K_p^2}{A_R^2} + a_R a_i w_e \frac{K_p^2}{A_R^2} R_L C_p \\ + a_R a_i w_c R_L \frac{d^2 K_p^2}{A_R^2} + a_R w_e w_c C_r + a_R w_c C_r \frac{K_p^2}{A_R^2} \\ + a_R a_i w_e w_c R_L C_p + a_R a_i w_c \frac{K_p^2}{A_R^2} R_L C_p \end{pmatrix} \\
a_0 &= \frac{1}{R_L C_p}\left(a_R a_i w_e \frac{K_p^2}{A_R^2} + a_R a_i w_c w_e + a_R a_i w_c \frac{K_p^2}{A_R^2} \right) \qquad \text{(B.20)}
\end{aligned}
$$

Finally, including Eq. (4.11) the following can be stated:

$$
\omega_n^2 = \frac{K_p}{A_R^2 M_D} = \frac{a_R K_p}{A_R^2} \qquad \text{(B.21)}
$$

Using Eq. (B.21), Eq. (B.20) can be simplified to:

$$
\begin{aligned}
a_4 &= \frac{1}{R_L C_p}(1 + \tau C_r w_e R_L C_p + w_c C_R R_L C_p) \\
a_3 &= \frac{1}{R_L C_p}\begin{pmatrix} \tau C_r w_e + R_L C_p (a_i w_e + a_i w_c + a_R w_e) \\ + w_c C_r + \omega_n^2 R_L (C_p + d^2 K_p) \end{pmatrix} \\
a_2 &= \frac{1}{R_L C_p}\begin{pmatrix} \omega_n^2 + (a_i w_e + a_R w_e + w_c a_i) + \tau C_r w_e \omega_n^2 R_L (C_p + d^2 K_p) \\ + C_r w_c \omega_n^2 R_L (C_p + d^2 K_p) + a_R w_c w_e C_r R_L C_p \end{pmatrix}
\end{aligned}
$$

$$
\begin{aligned}
a_1 &= \frac{1}{R_L C_p}\left(\begin{array}{l} C_r w_c \omega_n^2 + a_i(w_e + w_c)\omega_n^2 R_L(C_p + d^2 K_p) + a_R w_e w_c C_r \\ \\ +a_R a_i w_e w_c R_L C_p + \tau w_e C_r \omega_n^2 \end{array}\right) \\
a_0 &= \frac{1}{R_L C_p}\left(a_i(w_e + w_c)\omega_n^2 + a_R a_i w_c w_e\right) \qquad \text{(B.22)}
\end{aligned}
$$

B.2 TWTAE Electric Analogue Without Piezo End Cap

As for the diagram described by Fig. 4.3, while $R_L = C_p = Z = Kp = 0$, L_R can be defined as:

$$
L_R = \frac{\rho_0 l_R}{A_R} \qquad \text{(B.23)}
$$

Beginning with Eq. (B.16) and replacing M_D with L_R the expression can be condensed to:

$$
0 = V_t \left(\begin{array}{l} \left(\frac{1}{w_c w_e} L_R L_i^2\right) s^4 \\ \\ + \left(\frac{1}{w_c}\tau L_R L_i^2 + \frac{1}{w_e} C_r M_D L_i^2\right) s^3 \\ \\ + \left(\frac{1}{w_c} L_R L_i + \frac{1}{w_e} L_R L_i + \frac{1}{w_c} L_i^2\right) s^2 \\ \\ + \left(C_r L_i^2\right) s \\ \\ L_i \end{array}\right) \qquad \text{(B.24)}
$$

and with the following conventions:

$$
\begin{aligned}
a_i &= \frac{1}{L_i} \\
a_R &= \frac{1}{L_R} \qquad \text{(B.25)}
\end{aligned}
$$

Then Eq. (B.24) can be reduced to:

$$
0 = V_t \begin{pmatrix} s^4 \\ + \left(\tau C_r w_e + w_c C_r\right) s^3 \\ + \left(a_i w_e + a_i w_c + a_R w_e\right) s^2 \\ + \left(a_R w_c w_e C_r\right) s \\ a_R a_i w_c w_e \end{pmatrix} \tag{B.26}
$$

Which is identical to the expression reported by deWaele [10].

Appendix C

Example MATLAB code

C.1 MATLAB code for Chapter 5

This chapter displays the MATLAB code used to determine the 2×2 matrix coupling $\overset{*}{V}$ and I with P_t and V in Chapter 5. The material and geometric properties used for this code are given in Tab. C.1.

Piezo-disk FE material and geometric properties

Property	**Symbol**	**Value**	**Unit**
Disk Geometries			
base layer outer radius	R_o	0.027432	m
piezo layer outer radius	R_i	0.015875	m
base layer thickness	t_b	0.00127	m
piezo layer thickness	t_p	0.0001905	m
Material Properties Base Layer			
base layer density	ρ_b	2700	kg/m^3
Young's modulus of base layer	E_b	70E9	N/m^2
Poisson's ratio of base layer	υ_b	0.334	
Material Properties Piezo Layer			
piezo elastic modulus	c^E	6.6E10	N/m^2
piezo compliance	$s^E = 1/c^E$	1.515E-11	m^2/N
electromagnetic coupling factor	K_{31}	0.35	
piezo-strain constant	d_{31}	-190E-12	m/V
permittivity	ε_{33}^T	1.945E-8	$Farad/m$
density of piezo	ρ_p	7600	kg/m^3
Poisson ratio of piezo	υ_p	0.5	
	$c_{11} = \frac{c^E}{1-\upsilon_p^2}$	8.8E10	N/m^2
	$c_{12} = \frac{\upsilon_p c^E}{1-\upsilon_p^2}$	4.4E10	N/m^2
	$e_1 = c^E d_{31}$	-12.54	$\frac{N}{mV}$
	$\eta_3 = \varepsilon_{33}^T(1-K_{31}^2)$	1.7067E-8	$Farad/m$

Table C.1: Geometric and material properties for combined aluminum-piezo disk FEM

```
%% Piezo and Disk Finite Element
%This M-File attempts to determine the values of the 2x2 matrix ...
    coupling
%a vector of w_1 and I with P_t and V.
close all
clear
clc
%% Material Properties, Geometries and the like
%Geometries
Ro = 0.054864/2;%m, 2.16 in
```

```
Ri = 0.03175/2; %m, 1.25 in
Ap = pi*Ri^2;
tb = 0.0003307; %m, 0.015 in
tp = 0.0003; %m 0.0075in
%%
% Material Properties: Beam
rhob = 2700; %kg/m^3
Eb = 70E9; % N/m^2
poissonb = 0.334;
%%
% Material properties: Piezo
cE = 6.6E10; % N/m^2
sE = 1/cE;
K31 = 0.35;
d31 = -190E-12; %m/V
eps = 1.945E-8; %Farad/m
rhop = 7600; %kg/m^3
poissonp = 0.5;

c11 = cE/(1-poissonp^2);
c12 = poissonp*cE/(1-poissonp^2);
e1 = cE*d31;
eta3 = eps*(1-K31^2);

%%
% Beginning matrix formulation for Np piezo elements and Nb ...
    additional base
% elements.
Np = 1;
Nb = 1;
NumNodes = Np + Nb +1;
L1 = ones(1,Np)*(Ri/Np);
L2 = ones(1,Nb)*(Ro-Ri)/Nb;
L_vec = [L1 L2];
ri_vec = zeros(1,length(L_vec)+1);
for n = 1:length(L_vec)
    ri_vec(n+1)=sum(L_vec(1:n));
end
syms s L
Fnum = 10000;
W = zeros(Fnum,1);
F11 = zeros(Fnum,1);
F12 = zeros(Fnum,1);
F21 = zeros(Fnum,1);
F22 = zeros(Fnum,1);
F11abs = zeros(Fnum,1);
F12abs = zeros(Fnum,1);
F21abs = zeros(Fnum,1);
F22abs = zeros(Fnum,1);
w1 = zeros(Fnum,1);
V1 = zeros(Fnum,1);

N = [1 0 0 0 0 0; 0 0 1 0 0 0; 0 0 0 1 0 0; 1 L 0 0 0 0; 0 0 1 L ...
    L^2 ...
```

```
    L^3 ; 0 0 0 1 2*L 3*L^2];
Ns = [1 s 0 0 0 0; 0 0 1 s s^2 s^3]*inv(N);
%%
% Base layer mass matrix:
M_global_base = zeros(3*NumNodes,3*NumNodes);
for n = 1:length(L_vec)
    L_iter = L_vec(n);
    r_i = ri_vec(n);
    Ns_L = subs(Ns,L,L_iter);
    Me = int(rhob*Ns_L'*Ns_L*2*pi*(r_i+s)*tb,s,1E-12,L_iter);
    M_global_base(3*n-2:3*n+3,3*n-2:3*n+3) = Me + ...
        M_global_base(3*n-2:3*n+3,3*n-2:3*n+3);
end
%M_global_base
%Base layer stiffness matrix
%B = zeros(4,6);
D = (Eb/(1-poissonb^2))*[1 poissonb 0 0; poissonb 1 0 0; 0 0 ...
    (tb^2)/12 ...
    poissonb/(tb^2); 0 0 poissonb*(tb^2)/12 (tb^2)/12];
K_global_base = zeros(3*NumNodes,3*NumNodes);
for n = 1:length(L_vec)
    L_iter = L_vec(n);
    r_i = ri_vec(n);
    Ns_L = subs(Ns,L,L_iter);
    B(1,:) = diff(Ns_L(1,:),s);
    B(2,:) = (1/(r_i+s))*Ns_L(1,:);
    B(3,:) = -diff(diff(Ns_L(2,:),s),s);
    B(4,:) = -(1/(r_i+s))*diff(Ns_L(2,:),s);
    K_int = B'*D*B*2*pi*(r_i+s)*tb;
    K_int = subs(K_int,conj(s),s);
    %check(1,n)=K_int(1,1);
    Ke = int(K_int,s,1E-12,L_iter);
    K_global_base(3*n-2:3*n+3,3*n-2:3*n+3) = Ke + ...
        K_global_base(3*n-2:3*n+3,3*n-2:3*n+3);
end
%pretty(simplify((check(1))))
% K_global_base

%
%Piezo layer mass matrix
M_global_piezo = zeros(3*NumNodes,3*NumNodes);
for n = 1:length(L1)
    L_iter = L_vec(n);
    r_i = ri_vec(n);
    Ns_L = subs(Ns,L,L_iter);
    Me = int(rhop*Ns_L'*Ns_L*2*pi*(r_i+s)*tp,s,1E-12,L_iter);
    M_global_piezo(3*n-2:3*n+3,3*n-2:3*n+3) = Me + ...
        M_global_piezo(3*n-2:3*n+3,3*n-2:3*n+3);
end

%%
%Piezo stiffness layer
N = [1 0 0 0 0 0 0; 0 0 1 0 0 0 0; 0 0 0 1 0 0 0; 1 L 0 0 0 0 0; ...
    0 0 1 L L^2 L^3 0; 0 0 0 1 2*L 3*L^2 0; 0 0 0 0 0 0 1];
```

```
N_inv = inv(N);
Ns = [1 s 0 0 0 0 0; 0 0 1 s s^2 s^3 0; 0 0 0 0 0 0 1]*N_inv;

K_global_piezo = zeros(3*NumNodes+1,3*NumNodes+1);
C = [c11 c12; c12 c11];
for n = 1:length(L1)
    L_iter = L_vec(n);
    r_i = ri_vec(n);
    Ns_L = subs(Ns,L,L_iter);
    B2(1,:) = diff(Ns_L(1,:),s)-(tb/2)*diff(diff(Ns_L(2,:),s),s);
    B2(2,:) = (1/(r_i+s))*Ns_L(1,:);
    A = B2 - inv(C)*[e1;e1]*[0 0 1/tp]*Ns_L;
    E = [ 0 0 1/tp]*Ns_L;
    K_int = A'*C*A*2*pi*(r_i+s)*tp- E'*eta3*E*2*pi*(r_i+s)*tp;
    %K_int = subs(K_int,conj(s),s);
    check(1,n)=K_int(1,1);
    Ke = int(K_int,s,1E-12,L_iter);
    K_global_piezo(3*n-2:3*n+3,3*n-2:3*n+3) = Ke(1:6,1:6) + ...
        K_global_piezo(3*n-2:3*n+3,3*n-2:3*n+3);
    K_global_piezo(3*n-2:3*n+3,end)= ...
        K_global_piezo(3*n-2:3*n+3,end)...
        +Ke(1:6,end);
    K_global_piezo(end,3*n-2:3*n+3)= ...
        K_global_piezo(end,3*n-2:3*n+3)...
        +Ke(end,1:6);
    K_global_piezo(end,end)=K_global_piezo(end,end)+ Ke(end,end);
end

%K_global_piezo

%%
% Equation of Motion
%-w^2M+K = Q
Msize = size(M_global_base+M_global_piezo);
M = zeros(Msize(1)+1,Msize(2)+1);
M(1:end-1,1:end-1)=M_global_base+M_global_piezo;
%M(end)=1;
K_base = zeros(Msize(1)+1,Msize(2)+1);
K_base(1:end-1,1:end-1)=K_global_base;
K = K_base+K_global_piezo;
syms V_in
Q = [zeros(length(M)-1,1);0.00];
for n=1:NumNodes
    if n==1
        Q(3*n-1,1) = pi*(ri_vec(n+1)^2)/4;
    elseif n==NumNodes
        Q(3*n-1,1) = pi*ri_vec(n)^2-pi*(ri_vec(n)/2+ri_vec(n-1))^2;
    else
        Q(3*n-1,1) = pi*(ri_vec(n)/2+ri_vec(n+1))^2 ...
        -pi*(ri_vec(n)/2+ri_vec(n-1))^2;
    end
end

%%
```

```
%Reformatting D
Eeqi = zeros(length(L1),7);
for n = 1:length(L1)
    L_iter = L_vec(n);
    r_i = ri_vec(n);
    Ns_L = subs(Ns,L,L_iter);
    B2(1,:) = diff(Ns_L(1,:),s)-(tb/2)*diff(diff(Ns_L(2,:),s),s);
    B2(2,:) = (1/(r_i+s))*Ns_L(1,:);
    E_eq = [e1 e1]*B2 + eta3*[0 0 1/tp]*Ns_L;
    Eeqi(n,:)=int(2*pi*(r_i+s)*E_eq,s,1E-12,L_iter);
end

E_total = zeros(1,length(M));
for n = 1:Np+1
    if n==1
        E_total(n) = Eeqi(n,1);
        E_total(n+1) = Eeqi(n,2);
        E_total(n+1) = Eeqi(n,3);
    elseif n==Np+1
        E_total(3*n-2) = Eeqi(Np,4);
        E_total(3*n-1) = Eeqi(Np,5);
        E_total(3*n) = Eeqi(Np,6);
    else
        E_total(3*n-2) = Eeqi(n-1,4)+Eeqi(n,1);
        E_total(3*n-1) = Eeqi(n-1,5)+Eeqi(n,2);
        E_total(3*n) = Eeqi(n-1,6)+ Eeqi(n,3);
    end
end

E_total(end) = sum(Eeqi(:,end));
%%
%Reformatting ZEp
Zeqi = zeros(length(L_vec),7);
for n = 1:length(L_vec)
    L_iter = L_vec(n);
    r_i = ri_vec(n);
    Ns_L = subs(Ns,L,L_iter);
    Z_eq = [0 1 0]*Ns_L;
    Zeqi(n,:)=int(2*pi*(r_i+s)*Z_eq,s,1E-12,L_iter);
end

Z_total = zeros(1,length(M));
for n = 1:Np+1
    if n==1
        Z_total(n) = Zeqi(n,1);
        Z_total(n+1) = Zeqi(n,2);
        Z_total(n+1) = Zeqi(n,3);
    elseif n==Np+1
        Z_total(3*n-2) = Zeqi(Np,4);
        Z_total(3*n-1) = Zeqi(Np,5);
        Z_total(3*n) = Zeqi(Np,6);
    else
        Z_total(3*n-2) = Zeqi(n-1,4)+Zeqi(n,1);
        Z_total(3*n-1) = Zeqi(n-1,5)+Zeqi(n,2);
```

```
            Z_total(3*n) = Zeqi(n-1,6)+ Zeqi(n,3);
        end
end

Z_total(end) = sum(Zeqi(:,end));


%%
% Row reduction and new matrix formulation
w2M_Ksize=size(M);
w2M_Ksize=w2M_Ksize(1);
Q([1 3 w2M_Ksize-3 w2M_Ksize-2 w2M_Ksize-1],:)=[];
Q_3N = Q(1:end-1);
E_total(:,[1 3 w2M_Ksize-3 w2M_Ksize-2 w2M_Ksize-1])=[];
Z_total(:,[1 3 w2M_Ksize-3 w2M_Ksize-2 w2M_Ksize-1])=[];
f_i = logspace(2,5,Fnum);

%% Frequency response
freq = zeros(size(f_i));
for f = 1:Fnum
    f
w = 2*pi*f_i(f);
freq(f) =  f_i(f);
w2M_K = -w^2*M+K;

w2M_K([1 3 w2M_Ksize-3 w2M_Ksize-2 w2M_Ksize-1],:)=[];
w2M_K(:,[1 3 w2M_Ksize-3 w2M_Ksize-2 w2M_Ksize-1])=[];
w2M_K_3N = w2M_K(1:end-1,1:end-1);
%%%%%
% disp = 13789.5146*inv(w2M_K)*Q;
% w1 = abs(disp(1));
% V1 = abs(disp(end));
%%%%%%


NewMatrix = [w2M_K; 1i*w*E_total];
%vpa(NewMatrix,2)
%
% Row rearrangement:
NewMatrixSize=size(NewMatrix);
NewMatrix=[NewMatrix(:,2:NewMatrixSize(2)-1), NewMatrix(:,1),...
    NewMatrix(:,end)];
NewMatrix=[NewMatrix(2:NewMatrixSize(1)-1,:); NewMatrix(1,:);...
    NewMatrix(end,:)];
%Q = [Q([2:end],1);Q(1)];
%vpa(NewMatrix,2)

NewMatrixSize=size(NewMatrix);
Kss = NewMatrix([1:NewMatrixSize(1)-2],[1:NewMatrixSize(2)-2]);
Ksp = NewMatrix([1:NewMatrixSize(1)-2],...
    [NewMatrixSize(2)-1:NewMatrixSize(2)]);
Kps = NewMatrix([NewMatrixSize(1)-1:NewMatrixSize(1)],...
    [1:NewMatrixSize(2)-2]);
Kpp = NewMatrix([NewMatrixSize(1)-1:NewMatrixSize(1)],...
```

```
    [NewMatrixSize(2)-1:NewMatrixSize(2)]);
NewMatrix2=[Kss Ksp; Kps Kpp];
Check = NewMatrix-NewMatrix2;
KssTKssinv = inv(Kss'*Kss);
R = Kpp - Kps*KssTKssinv*Kss'*Ksp;

Qs = Q([2:end],1);

Qs12 = -Kps*KssTKssinv*Kss'*Qs;
Qmatrix = [Qs12(1)+Q(1),0;0,1];
Fiw = inv(Qmatrix)*R;

F2x2 = [Fiw(1)-Fiw(2)*Fiw(3)/Fiw(4), Fiw(2)/Fiw(4);...
    -Fiw(3)/Fiw(4), 1/Fiw(4)];

W(f)=w;
F11(f) = F2x2(1,1);
F21(f) = F2x2(2,1);
F12(f) = F2x2(1,2);
F22(f) = F2x2(2,2);
F11abs(f) = abs(F2x2(1,1));
F21abs(f) = abs(F2x2(2,1));
F12abs(f) = abs(F2x2(1,2));
F22abs(f) = abs(F2x2(2,2));
w_1 = 13789.5146/F2x2(1,1);
w1(f)=abs(w_1);
V1(f) = abs(w_1*F2x2(2,1));

A_dd = w2M_K_3N;
A_dV =  w2M_K(1:end-1,end);
A_Vd =  w2M_K(end,1:end-1);
A_VV = w2M_K(end,end);

ZE = [1i*w*Z_total;1i*w*E_total];
ZE_3N = ZE(:,1:end-1);
ZE_end = ZE(:,end);
Zp = [ZE_3N*inv(A_dd)*Q_3N, -ZE_3N*inv(A_dd)*A_dV+ZE_end]


end

figure
loglog(freq,w1,'b','LineWidth',4)
title('w_1 and V vs. f, 2 element FEM')
xlabel('f (Hz)')
grid
hold on
loglog(freq,V1,'r','LineWidth',4)
legend('w_1 (m)','V_1(V)','Location','NorthEast')

%%
% Output of laser vibrometer:

frequencies = 100:50:2250;
```

```
DisplAmp = 1E6*[7.097E-6,...
    2.053E-6,...
    1.319E-6,...
    923.2E-9,...
    696.6E-9,...
    531.2E-9,...
    990.6E-9,...
    140.9E-9,...
    119.5E-9,...
    88.16E-9,...
    83.29E-9,...
    113.4E-9,...
    44.52E-9,...
    23.95E-9,...
    26.31E-9,...
    33.52E-9,...
    48.12E-9,...
    32.92E-9,...
    35.91E-9,...
    61.07E-9,...
    41.08E-9,...
    42.40E-9,...
    58.28E-9,...
    35.71E-9,...
    177.3E-9,...
    135.1E-9,...
    50.95E-9,...
    30.92E-9,...
    25.14E-9,...
    15.54E-9,...
    14.13E-9,...
    11.83E-9,...
    12.01E-9,...
    10.74E-9,...
    10.78E-9,...
    9.867E-9,...
    9.039E-9,...
    9.31E-9,...
    6.885E-9,...
    5.628E-9,...
    5.564E-9,...
    6.546E-9,...
    7.093E-9,...
    7.888E-9];
figure
plot(frequencies,DisplAmp,'g','LineWidth',4)
xlabel('f (Hz)')
ylabel('\mum')
title('Frequency response of center of disk as seen by laser ...
    Vibrometer')
grid on
xlim([600 1600])
```

C.2 MATLAB code for Chapter 3

This MATLAB code reproduces Figure 7 and Figure 8 from the paper deWaele published.

```
% Andrew Roshwalb
% This M-Flie will attempt to verify the transient plots ...
    presented by
% A.T.A.M. de Waele in their paper.  These are shown in figures ...
    7 and 8 of
% their papers.
clear
clc
close all

DR = 0.102; %m (Resonator Diameter)
Lac = 2; %m (Length ac resonator)
Dr = 0.0889; %m (Regenerator Diameter)
Lr = 0.073; %m (Length of regenerator)
zr = 3.6E9; %m^-2 (Specific impedance)
Lt = 0.24; %m (Length of pulse tube)
Dt = 0.078; %m (Diameter of pulse tube)
Ld0 = 0.209; %m (Average length of space d)
Dd = 0.085; %m (Diameter of space d)
Li = 0.256; %m (Length of inertance tube)
Di = 0.078; %m (Diameter of inertance tube)
Vc0 = 0.00283; %m^3 (Average volume of space c)
Ta = 300; %K (Ambient temperature)
po = 3e6; %Pa (Average pressure)
gamma = 1.67; % (Specific heat ratio)
na = 20e-6; %micro-s Pa (Viscocity at Ta)
rho0 = 4.81; %kg/m^3 (density)

%  The following values are then dervied from the previous ...
    parameters:
LR0=2*Lac/pi; % m (Initial length of resonator)
AR = pi*(DR/2)^2; %m^2 (Area of resonator)
MR = AR*LR0*rho0; % kg (mass of air in resonator)
Ai = pi*(Di/2)^2; %m^2 (Area of inertance tube)
Mi = Ai*Li*rho0; % kg (mass of air in resonator)
Ar = pi*(Dr/2)^2; % m^2 (area of regenerator)
Zr = zr*Lr/Ar; % impedance of regenerator
Cr = 1/(na*Zr);
At = pi*(Dt/2)^2; %m^2 (Area of pulse tube)
Vt = At*Lt; %m^3 (volume of pulse tube)
wc = gamma*po/Vc0; %convention
Ad = pi*(Dd/2)^2; %m^2 (Area of connectiing tube)
Vd0 = Ad*Ld0; %m^3 (Initial volume of connecting tube)

VR0 = AR*LR0; %m^3 (Initial volume of regenerator)
```

```
we = gamma*po/(Vt+Vd0+VR0); % convention
aR = AR^2/MR; % convention
ai =Ai^2/Mi; % convention
Co=0.1*Cr;

KaAr_Lr = 0.085; %W/K
tau_c = 2.6755;
Ttc=Ta*tau_c;
v=103;
tp=1/v;
Ch = 0.21; % J/K
Qt= 500; %W
% a3 = we*Co + wc*Cr + tau_t*we*Cr;
a2 = aR*we + ai*wc + ai*we + wc*we*Cr*Co; % coefficient a_2
a1 = wc*we*(Cr*aR+Co*ai); % coefficient a_1
ao = wc*we*aR*ai; % coeffficient a_0
b1 = we*Co+wc*Cr;
b2 = we*Cr;
wt= gamma*po/Vt;
wd = gamma*po/Vd0;
wR = gamma*po/VR0;
% First determine temperature and pressure as it approaches ...
    tau_critical.
% It is given that the initial temperature Tt is 600K and the inital
% pressure is 50e2 Pa
Tti = 600;
pti = 50e2;
time = 2;
gain = 10^-2;
sim('de_waele_trans')
Δ_pt = [tout, yout(:,1)];
Thot = [tout, yout(:,2)];
L = 20;
numbersegments = length(tout)/L;
numbersegments = floor(numbersegments);
for k=1:numbersegments
    sample = Δ_pt(1+(k-1)*L:k*L,:);
    sample = sortrows(sample,2);
    Δ_ptmax(k,:)=sample(end,:);
end

plot(Thot(:,1),Thot(:,2),'Linewidth',2)
hold on
plot(Δ_ptmax(:,1),Δ_ptmax(:,2),'r','Linewidth',2)
Tcritical = tau_c*ones(size(tout));
plot(tout,Ttc,'g','Linewidth',2)
axis([0 2 0 1500])
title('Recreation of Figure 7 from ATAM de Waele')
xlabel('t(s)')
legend('T_t (K)','p_1 (hPa)','T_c (K)')
grid
hold off

Ch = 21;
```

```
Qt = 2000;
gain = 10^-3;
Tti = 750;
pti = 50e2;
time = 6;
sim('de_waele_trans')
∆_pt = [tout, yout(:,1)];
Thot = [tout, yout(:,2)];
L = 20;
numbersegments = length(tout)/L;
numbersegments = floor(numbersegments);
for k=1:numbersegments
    sample = ∆_pt(1+(k-1)*L:k*L,:);
    sample = sortrows(sample,2);
    ∆_ptmax(k,:)=sample(end,:);
end
figure
plot(Thot(:,1),Thot(:,2),'Linewidth',2)
hold on
plot(∆_ptmax(:,1),∆_ptmax(:,2),'r','Linewidth',2)
Tcritical = tau_c*ones(size(tout));
plot(tout,Ttc,'g','Linewidth',2)
axis([0 6 0 1000])
title('Recreation of Figure 8 from ATAM de Waele')
xlabel('t(s)')
legend('T_t (K)','p_1 (kPa)','T_c (K)')
grid
```

This MATLAB code produces figures equivalent to Figure 7 and Figure 8 from the paper deWaele published but for the TWTAE described in Chapter 7.

```
% Andrew Roshwalb
% This M-Flie will attempt to reproduce the transient plots ...
    similar to those
% shown in figures 7 and 8 ofA.T.A.M. deWaele's publications, ...
    but specifically
% for this lab's TWTAE
clear
clc
close all

DR = 0.32/pi; %m (Resonator Diameter)
RR = DR/2; %m (Resonator Radius
RRr = 6.14e-2/(2*pi); %m (cone, smaller radius)
Lcone = 0.203; % m (cone length)
Lcone_eq = Lcone*(RR^2+RR*RRr+RRr^2)/(3*RR^2); %m (equivalent ...
    cone length)
LR_smallerduct = 0.3; %m
LR_smallerduct_eq = LR_smallerduct*RRr^2/(RR^2);
LR_largerduct = 0.2413; %m
```

```
LR_eq = LR_largerduct + LR_smallerduct_eq + Lcone_eq;...
    %m (Length ac resonator)
Dr = sqrt(4*3e-4/pi); %m (Regenerator Diameter)
Lr = 3e-2; %m (Length of regenerator)
zr = 3.6E9; %m^-2 (Specific impedance)
Lt = 6.14e-2; %m (Length of pulse tube)
Dt = Dr; %m (Diameter of pulse tube)
Ld0 = 0.314; %m (Average length of space d)
Lc0 = 0.314; %m (Average length of space c)
Dd = Dr; %m (Diameter of space d)
Dc = Dr; %m (Diameter of space c)
Li = Ld0/4; %m (Length of inertance tube)
Di = Dr/2; %m (Diameter of inertance tube)
Vc0 = Lc0*pi*(Dc/2)^2; %m^3 (Average volume of space c)
Ta = 300; %K (Ambient temperature)
po = 6e5; %Pa (Average pressure)
gamma = 1.67; % (Specific heat ratio)
na = 20e-6; %micro-s Pa (Viscocity at Ta)
rho0 = 4.81; %kg/m^3 (density)

%  The following values are then dervied from the previous ...
   parameters:
LR0=LR_eq; % m (Initial length of resonator)
Lac = LR0*pi/2;
AR = pi*(DR/2)^2; %m^2 (Area of resonator)
MR = AR*LR0*rho0; % kg (mass of air in resonator)
Ai = pi*(Di/2)^2; %m^2 (Area of inertance tube)
Mi = Ai*Li*rho0; % kg (mass of air in resonator)
Ar = pi*(Dr/2)^2; % m^2 (area of regenerator)
Zr = zr*Lr/Ar; % impedance of regenerator
Cr = 1/(na*Zr);
At = pi*(Dt/2)^2; %m^2 (Area of pulse tube)
Vt = At*Lt; %m^3 (volume of pulse tube)
wc = gamma*po/Vc0; %convention
Ad = pi*(Dd/2)^2; %m^2 (Area of connectiing tube)
Vd0 = Ad*Ld0; %m^3 (Initial volume of connecting tube)

VR0 = AR*LR0; %m^3 (Initial volume of regenerator)
we = gamma*po/(Vt+Vd0+VR0); % convention
aR = AR^2/MR; % convention
ai =Ai^2/Mi; % convention
Co=0.1*Cr;

KaAr_Lr = 0.085; %W/K

Ch = .021; % J/K
Qt= 301.5; %W
% a3 = we*Co + wc*Cr + tau_t*we*Cr;
a2 = aR*we + ai*wc + ai*we + wc*we*Cr*Co; % coefficient a_2
a1 = wc*we*(Cr*aR+Co*ai); % coefficient a_1
ao = wc*we*aR*ai; % coeffficient a_0
b1 = we*Co+wc*Cr;
b2 = we*Cr;
wt= gamma*po/Vt;
```

```
wd = gamma*po/Vd0;
wR = gamma*po/VR0;

%%
% Finding the
%rlocus(tf([0 1 0 0 0 ],[1 0 a2 a1 ao]));
% grid on
tau_c = (1.69e3-we*Co-wc*Cr)/(we*Cr);
Ttc=Ta*tau_c; %K
v=1.25e3/(2*pi);
tp=1/v;
% First determine temperature and pressure as it approaches ...
    tau_critical.
% It is given that the initial temperature Tt is 600K and the inital
% pressure is 50e2 Pa
Tti = 600;
pti = 50e2;
time = 0.8;
gain = 10^-2;
sim('Velocities')
∆_pt = [tout, yout(:,1)];
pc = [tout, yout(:,4)];
Thot = [tout, yout(:,2)];
L = 25;
numbersegments = length(tout)/L;
numbersegments = floor(numbersegments);
for k=1:numbersegments
    sample = ∆_pt(1+(k-1)*L:k*L,:);
    sample = sortrows(sample,2);
    ∆_ptmax(k,:)=sample(end,:);
    sample2 = pc(1+(k-1)*L:k*L,:);
    sample2 = sortrows(sample2,2);
    pcmax(k,:)=sample(end,:);
end
figure(2)
plot(Thot(:,1),Thot(:,2),'LineWidth',2)
hold on
plot(∆_ptmax(:,1),∆_ptmax(:,2),'r','LineWidth',2)
plot(pcmax(:,1),pcmax(:,2),'k','LineWidth',2)
Tcritical = tau_c*ones(size(tout));
plot(tout,Ttc,'g','LineWidth',2)
% axis([0 2 0 1500])
title(['Pressures, T_h_o_t , Ch = ',num2str(Ch),', Q = ...
    ',num2str(Qt)])
xlabel('Time - t(s)')
legend('T_t (K)','p_1 (hPa)','p_c(hPa)','T_c (K)')
grid on
hold off
figure(3)
grid on
VR_dot = [tout,yout(:,5)];
Vd_dot = [tout,yout(:,6)];
Vc_dot = [tout,yout(:,7)];
Vt_dot = [tout,yout(:,8)];
```

```
Vh_dot = [tout,yout(:,9)];
L = 50;
numbersegments = length(tout)/L;
numbersegments = floor(numbersegments);
for k=1:numbersegments
    sample = VR_dot(1+(k-1)*L:k*L,:);
    sample = sortrows(sample,2);
    VR_dotmax(k,:)=sample(end,:);
    sample2 = Vd_dot(1+(k-1)*L:k*L,:);
    sample2 = sortrows(sample2,2);
    Vd_dotmax(k,:)=sample2(end,:);
    sample3 = Vc_dot(1+(k-1)*L:k*L,:);
    sample3 = sortrows(sample3,2);
    Vc_dotmax(k,:)=sample3(end,:);
    sample4 = Vt_dot(1+(k-1)*L:k*L,:);
    sample4 = sortrows(sample4,2);
    Vt_dotmax(k,:)=sample4(end,:);
    sample5 = Vh_dot(1+(k-1)*L:k*L,:);
    sample5 = sortrows(sample5,2);
    Vh_dotmax(k,:)=sample5(end,:);
end
plot(VR_dotmax(:,1),VR_dotmax(:,2),'c',...
    Vd_dotmax(:,1),Vd_dotmax(:,2),'b',...
    Vc_dotmax(:,1),Vc_dotmax(:,2),'r',...
    Vt_dotmax(:,1),Vt_dotmax(:,2),'g',...
    Vh_dotmax(:,1),Vh_dotmax(:,2),'k','LineWidth',2)
grid on
legend('VR_d_o_t','Vd_d_o_t','Vc_d_o_t','Vt_d_o_t','Vh_d_o_t')
xlabel('Time - t(s)')
title(['Volume flow, Ch = ',num2str(Ch),', Q = ',num2str(Qt)])
ylabel('m^3/s')
```

C.3 Simulink block diagram used for transient response figure

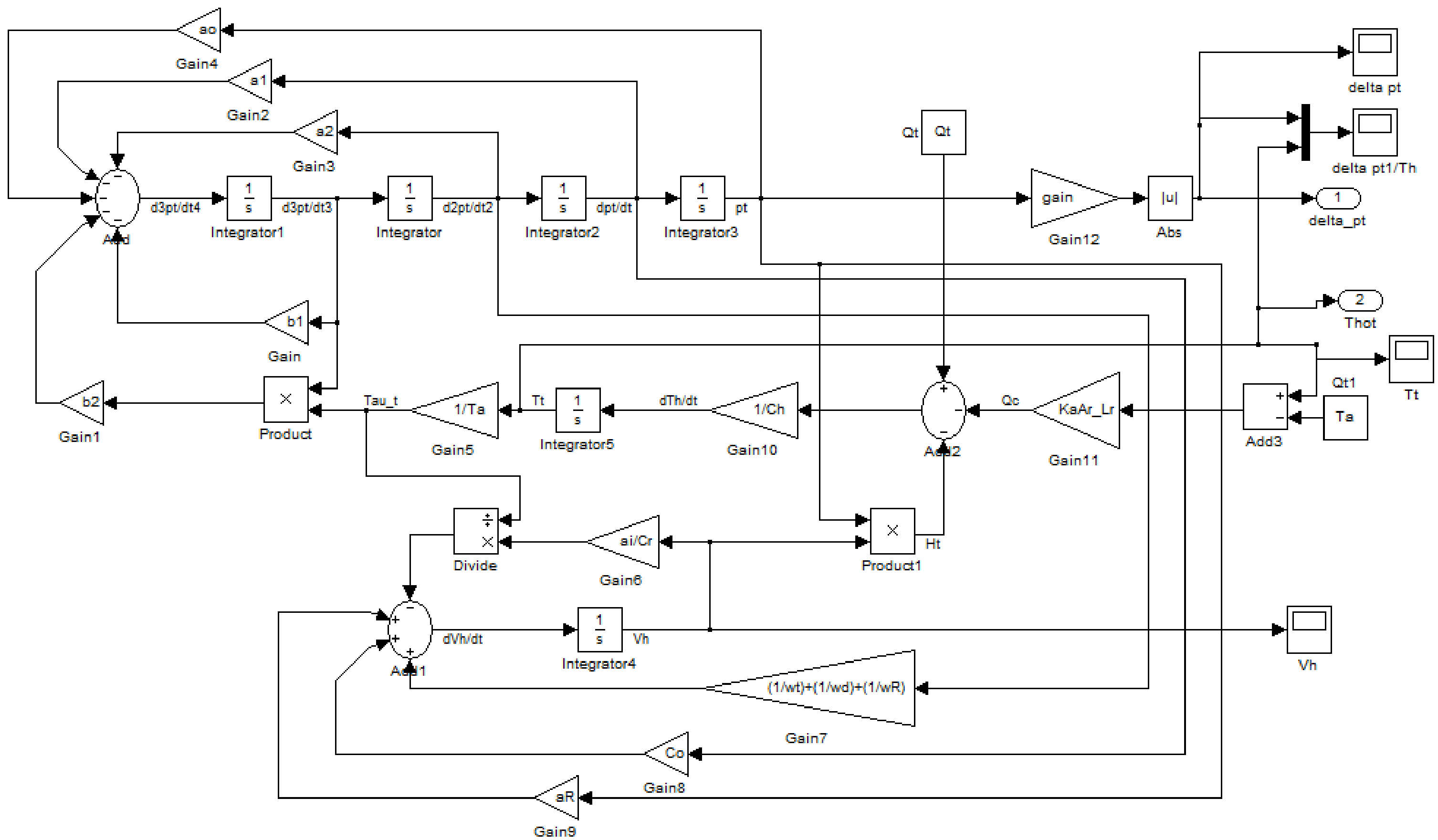

Figure C.1: Block diagram used for transient response figures

Appendix D

ANSYS Code

This chapter displays the ANSYS code used to determine the resonant frequencies of the piezo-aluminum disk system described in Chapter 5. The code is as follows:

```
!/CWD,'C:\Akl\UMD_Summer_2011\experiments_Impedance_metamaterials_cell
\ansys models\cell_only_impulse'

/FILNAME,Andrew_Model_Modal_Analysis,0
/title, Andrew Diaphragm Model
/nopr
/com,
/CONFIG,NRES,25000
/CONFIG,NBUF,4
/PREP7
/UNITS, MKS

!*** Data (Dimensions and Applied Volts)
!***************************************
inch=25.4e-3
Lp= 1.25/2*inch
Hp= 0.0075*inch
Ld= 2.16/2*inch
Hd= 0.015*inch

vtop = 100   !Voltage applied to the top of the PZT layer
vbot = 0 !Voltage applied to the bottom of the PZT layer
seltol,5e-7 !Selection tolerance

!*** Element Type and Material Properties
!****************************************
et,1,PLANE223,1001,,1 ! AxiSymmetric piezoelectric
element, plane stress

et,2,PLANE183    ! AxiSymmetric diaphragm element
KEYOPT,2,1,0
KEYOPT,2,3,1
KEYOPT,2,6,0
```

```
KEYOPT,2,10,0

MP,EX,2,70e9 ! Diaphragm material
MP,PRXY,2,0.31
MP,DENS,2,2700
!MP,DAMP,2,0.000135

/com  -- Material matrices for PZT4
(polar axis along Y-axis): ANSYS input
/com
/com   [c11 c13 c12  0  0  0 ]        [ 0 e31  0 ]
/com   [c13 c33 c13  0  0  0 ]        [ 0 e33  0 ]
/com   [c12 c13 c11  0  0  0 ]        [ 0 e31  0 ]
/com   [ 0   0   0  c44 0  0 ]        [e15 0   0 ]
/com   [ 0   0   0   0 c44 0 ]        [ 0  0  e15]
/com   [ 0   0   0   0  0 c66]        [ 0  0   0 ]

c11=13.2e10
c12=7.1e10
c13=7.3e10
c33=11.5e10
c44=2.6e10
c66=3e10

tb,anel,1 !Define structural table
tbdata,1,c11,c13,c12 !Input elastic stiffness matrix [c]
tbdata,7,c33,c13
tbdata,12,c11
tbdata,16,c44
tbdata,19,c44
tbdata,21,c66

e13=-4.1
e33=14.1
e15=10.5

tb,piez,1 !Define Piez. table
tbdata,2,e13 !Input Piezoelectric stress matrix [e]
tbdata,5,e33
tbdata,8,e13
tbdata,10,e15
tbdata,15,e15

MP,perx,1,804.6 !Permittivity (x direction)
MP,pery,1,659.7 !Permittivity (y direction)
MP,perz,1,804.6 !Permittivity (z direction)
MP,dens,1,7500 !Density
```

```
!*** Local Coordinate System
local,11          ! Coord. system for lower layer: polar axis +Y

!*** MODELING
!************
!Modeling Lower piezoelectric and diaphragm elements
!**************************************************
csys,11              ! Activate coord. system 11
rect,0,Lp,0,Hp       ! Create area for upper layer (xL, xR, yL, yU)
rect,0,Ld,-Hd,0
aglue,1,2      ! Glue layers
numcmp,all

! Area # 1  ---> Piezoelectric layer
! Area # 2  ---> Aluminum Diaphragm

!*** MESHING
!***********
! AATT, MAT, REAL, TYPE, ESYS, SECN
esize,1*Hp     ! Specify the element size for the piezo elements

! Meshing Lower Piezos
!*********************
AATT, 1,,1,11,
amesh, 1 ! Mesh Area # 1
allsel,all

! Meshing Diaphragms
!*******************
AATT, 2,,2,11,
amesh, 2 ! Mesh Area # 2
allsel,all

!*** Boundary Conditions

!*** Diaphragm and Cavity Walls
!******************************
nsel,r,loc,x,Ld
D,all,ux,0,,,,uy

!*** Piezoelectric Layer
!**********************
asel,s,,,1
nsla,,1
nsel,r,loc,y,0
!D,all,volt,vbot
```

```
cp,1,volt,all

asel,s,,,1
nsla,,1
nsel,r,loc,y,Hp
cp,2,volt,all
!D,all,volt,vbot
allsel,all

fini

/SOLU
ANTYPE,2 !Modal Analysis
MODOPT,LANB,4
EQSLV,SPAR
MXPAND,4, , ,0
MODOPT,LANB,10,0,1e6, ,OFF

solve

/POST1
SET,LIST,2
```

In addition to the first mode plot shown in Fig. 5.6, the next 3 modes of vibration were found to be as 5,318 Hz, and 12,701 Hz. These can be seen in Fig. D.1, Fig. D.2.

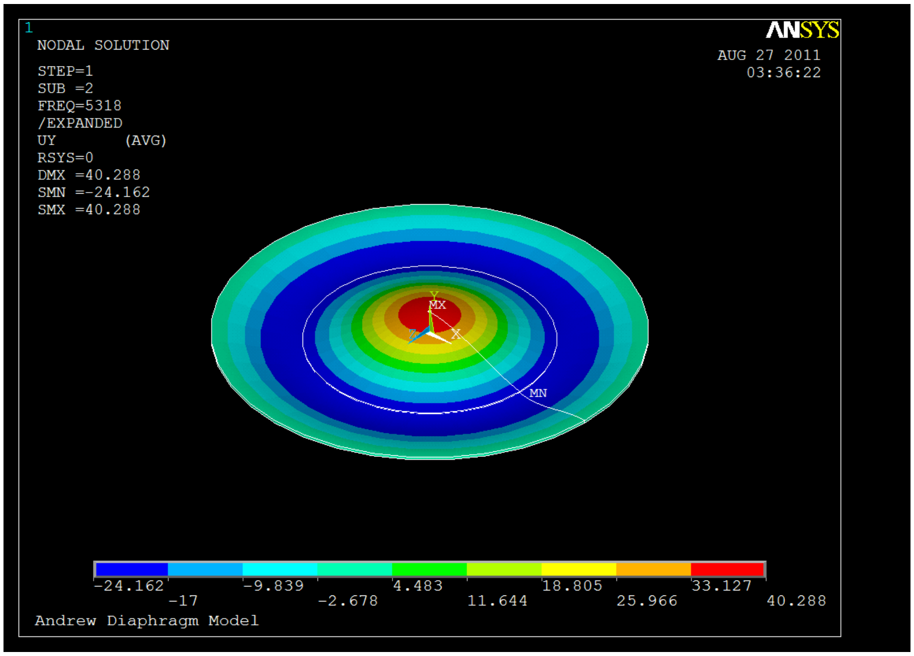

Figure D.1: Calculated frequency of 2^{nd} mode of combined piezo-aluminum disk system at 5,318 Hz

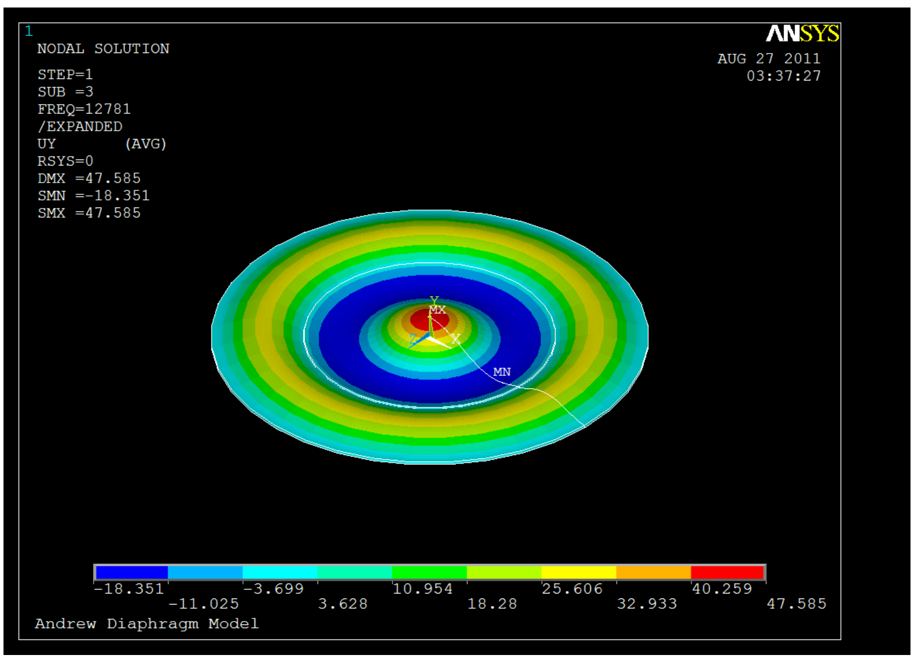

Figure D.2: Calculated frequency of 3^{rd} mode of combined piezo-aluminum disk system at 12,701 Hz

Bibliography

[1] G. W. Swift. *Thermoacoustics: A Unifying Perspective for some Engines and Refrigerators*. Acoustical Society of America Publications, Sewickley PA, 2002.

[2] Hartley, R., 1951 "Electrical Power Source," *U.S. Patent No.* 2,549,464.

[3] Marrison, W., 1958, "Heat-Controlled coustic Wave System," *U.S. Patent No.* 2,836,033.

[4] Ceperly, Peter H. "A Pistonless Stirling Engine- the Traveling wave heat engine." *The Journal of the Acoustical Society of America.* **66** (1979) 1508-1513.

[5] P.H. Ceperly. Resonant traveling wave heat engine, 1982 *U.S. Patent No.* 4,355,517.

[6] Walker, G., 1960, *Stirling Engines*, Clarendon, Oxford.

[7] Yazaki, T. et. al. "Traveling Wave Thermoacoustic Sngine in a Looped Tube." *Physical Review Letter.* **81** (1998) 3128-3131.

[8] Backhaus, S., and Swift, G.W., "A Thermoacoustic Stirling Engine." *Nature.* **399** (1999) 335-338.

[9] Backhaus, S., and Swift, G.W., "A Thermoacoustic Stirling Engine: Detailed Study." *The Journal of the Acoustical Society of America.* **107** (2000) 3148-3166.

[10] A.T.A.M. de Waele. "Basic treatment of onset conditions and transient effects in Thermoacoustic Stirling engines." *Journal of Sound and Vibration.* **325** (2009) 974-988.

[11] K.C. Rocky, H. R. Evans, D.W. Griffiths, and D.A. Nethercot, "The Finite Element Method: A Basic Introduction for Engineers", William Collins Sons & Co. Ltd, Great Britain 1985.

[12] F. Ashida and T. R. Tauchert, "Transient response of a piezothermoelastic circular disk under axisymmetric heating." *Acta Mechanica.* **128** (1998) 1-14.

[13] Ward, W.C. and Swift, G.W. "Design Environment for Low Amplitude Thermoacoustic Engines (DeltaE)." *The Journal of the Acoustical Society of America.* **95** (1994) 3671-3672.

[14] Backhaus, S., Tward, E., and Petarch, M., "Traveling Wave Thermoacoustic Electric Generator." *Applied Physics Letters.* **85** (2004) 1085-1087.

[15] Cengel, Yunus A. and Boles, Michael A. *Thermodynamics.* 4th ed. McGraw Hill: New York, 2002.

[16] Yuki Ueda, Testsushi Biwa, and Uichiro Mizutani, "Acoustic field in a thermoacoustic Stirling engine having a looped tube." *Applied Physics Letters.* **81** (2002) 5252-5254.

[17] T. Biwa, Y. Ueda, T. Yazaki, and U. Mizutani "Work flow measurements in a thermoacoustic engine." *Cryogenics.* **41** (2001) 305-310.

[18] Daming Sun, Limin Qiu, Wu hang, Weilin Yan, Guobang Chen, "Investigation on Traveling Wave Thermoacoustic Heat Engine with High Pressure Amplitude." *Energy Conversion and Management.* **46** (2005) 281-291.

[19] Swift, G.W. "Thermoacoustics: a Unifying Perspective for Some Engines and Refrigerators." Condensed Matter and Thermal Physics Group, Los Alamos National Laboratory, May 2001.

[20] Ceperly, Peter H. "Gain and Efficiency of a Short Traveling Wave Heat Engine." *The Journal of the Acoustical Society of America.* **77** (1985) 1239-1244.

[21] Swift, G.W. "Thermoacoustic Engines." *The Journal of the Acoustical Society of America.* **84** (1988) 1145-1180.

[22] Fusco, A.M., , W.C. and Swift, G.W. "Two sensor power measurements in lossy ducts." *The Journal of the Acoustical Society of America.* **91** (1992) 2229-2235.

[23] M.A. Lewis, T. Kuriyama, F. Kuriyama, and R. Radenbaugh, "Measurement of hear conduction through stacked screens," *Adv. Cryog. Eng.* **43** (1998) 1611-1618.

[24] Yuki Ueda, T. Biwa, U. Mizutani et al.,"Experimental Studies of a Thermoacoustic Stirling Prime Mover and its Application to a Cooler." *The Journal of the Acoustical Society of America.* **115** (2004) 1134-1141.

[25] Swift, G.W. "Thermoacoustic Energy Conversion."Chapter 7 of the *Springer Handbook of Acoustics*, edited by Thomas Rossing, 2007.

[26] Yu, G.Y. et al. "Study of Nonlinear Processes of a large experimental Thermoacoustic Stirling Heat Engine by Using Computational Fluid Dynamics." *Journal of Applied Physics.* **102** (2007) 074901.

[27] Blauert, J. Xiang, N. *Acoustics for Engineers.* Berlin: Springer-Verlag. 2008.

[28] P.H. Ceperly. Traveling wave heat engine, 1978 *U.S. Patent No.* 4,114,380.